Extraction of 3D Machined Surface Features and Applications

by

Yi Liao

A dissertation submitted in partial fulfillment
of the requirements for the degree of
Doctor of Philosophy
(Mechanical Engineering)
in The University of Michigan
2010

Doctoral Committee:

Professor Jun Ni, Chair

Professor Shixin Jack Hu

Associate Professor Ji Zhu

Research Scientist David A. Stephenson

© Yi Liao 2010
All Rights Reserved

To my dear husband Yang Lin,
my parents and parents-in-law.

ACKNOWLEDGMENTS

There are many people to whom I am deeply indebted for their help in the process that ends with this PhD dissertation. I take this opportunity to acknowledge their encouragement and support.

First of all, I wish to thank my PhD advisor Professor Jun Ni for offering me the opportunity to do my PhD in the S. M. Wu Manufacturing Research Center. Thanks to him, I have the opportunity to work on the NIST ATP project, which gave me great experiences of working with industry people. Special thanks also for his wise supervision, guidance, and encouragement. Without his continuous support, this dissertation would have not been accomplished.

I am deeply grateful to Mr. C.W. (Ron) Swonger, the Vice President of advanced technology of Coherix, Inc., who is my industry supervisor. He has contributed to the dissertation significantly. He has always had time to discuss the details of my projects, researches and papers, and give invaluable pieces of advice. Without him, I would not have completed this work.

I would like to thank Dr. David A. Stephenson, who is a research scientist in S. M. Wu Manufacturing Research Center. He was always willing to help me solve problems occurred in the projects, researches, and look into the details of my papers.

My gratitude also goes to Mr. Dwight Carlson, the CEO of Coherix, Inc., who believed in my research and offered me a great opportunity of doing internship at Coherix.

I want to thank Professors Shixin Jack Hu and Professor Zhu Ji, who gave me a lot of advice and practical instruction in the path of my PhD study.

Much appreciation to my dear friends, Shiming Duan, Xiaoning Jin, Hao Yu, Sibo Hu, Adam John Brzezinski, Xin Weng, Peiyun Yi, Chaoye Pan, Jingjing Li, Liang Zhou, Zhao Qin, Cindy Kuo and Bruce Tai. Most of these friends have put up with me for several years in the same office. Also, there are all the other friends I've made, the list is too long to mention but their friendships are thankful.

Finally, I dedicate this work to my parents and parents-in-law for the encouragement and support that they have never ceased to give me. Also, the last and the most precious, I would like to thank my husband, Yang Lin, who has always been standing by me in good and bad times for ten years. His support and understanding during these years is where I have drawn my strength to complete this doctoral study.

TABLE OF CONTENTS

LIST OF FIGURES

LIST OF TABLES

ABSTRACT

Continuous improvement of product quality is crucial to the success of competitive automotive manufacturing industry. Machined surfaces for sealing and similar applications in automotive powertrain manufacturing require increasingly stringent tolerances and higher repeatability. There is a need for engineers to go beyond specifying sizes, shapes and peaks, and move toward specifications of various surface functional attributes.

Most previous work on surface functional characterization has focused on surface tribological properties (roughness domain) for rotational and moving components, and they have made significant contributions. However, because of the limitation of the metrology technologies, most of these works were focused on only a small area of a large engineering surface. Therefore, characterizing large engineering surface comprehensively and rapidly presents significant challenges. Recently, a laser holographic interferometer has been developed by Coherix *Inc.* to rapidly measure a large workpiece surface (300mm×300mm) and generate a 3D surface height map in 40 seconds. This technology provides an unprecedented platform for developing extraction and characterization methods of 3D surface features larger than roughness scale and applying these features to predict some other surface functions and detect errors in the machining process.

In this research, an improved Gaussian filter is first designed to accurately extract 3D surface waviness from a large surface height map measured by the interferometer. The improved Gaussian filter enhances the performance of the standard Gaussian filter when applied to a surface which has large form distortion and many sharp peaks/valleys/noise. Following this, a 3D surface waviness feature of the machined workpiece is defined and applied to assess tool flank wear conditions. Experimental tests for different cutter types, workpiece materials and cutting conditions are implemented of using the waviness parameter to detect severe tool wear. The results verify that the proposed 3D surface waviness feature is a very good indicator for severe tool wear assessment.

Secondly, a two-channel filter bank diagram is developed that applies a 2D wavelet to decompose a 3D surface into multiple-scale subsurfaces. 3D surface features extracted from multiple-scale subsurfaces are then used to predict surface functional performances and detect machining errors. In the proposed surface decomposition process, two important issues: the elimination of border distortion and the transformation between the wavelet scale and its physical dimension are addressed. Applications of 2D wavelet decomposition to 3D surfaces are demonstrated using several automotive case studies, including abrupt tool breakage detection, chatter detection, cylinder head mating/sealing surface leak path detection, and transmission clutch piston surface non-clean up detection. These case studies demonstrate that the 3D surface features extracted from multiple-scale subsurfaces provide valuable information for surface functional performance prediction and machining error detection.

Finally, a novel and automated surface defect detection and classification system for flat machined surfaces is designed. The purpose of this work is to extract microscopic surface anomalies and assign each anomaly to a surface defect type commonly found on the automotive machined surfaces. A “breadboard” version surface defect inspection system using multiple directional illuminations is constructed. Related image processing algorithms are developed to detect and identify 5 types of 2D or 3D surface defects (pore, 2D blemish, residue dirt, scratch, and gouge). Several machined surface samples are tested and the results show that the microscopic surface defects which have a minimum dimension larger than 300 micron can be accurately detected and classified.

In summary, this research is dedicated to extract multiple-scale 3D surface texture features and apply these features to characterize some workpiece functional performances, discover issues in the machining process; and detect and classify certain classes of microscopic surface defects that are problematic to the manufacturing process.

CHAPTER 1

INTRODUCTION

1.1 Motivation

Metrology is the foundation of manufacturing. As illustrated in Figure 1.1, the measurement of a workpiece can be utilized for two different applications: (1) the production engineers use it to diagnose and control the manufacturing process and (2) the design engineers use it to optimize the functions of the product, such as sealing, loading, lubrication and so on. The two blocks, ‘manufacturing’ and ‘function’, are interdependent.

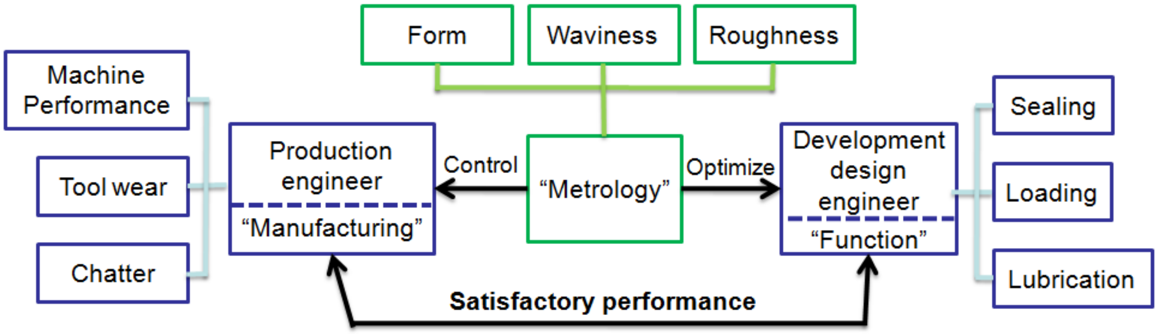

Figure 1.1 Importance of metrology.

In practice, workpiece is manufactured and measured sequentially to obtain the condition of a manufacturing process. If a workpiece functions satisfactorily, the same manufacturing conditions will be used to make the next workpiece. Thus, the measurement of the surface is being used as an effective go-gauge for the process and the function.

In the modern production process, the measurement of surface function becomes more and more important, since the surface of a machined component is the only part that interacts with its surrounding or mating parts. And it would be highly advantageous if the function of a surface is known before the part is tested or assembled.

Surface texture impacts many surface functions and applications. It is usually divided into three frequency domains, the short wavelength (high spatial frequency) components are considered as roughness; the long wavelength (low spatial frequency) components are referred to as form; the medium ones (middle spatial frequency) are treated as waviness [1][2]. Surface features extracted from different frequency bands are key indicators to predict various workpiece functional performances and detect errors in the manufacturing processes which produce the surface.

In early days, different instruments and measurement techniques were used to capture different wavelength bands. Stylus based instruments were used to measure roughness, other special instruments were used to obtain form information. Today, many instruments, like a stylus based instrument, can capture roughness, waviness and form. As the wavelength bandwidth of measurement instruments increases, mathematical methods for separating surface profile data into different wavelength bands are becoming popular research topics. Raja et al. [3] reviewed the recent filter techniques used in the separation of roughness, waviness and form. These filter techniques are: analog 2RC filter [1][4][5], Gaussian filter [2][6][7][8][9] and several newer research methods such as the spline filter [10][11], morphological filter [12][13] and wavelet filter [14][15][16] [17][18][19].

Conventionally, surface texture is characterized with 2D parameters based on the data measured by a profilometer or point-based measurement instrument. Researchers used 2D parameters to characterize surface functional performance [1][20][21][22]. However, sometimes the 2D parameters are inadequate or not capable to characterize the surface [23][24].

In recent years, with the invention of 3D profilometer, optical interferometer and other measurement techniques, 3D surface topography measurement has become realistic [25][26][27][28][29][30][31][32][33]. The area measurement technology provides 3D data that is more comprehensive than the linear profile tracing method. Although some analysis of 3D surface topography has been carried out, few parameters and approaches to characterizing 3D surfaces have been proposed because of the complexity of surfaces and mathematical description difficulties. Thus a set of parameters for characterizing 3D surface texture needs to be developed. Dong and Stout *et al.* [22][23][24][34][35][36][37] had done some works on extending the 2D parameters to characterize 3D surfaces. Based on the understanding of intrinsic properties of surface topographic features and parameters, a primary 3D parameter set was proposed in their papers. Some of the parameters included in the primary parameter set were extended from their 2D counterparts; others were specifically defined for characterizing 3D surface topography. Evidence was given to support the reasons for inclusion of each parameter in the set. Besides the mathematical/statistical background of the parameters, the experimental results were also obtained by testing a wide range of engineering surfaces to justify the proposal. There are also some other people working on 3D surface characterization and they have made significant contributions [38][39][40][41][42].

Most of the previous work on 3D surface characterization was focused on surface tribological properties, and their works are meaningful for some rotational and moving components. The extracted 3D surface features/parameters were from surface roughness domain (small scale). However, there is little work done on extracting 3D surface features from waviness domain (middle spatial frequency domain) and utilizing these features to characterize other surface functional performances such as sealing, or to defect problems in the machining process, such as tool wear, tool breakage. One basic reason for the limitation of the previous work is that, the current 3D surface measurement technologies have very small field of view, e.g. from 50 μm to 5 mm and the lateral resolution is normally from 0.25 μm to 0.5 μm. Although these measurement techniques are able to obtain 3D surface topography and have very high resolution, the small field of view property cannot provide comprehensive information for the large whole machined part. Besides this, the measurement speed of these methods is usually very slow, thus not capable of supporting the cycle time of the manufacturing process, therefore cannot be used for inline surface measurement and rapidly detecting problems in the machining process.

Recently, a novel laser holographic interferometer has been developed by Coherix *Inc.* [43], and this optical interferometer has the capability of measuring a workpiece surface as large as 300mm×300mm and generating a 3D surface height map within 40 seconds. To measure a surface larger than the field of view, multiple views of height maps can be accurately stitched together with cross-correlation software. The accuracy in the height direction can reach micron level. The lateral resolution is only 150 micron, but it is enough for analyzing surface features from middle spatial frequency domain (feature size larger than 300micron). Therefore, this 3D surface height measurement instrument provides an unprecedented platform to develop filter methods to extract 3D surface features from the middle frequency domain and use these features to predict some important surface functional performances and detect machining error.

A key problem for this research is to define and accurately extract 3D surface features that characterize surface properties in such a way that they correlate well with surface functional behavior and machining process which produces the surface. Therefore, in this research, based on the large field of view 3D surface height map measured by the holographic interferometer, filter methods will be specially designed to accurately extract multiple-scale 3D surface texture features and applied these features to correlate to some surface functional performances and detect errors in the machining process.

Besides extracting 3D surface texture features, this research will also analyze abnormal surface features: surface defects. Defect inspection is important for quality assurance of critical mating/sealing surfaces in automotive powertrain manufacturing. The presence of surface porosity and other types of surface defects located on nominally flat surfaces may cause serious coolant, oil, or combustion gas leakages. Therefore 100% inline inspection plays an important role for improving product quality.

Although the techniques of image processing and machine vision have been applied to machined surface inspection and well improved in the past 20 years, in today's automotive industry, surface porosity inspection is still done by skilled humans, which is costly, tedious, time consuming and not capable of reliably detecting small defects. Current machine vision systems cannot reliably distinguish porosity from similar shape 2D blemish, therefore has an unsatisfied false alarm rate. Also current methods cannot classify different types of surface defects which are problematic to the automotive powertrain manufacturing.

Therefore an automated surface defect detection and classification system for mating/sealing surfaces is desired. Our newly constructed machine vision system should have the ability to reliablely detect, distinguish and classify different types of surface defects commonly found on the mating/sealing surfaces, such as porosity, 2D blemish, residue dirt, scratch, and gouge. The cycle time of this system should be sufficiently fast thus the implementation of 100% inline inspection is feasible.

1.2 Research Objectives

The ultimate goal of this research is to reliably extract multiple scales of 3D surface features and apply these features to characterize workpiece functional performance, discover issues in the machining process, and detect and classify certain classes of surface defects that are problematic to manufacturing process. Specific objectives of this research are identified as follows:

(1) To design a filter method to accurately extract 3D surface waviness features from surface height map measured by the large field of view holographic interferometer. As described before, the advantages of this measurement technology are the speed and large field of view. But the disadvantage is that the result contains large amount of noises, and also because of the large field of view, the distortion of the surface is much larger than a smaller field of view height map. Therefore, the waviness extraction filter should be designed to overcome these disadvantages and extract 3D surface waviness without distortion. In addition to developing the feature extraction method, a 3D surface waviness feature will be extracted as an indicator to detect tool severe wear as a case study of using 3D surface features to detect errors in the machining process.

(2) To develop a wavelet transform method to decompose 3D surface into finer scale subsurfaces and extract multiple-scale features from the subsurfaces to better characterize functional performances of a surface and detect machining error. Through the multi-scale decomposition, 3D surface height data will be converted into the surface representations in different scales. Wavelet filter and related algorithms will be designed to automatically separate surface features at various zooming scales. Several automotive parts will be analyzed in order to demonstrate that the extracted 3D surface features from different

scale subsurfaces can used to characterize surface functional performances and detect problems in the machining processes.

(3) To design and construct an automated, reliable and fast surface defect detection and classification system which can accurately detect and identify surface porosities and other types of surface defects, e.g. residue dirt, 2D blemish, scratch and gouge. This system is designed to reliably detect the actual defects, achieve a very low rate of false detections, and has the ability to detect the defects with a minimum dimension larger than 300 microns. According to the requirements, a single camera machine vision system will be designed with LED illuminators illuminating the target surface from multiple directions. Related algorithms will be developed to realize defect detection and classification. Following this, the system will be then tested on actual automotive machined parts to demonstrate that the microscopic surface defects can be accurately detected and assigned to a surface defect class.

1.3 Organization of Dissertation

This dissertation contains five Chapters. Chapter 1 provides a brief description of the motivation and objectives of this doctoral research. Chapter 2 describes the proposed filter method to extract 3D surface waviness features and its application to detect severe tool wear. The correlation experiments between 3D surface features and tool conditions are performed on different cutter types, workpiece materials and cutting conditions. Chapter 3 focuses on developing multiple-scale wavelet surface decomposition method and applying it for workpiece surface functional performances prediction and machining errors detection. In this chapter, the 2D wavelet decomposition approach on 3D surface is developed. Case studies of four machined surfaces are demonstrated. In Chapter 4, a novel machine vision system has been designed and constructed to detect and classify abnormal surface features: surface defects. This system is designed based on 16 LED blocks illuminating the target surface from multiple directions. Related image processing algorithms are developed to realize the detection and classification of 5 types surface defect commonly found on mating/sealing surfaces. One artificially machined surface and two actual automotive parts are tested on this system. Finally, Chapter 5 provides the conclusions of this research, future work and contributions.

CHAPTER 2

3D SURFACE WAVINESS FEATURE EXTRACTION AND APPLICATION TO SEVERE TOOL WEAR ESTIMATION

2.1 Introduction

A surface is typically decomposed into three spatial frequency domains, the large frequency components are considered as roughness; the small frequency components are referred to as form; the medium frequency components are treated as waviness [1][2]. Surface features extracted from different frequency bands can be utilized to detect various problems in the manufacturing process. Waviness feature is considered as an important symptom of machine tool behaviors [1], and some challenging problems in the manufacturing process can be understood and solved in an easier way by studying waviness.

As described in the previous chapter, 3D surface height map of a large workpiece (e.g., 300mm×300mm) can be measured by the holographic interferometer within 40 seconds. Although the lateral resolution of the height map is only 150 micron, this interferometer technique provides us an unprecedented platform to develop filter methods for 3D surface features extraction from the middle spatial frequency domain (waviness domain) and use these features to characterize some important surface properties or address machining problems. Most of the previous work on 3D surface characterization has focused on surface tribological properties, these properties are important for rotational and moving components. However, little work has been done on extracting 3D surface waviness features and utilizing these features to characterize surface functions other than tribological properties or to detect machining errors, such as tool wear, tool breakage.

Therefore, this chapter will focus on designing a filter method to accurately extract 3D surface waviness from the surface height map measured by the interferometer and applying the waviness feature of workpiece to detect severe tool wear as an application example. The large field of view 3D surface height map based on the interferometer measurement can provide comprehensive information for the surface condition, but the result contains large amount of noises and because of the large field of view, the surface distortion cannot be neglected. Therefore, the feature extraction filter should have the ability to remove the measurement noises and surface distortion which may otherwise affect the waviness extraction result.

Generally in the automotive industry, the standard spatial cutoff wavelengths for surface waviness are: 0.8mm, 2.5mm and 8 mm [2]. The wavelengths of surface components longer than cutoff wavelength will have their amplitude transmitted as waviness. The lateral resolution (pixel size) of the holographic interferometer is 150 micron, therefore compared with the cutoff wavelengths:

- 0.8 mm spatial wavelength cutoff equals to 5.33 pixels
- 2.5 mm spatial wavelength cutoff equals to 16.67 pixels
- 8.0 mm spatial wavelength cutoff equals to 53.3 pixels

Even the smallest cutoff wavelength (0.8 mm cutoff) is within approximately a spatial frequency octave of the theoretical Nyquist limit for data sampling and signal information retention. Therefore, the lateral resolution of this interferometer is capable of providing surface waviness for most manufacturing industry cases.

Following the design of filtering method, some correlation experiments are performed to use 3D surface waviness feature of the workpiece to detect severe tool wear in the machining process. The purpose of these correlation experiments is to demonstrate an industry application example of using 3D surface waviness feature. Accurate on-line tool condition monitoring is important for improving process efficiency, ensuring product quality and reducing unnecessary tool change costs as well as machine downtime. The ability to disengage the tool prior to catastrophic failure reduces manufacturing costs and excessive machine deterioration. Therefore, tool condition monitoring has been the subject of considerable research. In this chapter, we present a new way to determine the wear conditions of a cutting tool based on the 3D surface waviness feature of the workpiece.

In general, tool wear assessment methods can be classified as either direct or indirect. In the direct approaches, machine vision systems are usually employed to capture the images of the tool's cutting edge and monitor tool wear based on these images [44][45][46][47]. These techniques are highly dependent on the reflectance, color and specularity of the tool edges as well as the illumination conditions of the light source. Moreover, results may be sensitive to coolants and coolant mists. Indirect tool wear monitoring on the other hand can be achieved by measuring cutting force, torque, or vibration, acoustic emission produced during machining [48][49][50][51][52][53][54][55][56][57]. These methods require sensor systems which are usually expensive and difficult to install and maintain. Also, the signal to noise ratio is often small, leading to inaccuracies and false alarms.

Estimating tool wear conditions using 3D surface features of the workpiece is an indirect method. This method provides a spatial signature of the interaction between tool's cutting edge and the part surface [58][59]. However, because of the limitations of the previous measurement techniques, considerably less work has been successfully performed of using 3D surface texture features to assess tool wear. A line profile of a surface obtained from the stylus profilometer or point-based measurement system is highly localized and 2D parameters extracted from the profile cannot reliablely represent the characteristics of the whole surface. 3D surface features extracted from large field of view workpiece surface height map provide more comprehensive information thus can be used to detect tool wear.

The rest part of this chapter is organized as follows: section 2.2 introduces the design of filter method for 3D surface waviness extraction. Section 2.3 presents the correlation studies of applying 3D surface features to detect severe tool wear for both aluminum workpieces and compacted graphite iron (CGI) workpieces This chapter is concluded in section 2.4.

2.2 Filter Design for 3D Surface Waviness Extraction

2.2.1 Transmission Properties and Limitations of Standard Gaussian Filter

Researchers developed different filter methods to decompose an engineering surface into different frequency bands as mentioned in chapter 1. There are several general requirements for the filter design [24]: firstly, the use of surface filtering must be justified by the application, there is not a universal filter good for any applications; secondly, only linear or zero phase filters are to be used for topographic component separation; thirdly, the surface filter should have a gradual fall-off impulse response thus to avoid the ringing effect associated with sharp cut-off.

Among the filter methods, the analog 2RC filter has serious phase distortion and has rarely been used now. Gaussian filter is a good choice because of its zero phase transmission characteristic, and 50% amplitude transmission at its cutoff wavelength makes it the most straightforward filter method to extract waviness. But it has edge distortion and performs poorly on the surface with large form distortion and sharp peaks/valleys/noise. Many kinds of spline filters have been recently designed to have the transmission characteristics comparable to Gaussian filter while the edge distortion has been reduced. Nevertheless, the spline filters have too many parameters that need to be defined which makes the use of these methods complicated and less flexible. After studying the properties of these filter techniques, Gaussian filter is chosen as the basic method to extract 3D surface waviness. (See the next page for some explanation of this selection.)

The weighting function (impulse response) of 2D Gaussian filter is written as [2][6]:

$$S(x,y)=\frac{1}{\beta\lambda_{xc}\lambda_{yc}}\exp\left\{-\frac{\pi}{\beta}\left[(\frac{x}{\lambda_{xc}})^2+(\frac{y}{\lambda_{yc}})^2\right]\right\} \tag{2.1}$$

Where $\beta = Int2/\pi = 0.2206$, x is the distance from the origin in the x axis, y is the distance from the origin in the y axis; λ_{xc} and λ_{yc} are the cutoff wavelengths in the x and y directions respectively. In our study, λ_{xc} = λ_{yc}=0.8mm, which is the typical cutoff wavelength defined for the surface waviness extraction in the automotive industry.

Gaussian filter is essentially a low-pass filter, and the frequency response function can be written as [24]:

$$\begin{aligned} \mathrm{H}(\omega_x,\omega_y) &= \exp\left\{-\pi\beta\left[(\frac{\omega_x}{\omega_{xc}})^2+(\frac{\omega_y}{\omega_{yc}})^2\right]\right\} \\ &= \exp\left\{-\pi\beta\left[(\frac{\lambda_{xc}}{\lambda_x})^2+(\frac{\lambda_{yc}}{\lambda_y})^2\right]\right\} \end{aligned} \tag{2.2}$$

Where ω_{xc} and ω_{yc} is the cut-off frequency at 50% attenuation ratio.

The 2D Gaussian weighting function (impulse response) with $\lambda_{xc} = \lambda_{yc}$=0.8mm is illustrated in Figure 2.1.

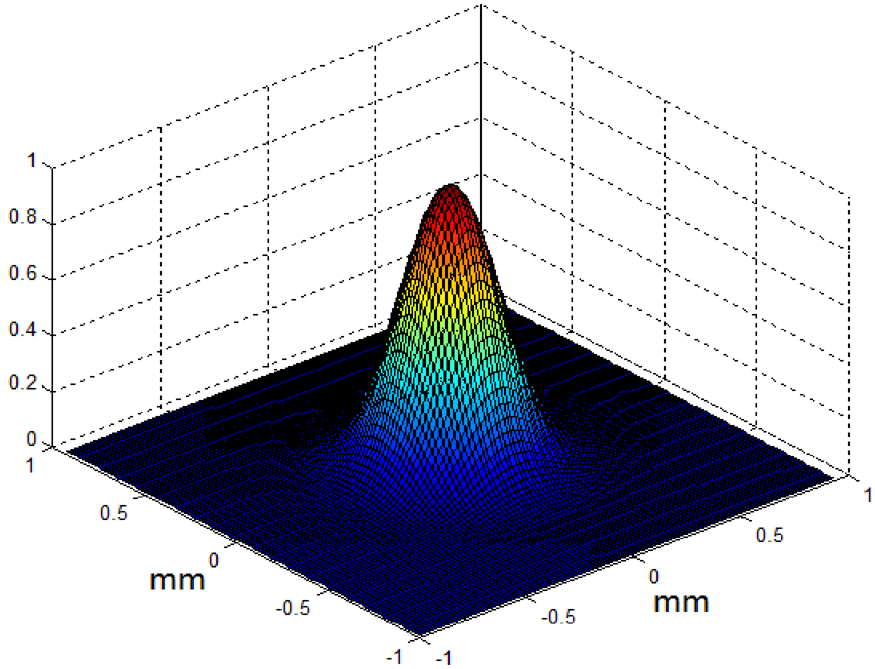

Figure 2.1 2D Gaussian filter weighting function ($\lambda_{xc} = \lambda_{yc}$=0.8mm).

Gaussian filter has some transmission properties which explain why it is chosen as the basic method for our application to extract 3D surface waviness.

1) Gaussian filter has a gradual fall-off, as shown in Figure 2.1, thus it avoids the ringing effect associated with sharp cut-off. It has 50% amplitude transmission occurring at the cutoff wavelength, wavelengths shorter than the cutoff will have their amplitude transmitted as roughness; wavelengths longer than the cutoff will have their amplitude transmitted as waviness. Hence, 3D surface waviness can be simply extracted by subtracting roughness from the surface.
2) Gaussian filter is a zero phase filter. As shown in equation 2.2, the frequency response $H(\omega_{xc},\omega_{yc})>0$ over the entire frequency domain, therefore, both the high frequency and low frequency can be extracted with a single filtering procedure without phase distortion.
3) 2D Gaussian filter is symmetric and separable: $H(\omega_{xc},\omega_{yc})= H(\omega_{xc})H(\omega_{yc})$, therefore practically, when applying 2D Gaussian filter to decompose a large 3D surface (e.g., 4 million data points), the separability enables the separate filtering of successive profile in one direction, followed by the same operation in the other, thus greatly simplifies the implementation and brings computational efficiency and conceptual simplicity.
4) Gaussian filter is straightforward and well accepted in the automotive industry, and only one parameter (cutoff wavelength) needs to be specified when applying Gaussian filter, thus production engineers are comfortable working with it.

However, Gaussian filter has some limitations including edge distortion and poor performance on surface profile with large form distortion and sharp peaks/valleys/noise. The 3D surface height map we used is measured by the optical holographic interferometer, which has large amount of noises. Besides, because of this measurement technique can measure a large field of view surface, the surface form distortion of the height map is much larger than the small field of view height map. Therefore, an improved Gaussian filter will be developed to overcome the disadvantages of the standard Gaussian filter and extract 3D surface waviness accurately.

2.2.2 Design of Improved Gaussian Filter

The structure of our improved Gaussian filter is shown in Figure 2.2. There are four steps in the improved Gaussian filter. The detail of each step will be explained in following sub-sections.

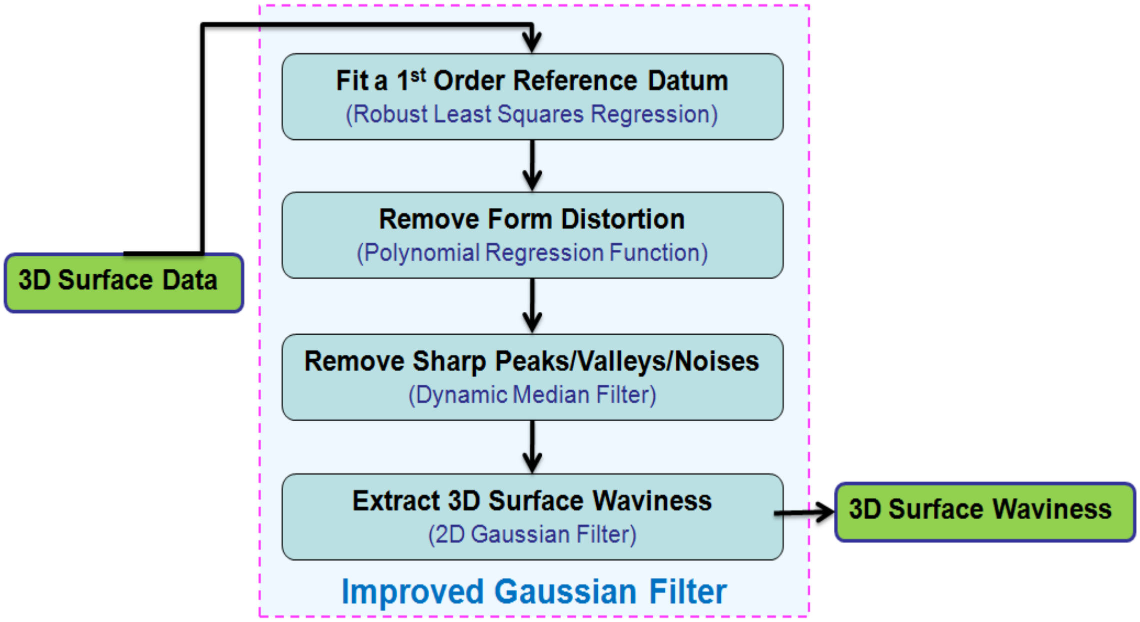

Figure 2.2 Structure of improved Gaussian filter.

2.2.2.1 Fitting of a 1^{st} Order Reference Datum to the Surface

In the first step of the improved Gaussian filter, a 1^{st} order reference datum plane is required for nominally flat 3D surface characterization. The purpose of this step is to fit a reference datum plane to the surface thus to remove the linear trend of the surface and to level the raw topographic data. Basically, a reference datum plane is a base to which parameters can be referred. In most cases, the least squares mean plane will be used as the reference datum, and it is well defined in mathematics: a plane such that the sum of the squares of asperity departures from this plane is a minimum. By this definition, the least squares mean plane is unique for a given surface and it minimizes the root mean square height in comparison with other planes, thus this eliminates any uncertainty in finding the plane.

However, when there are significant outliers, the normal direction of the least squares mean plane may be influenced by the outliers thus not conform to the normal direction of the measured surface anymore. An example of an unprocessed 3D surface height data measured by the holographic interferometer is shown in Figure 2.3. We can see lots of sharp peaks/valleys/noise on the raw data.

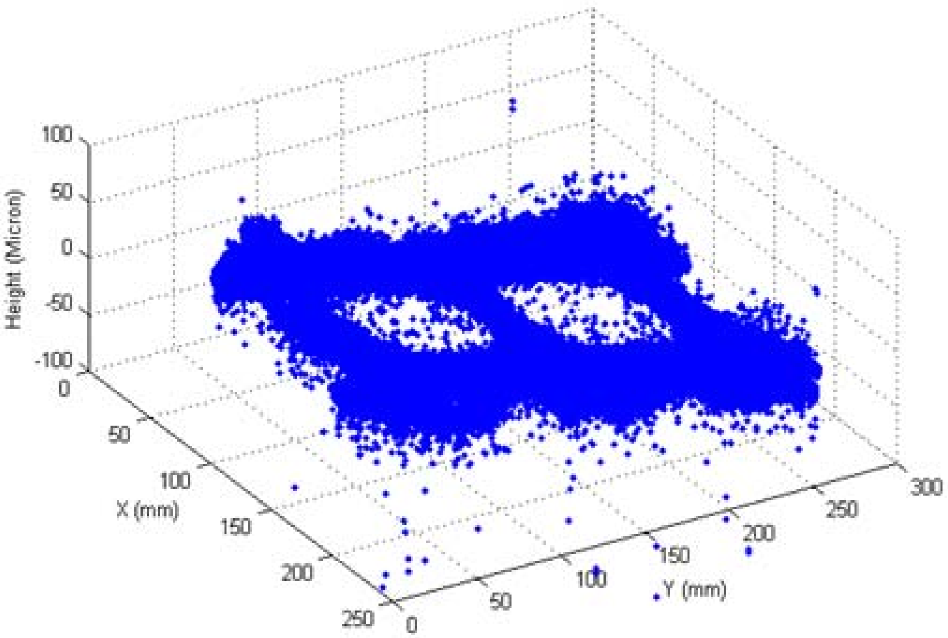

Figure 2.3 An example of a 3D surface of a cylinder head.

In this case, robust least squares mean plane can be employed. It is an iteratively reweighted least squares fitting, which tends to diminish the influence of outliers compared with the ordinary least squares fitting [60]. The weights to be used are related to residuals of the surface with respect to the former least squares mean plane. It can be shown that such a reweighted least squares mean plane would be convergent to the plane where no outliers exist, hence conforming the normal direction of the robust least squares mean plane to the normal direction of the measured surface [60]. Figure 2.4 shows the robust least squares mean plane of the example in Figure 2.3, an example of a 3D surface of a cylinder head.

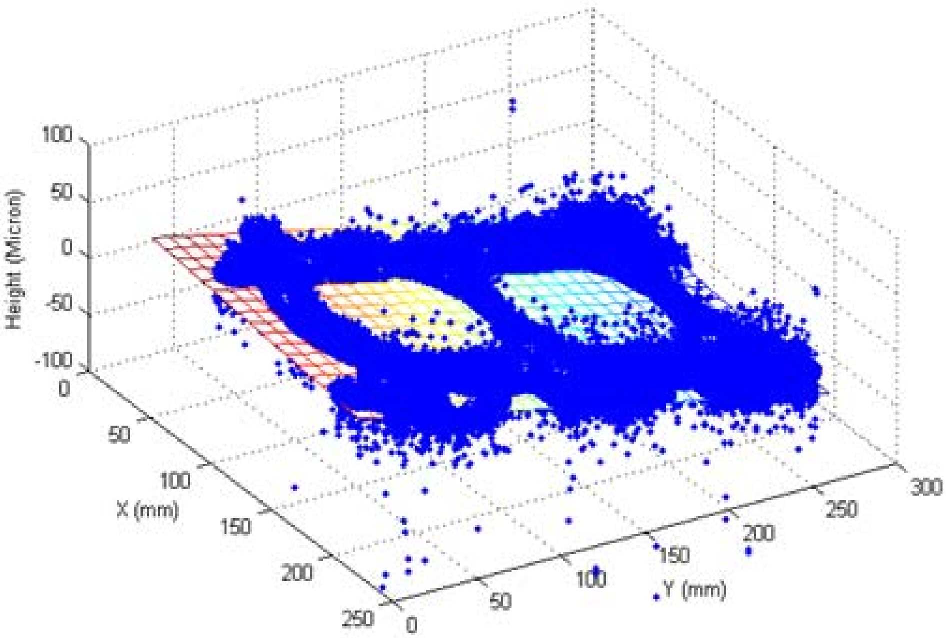

Figure 2.4 An example of a 3D surface of a cylinder head with a robust least squares mean plane.

2.2.2.2 Removal of the Large Form Distortion of the Surface

The robust least squares mean plane described above is a first order linear plane which fits onto a nominally flat surface. In our application, many large engineering surfaces, such as cylinder head surface, transmission valve body and so on are all nominally flat surfaces, but actually slightly curved because of the machining processes. To extract and characterize surface waviness, 3D form curvatures have to be removed. A way to deal with this problem is to fit a least squares polynomial surface. This is a very widely used method to fit either partial cylindrical forms, partial spheres or arbitrary curved forms [61][62].

Again, for a surface with large amount of noises, robust least squares fitting (iteratively reweighted least squares) as described in the previous step is applied to reduce the effect of the outliers. Another important issue in this step is how to determine the order of the polynomial surface. Usually it is not so straight forward to determine what order of a polynomial surface is the best fit to a curved surface and how good the surface fitting would be. The goodness-of-fit depends statistically and problematically on the criteria selected. Here R^2 value is used to evaluate the goodness-of-fit [63]. R^2 coefficient of determination is a statistical measure of how well the regression line approximates the real data points, as defined in equation 2.3, where y_i is measured data which has already been divided by a weight factor from the last iteration of the robust least squares fitting and f_i is modeled (predicted) data. An R^2 of 1.0 indicates that the regression surface perfectly fits the data.

$$R^2 = 1 - \frac{\sum_i (y_i - f_i)^2}{\sum_i (y_i - \bar{y})^2} \tag{2.3}$$

Table 2.1 lists the R^2 values of the first order, second order and third order polynomial regression surfaces for the cylinder head surface example shown in Figure 2.3. It can be seen from Table 2.1 that, when the order of the polynomial increases from the first order to the second order, R^2 value increases; when the order increase from the second order to the third order, the R^2 value remains almost the same. Therefore, the second order polynomial regression model is selected. A higher order regression model is not desirable since it will largely increase the processing time and cause over-fit problem. Figure 2.5 shows the cylinder head surface with a second order polynomial regression surface. Figure 2.6 shows the 3D height map after the form distortion is removed. For this example, the first order polynomial regression function can also be adequate.

Table 2.1: R^2 values of polynomial regression surfaces of a cylinder head surface.

Order of Polynomial	Number of Coefficients	R^2 Value
1	3	0.9769

2	6	0.9806
3	10	0.9808

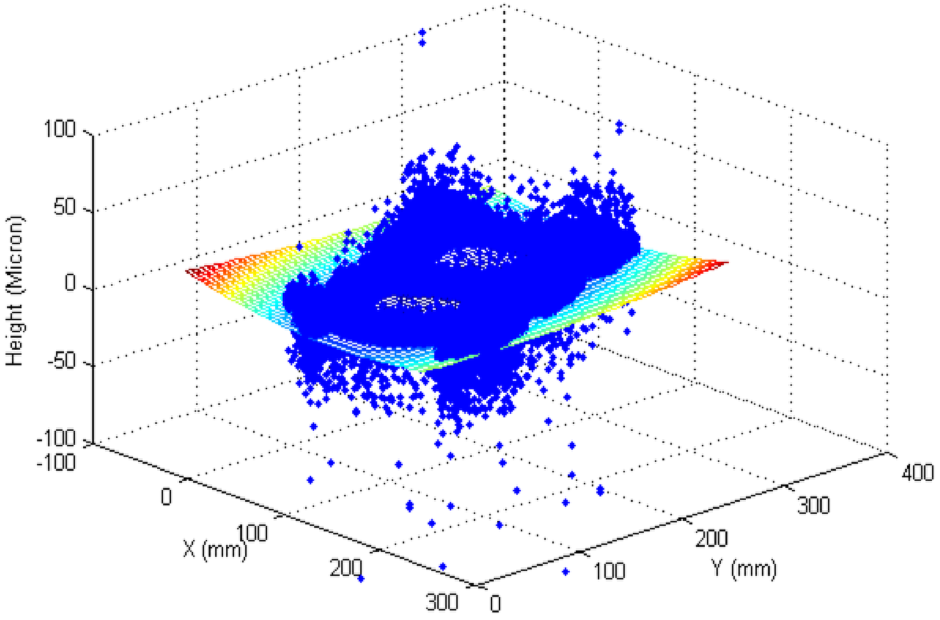

Figure 2.5 3D cylinder head surface with a second order polynomial robust least squares regression surface.

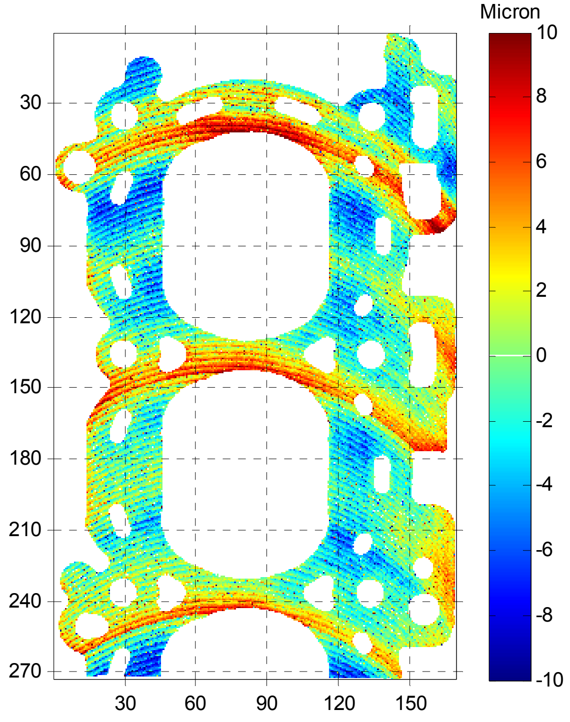

Figure 2.6 3D surface height map of a cylinder head surface after removal of large form distortion.

This step is extremely important for a large and thin workpiece such as an automotive transmission valve body, which may have a significant form distortion because of the clamping during the machining process. An example of a valve body surface is shown in Figure 2.7. The R^2 values of polynomial regression surfaces are shown in Table 2.2, we can see clearly that when the order of the polynomial increases from the first order to the second order, R^2 value increases significantly; when the order increases from the second order to the third order, the R^2 value increases not significantly. Therefore, the second order polynomial regression model is adequate. Figure 2.8 shows the surface height map after the removal of the quadratic form shape, we don't see a bending shape anymore.

Table 2.2: R^2 values of polynomial regression surfaces of a transmission valve body surface.

Order of Polynomial	Number of Coefficients	R^2 Value
1	3	0.0412
2	6	0.9720
3	10	0.9818

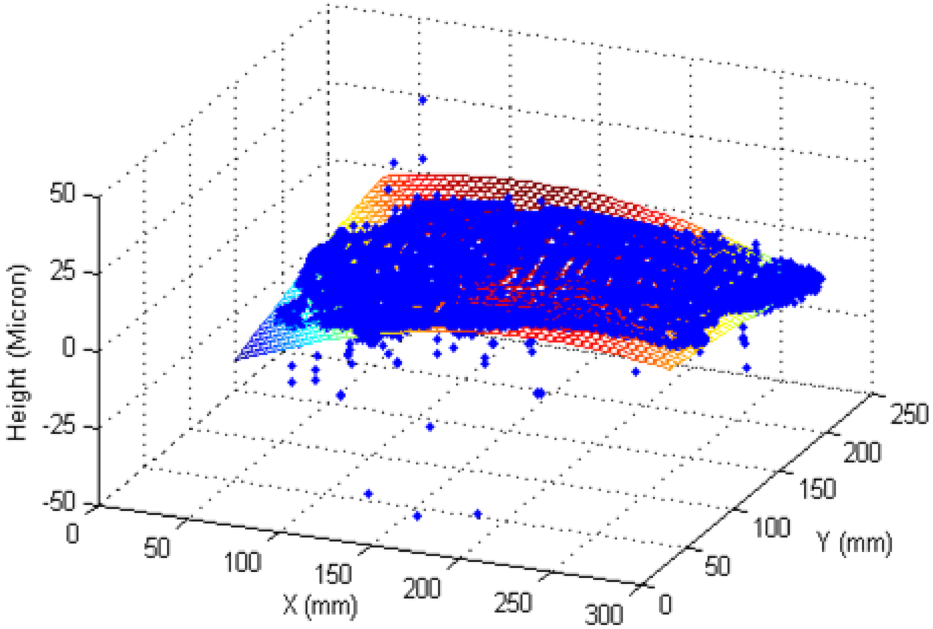

Figure 2.7 3D valve body surface with a second order polynomial robust least squares regression surface.

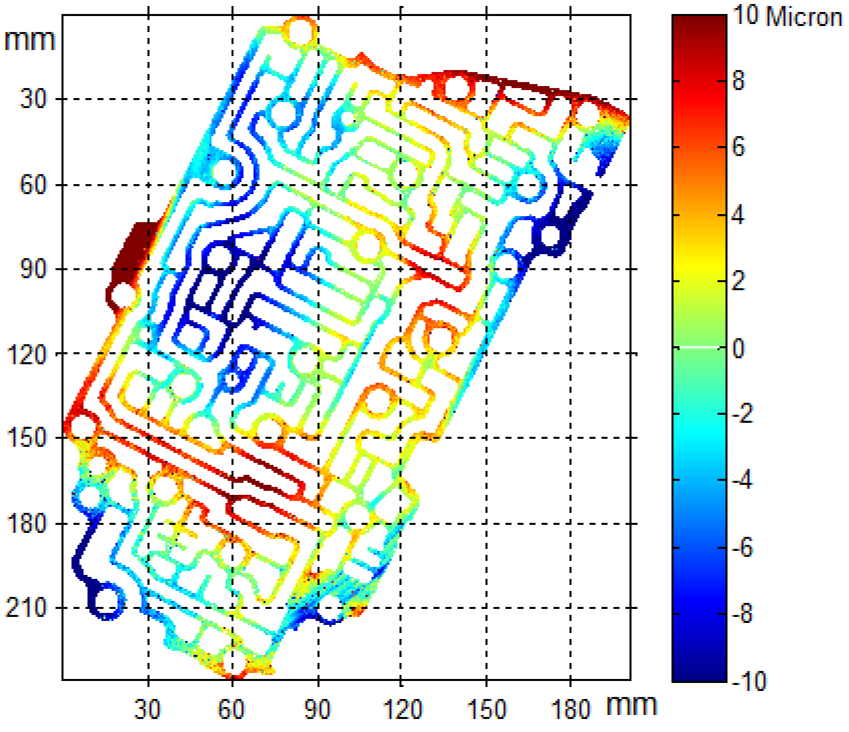

Figure 2.8 3D surface height map of a valve body surface after removal of large form distortion.

2.2.2.3 Removal of Sharp Peaks/Valleys/Noise

After the linear trend and the form distortion of the surface were removed, a noise filter should be designed and applied to the surface in order to efficiently remove the large amount of sharp peaks/valleys and measurement noise which may otherwise affect the waviness extraction result. In our case, the height map contains important tooling mark information (key waviness components), thus a good noise filter should incorporate the ability to preserve the sharpness of the tooling marks. An unsuitable filter choice would result in useful information being destroyed or noise remaining. Therefore, a "dynamic median filter" is designed based on our specific requirements.

Median filter was introduced in 1974 by Tukey [64], who used the moving median as a smoothing technique in time series analysis. Median filter has also been used for enhancing images, Pratt [65] made a qualitative study of two dimensional median filters of various sizes and shapes and he concluded that the median filter is extremely useful for suppressing impulsive and 'salt and pepper' noise. However, median filter and many of its variants have limitations like blurring of image details due to simultaneous noise and signal suppression of median filter affecting the image fidelity badly. Researchers are trying to build median filters which will replace only the noise corrupted pixels while preserving uncorrupted pixels [66][67][68][69][70][71][72].

Median filter considers each pixel in the image in turn and looks at its neighbors (e.g., a 3×3 window size, each pixel has 8 neighbors) to decide whether or not it is representative of its surroundings by choosing a fixed threshold, if not, replaces it with the median of those neighbors. The median is calculated by first sorting all the pixel values from the surrounding neighborhood into numerical order and then replacing the pixel being considered with the middle pixel value. By applying median filter, most of the sharp peaks/valleys and measurement noises will be removed, however, in our case, the tooling marks information on the surface height map which belongs to the surface waviness domain may also be smoothed. For some roughly machined surface, the height map measured by the optical interferometer may contain large amount of noises, the median filter needs to be applied several times to completely remove the noises, but the side effect is that the tooling marks may be washed out with the noises.

Therefore, a dynamic median filter is designed to remove the sharp peaks/valleys/noises, but preserve the sharpness of the tooling marks. For the dynamic median filter, a dynamic threshold based on statistical analysis of the whole surface height data will be selected and recalculated in each iteration. Compared to the ordinary median filter, which selects a fixed threshold only based on the surrounding neighborhood, the dynamic median filter is more robust and flexible. It selects a threshold based on the statistical study of the surface.

First, for each pixel on the surface, find the median value of its 8 surrounding neighborhood (3×3 window size), then calculate the difference between the pixel value and the median value of the neighbors, we use d_i to represent this value, $i=1,2,\dots, N$, where N is the total number of pixels on this surface; then draw a histogram chart of all d_i for this surface, identify the standard deviation δ for all d_i. In the dynamic filtering process, we apply the dynamic median filter several times, for each iteration, we recalculate d_i and δ values, the threshold values are listed in Table 2.3, where δ_j is the recalculated standard deviation at iteration j. The total number of iterations is limited by

10, however, the noise removal power is designed to be decreasing when applying more iterations. For most cases, after iteration 3, the filter does not remove much noise.

Table 2.3: Threshold value for each iteration of the dynamic median filter

Iteration	1	2	3	4	5	6	7	8	9	10
Threshold	$3\delta_1$	$3.3\delta_2$	$3.6\delta_3$	$3.9\delta_4$	$4.2\delta_5$	$4.5\delta_6$	$4.8\delta_7$	$5.1\delta_8$	$5.4\delta_9$	$5.7\delta_{10}$

Figure 2.9 shows an example of comparing the reconstruction results by the ordinary median filter and dynamic median filter, this example is selected from a cylinder head surface. Figure 2.9 (a) is the raw height map, Figure 2.9 (b) is the height map filtered by median filter, and Figure 2.9 (c) is the result filtered by the dynamic median filter. It can be seen from the results that, both the median filter and dynamic median filter can remove the impulsive noises, but the dynamic median filter can preserve the sharpness of the original data better, the median filter blurs the details on the height map and smoothes the peaks of the tooling mark.

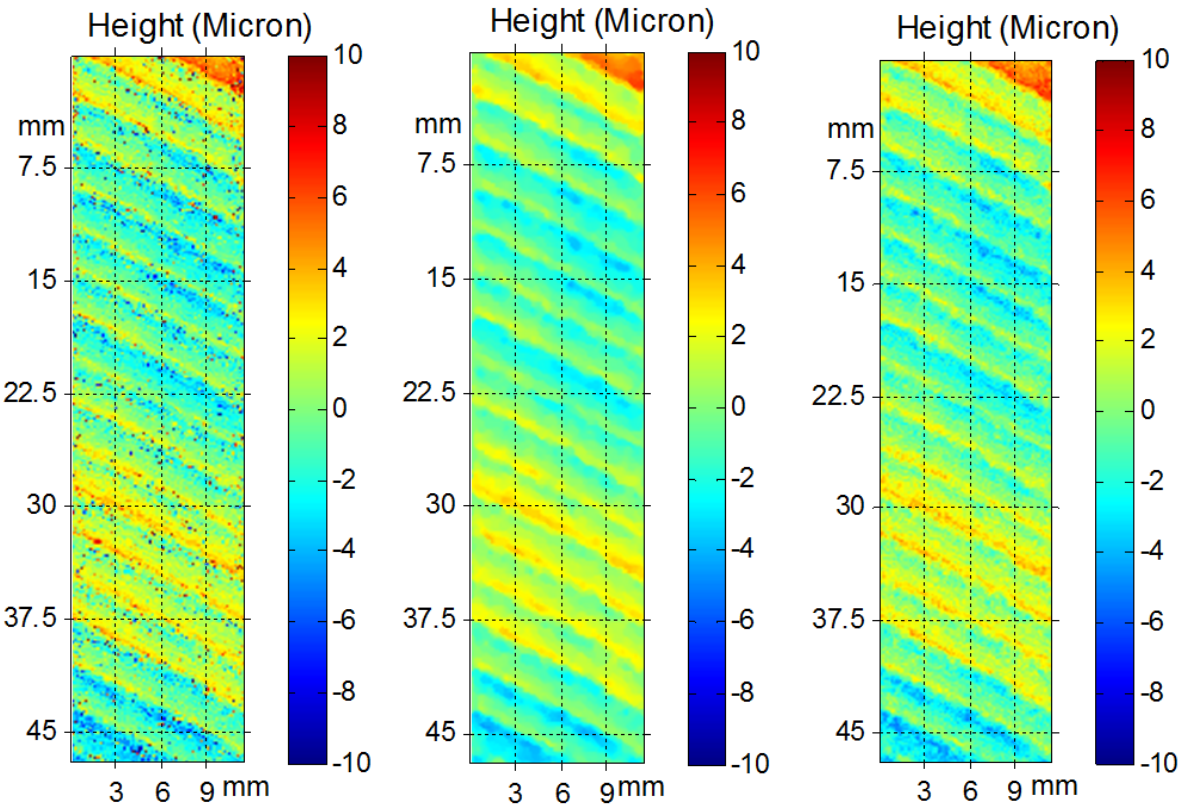

(a) (b) (c)

Figure 2.9 Compare the results of ordinary median filter and dynamic median filter: (a) original surface height map, (b) result filtered by ordinary median filter, (c) result filtered by dynamic median filter.

To better compare the results filtered by the two filters, Figure 2.10 (a) shows a column section on the result of applying ordinary median filter, we can see that, the noise suppression of the ordinary median filter reduces the sharpness of the tooling marks thus affects the fidelity of the surface height map. Figure 2.10 (b) and (c) show the results of applying dynamic median filter, it can be observed from the height data after applying dynamic median filter in 3 iterations that the sharp peaks/valleys/noises are all removed while the tooling marks information is well preserved. By comparing the height data after applying dynamic median filter 3 iterations and 10 iterations, we can see that, not too many more peaks/valleys are removed after 3 iterations. This is example is representative for the aluminum parts.

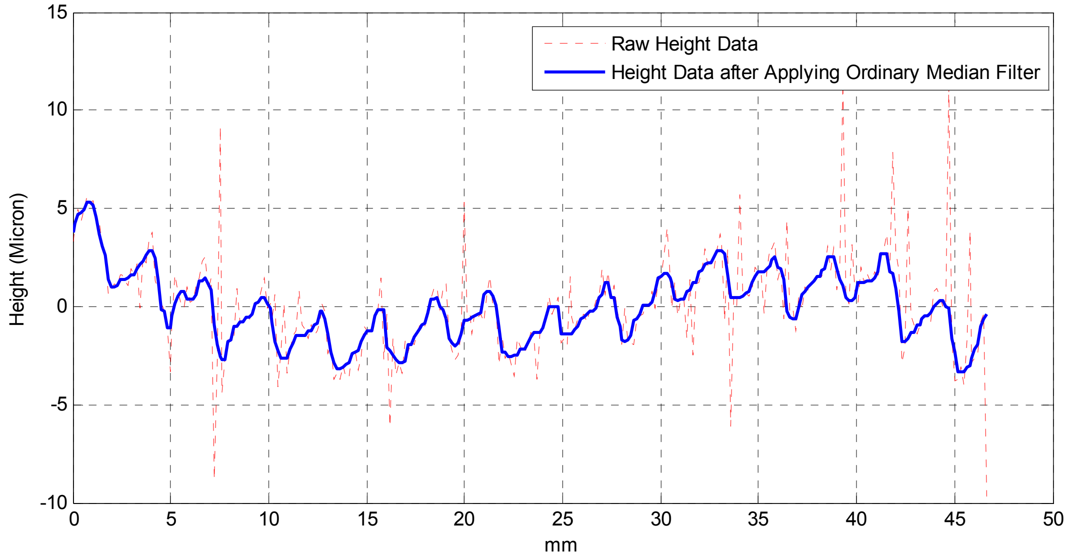

(a)

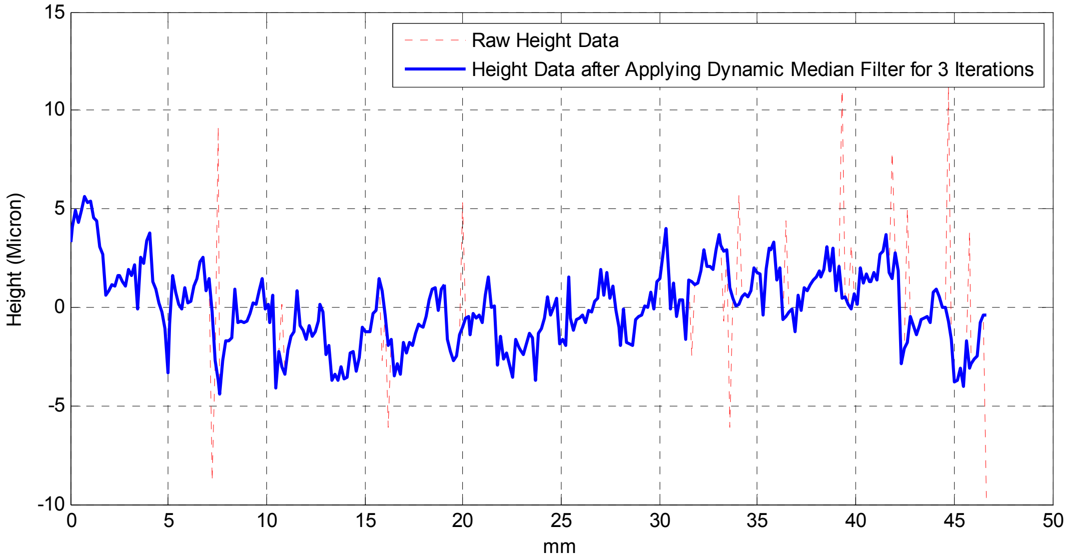

(b)

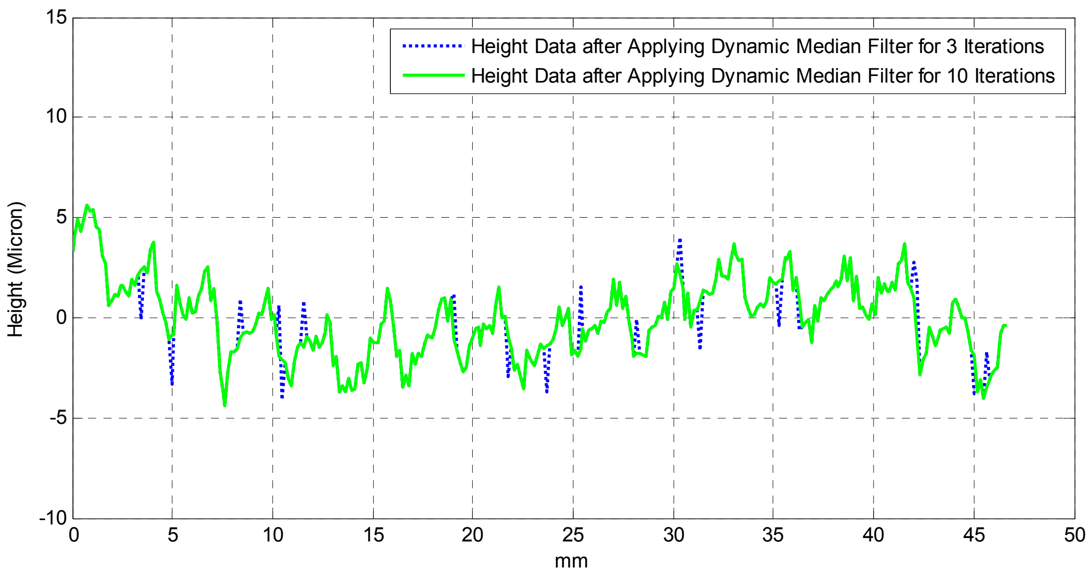

(c)

Figure 2.10 Compare the results of ordinary median filter and different iterations of dynamic median filter.

In order to measure the performance of the dynamic median filter, the most commonly used parameter: peak signal-to-noise ratio (PSNR) [73] is applied to evaluate the goodness of a noise filter. The equations listed below show the calculation logic of the PSNR. Where *I(i,j)* is the pixel height value on the original image, *K(i,j)* is the pixel height value on the reconstructed image, MAX_I means the maximum possible height value on the original image. PSNR is defined based on the mean squared error, and a higher PSNR would normally indicate that the reconstruction is of higher quality.

$$PSNR = 10 \cdot \log_{10}\left(\frac{MAX_I^2}{MSE}\right) \tag{2.4}$$

$$\text{MSE}=\frac{1}{\text{mn}}\sum_{i=0}^{m-1}\sum_{j=0}^{n-1}[I(i,j)-K(i,j)]^2 \tag{2.5}$$

Since in the real world, there is no way to obtain a surface height map without noises, therefore, we will simulate an original height map, then intentionally add some noises, then compare the filtered results with the original data. In Figure 2.11 (a), we simulated a surface which is similar to the machined surface with tooling marks, in Figure 2.11 (b), we added 10% impulsive noise to the original data. Figure 2.11 (c) shows the reconstruction height map after applying ordinary median filter. Figure 2.11 (d) is the result after applying dynamic median filter. We can see from the images that, the dynamic median filter preserves the sharpness of the tooling mark information better than the ordinary median filter.

The PSNR value (calculated base on equation 2.4 and 2.5) of the median filter for this example is 19 dB, and the PSNR for the dynamic median filter is 26dB, which indicates the dynamic median filter can reconstruct the original data at a higher quality.

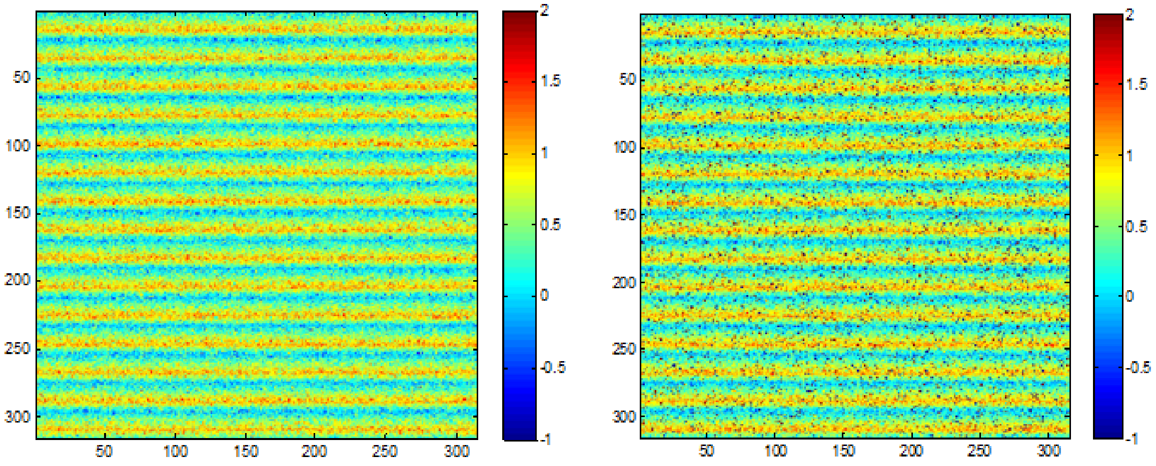

(a)

(b)

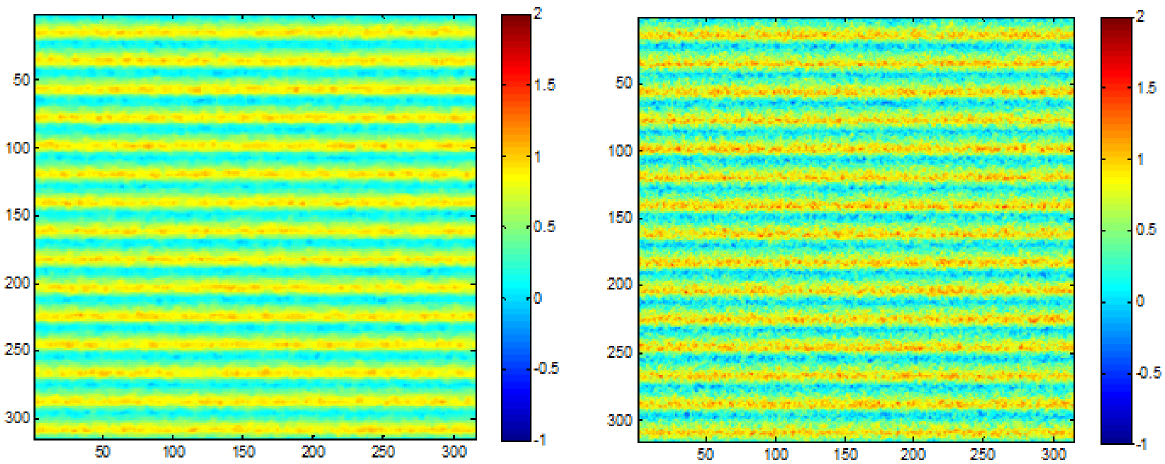

(c) (d)

Figure 2.11 (a) A simulated image, (b) 10% impulsive noises are added to the image in (a), (c) the reconstruction image of applying median filter on (b), (d) the reconstruction image of applying dynamic median filter on (b).

2.2.2.4 Extraction 3D Surface Waviness

After the previous three steps, 2D Gaussian filter as introduced in section 2.2.1 is then applied to extract 3D surface waviness. When 2D Gaussian filter is performed on finite-size image, edge distortion occurs, thus in the improved Gaussian filter, the first and last half cutoff wavelength is discarded in order to avoid edge distortion. Compared to the large dimensions of the surface data (300mm×300mm), discarding less than 1 millimeter edge data does not prevent us from collecting the entire surface information (cutoff wavelength is typically 0.8mm or 2.5mm, less than 1% data is discarded).

An example of 3D surface raw height data and waviness data extracted by a standard 2D Gaussian filter and the improved Gaussian filter are shown in Figure 2.12, here in order to show the data clearly, only a small area of the cylinder head surface is shown. It can be seen from the results that, standard Gaussian filter is seriously affected by the sharp peaks/valleys/noises on the surface; but the improved Gaussian filter is robust over these peaks/valleys/noises, thus can extract the surface waviness without distortion. Compared to the raw surface data, surface waviness data reveals purely the tooling mark features on the surface. Also, we can see from Figure 2.12 (c) and (d) that applying dynamic filters in more iterations will not affect too much of the waviness extraction result.

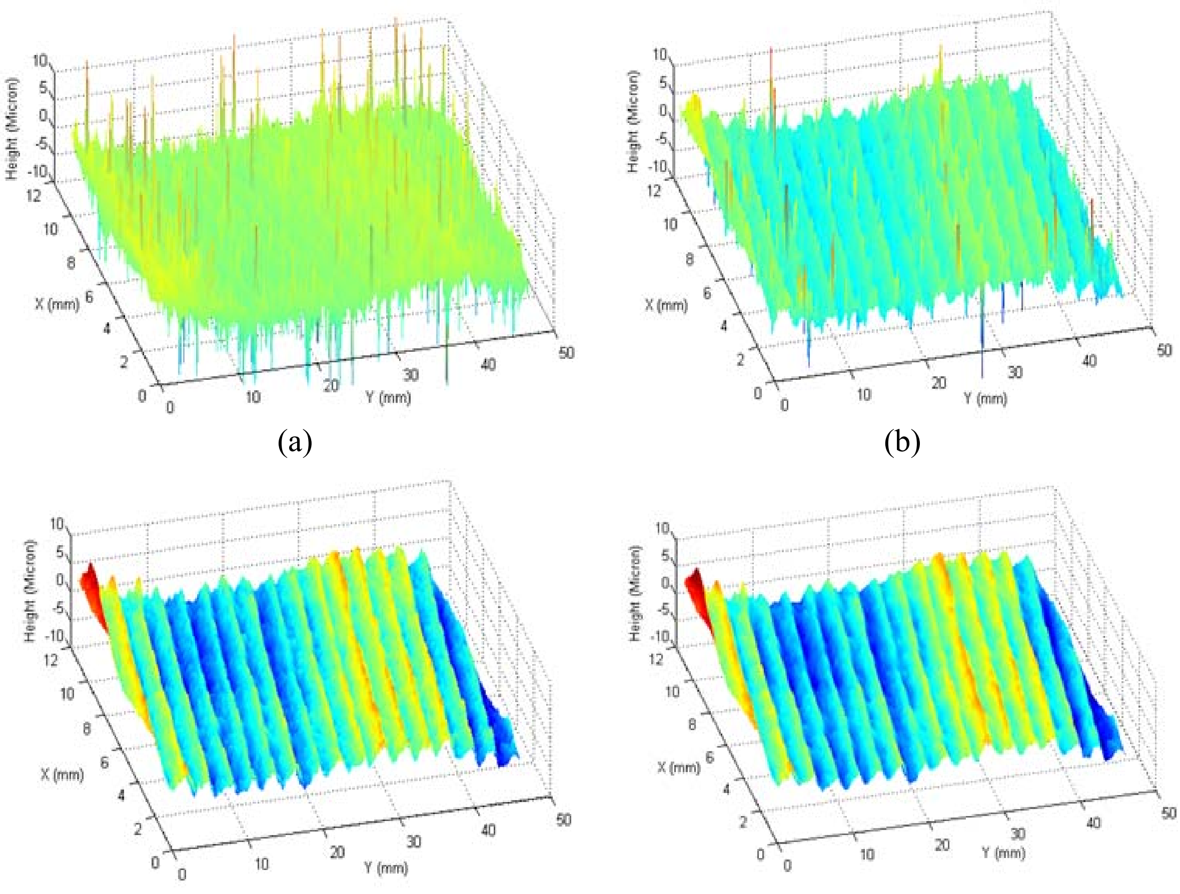

(a) (b)

(c) (d)

Figure 2.12 (a) An example of 3D surface height data, (b) 3D surface waviness extracted from the height map in (a) by standard Gaussian filter, (c) 3D surface waviness extracted by improved Gaussian filter (using dynamic median filter 3 iterations), (d) 3D surface waviness extracted by improved Gaussian filter (using dynamic median filter 10 iterations.

In order to compare the results more clearly, a line section on the surface is illustrated in Figure 2.13. We can see that, the waviness profile by applying the standard Gaussian filter is affected by the peaks/valleys/noises on the surface profile; but the improved Gaussian filter is not affected by these sharp peaks/valleys/noises, and Besides the noises, the high frequency components which belong to the roughness regime are also clearly separated from waviness. Also, in the noise filtering step, applying dynamic filter more than 3 iterations will almost not affect the waviness extraction result.

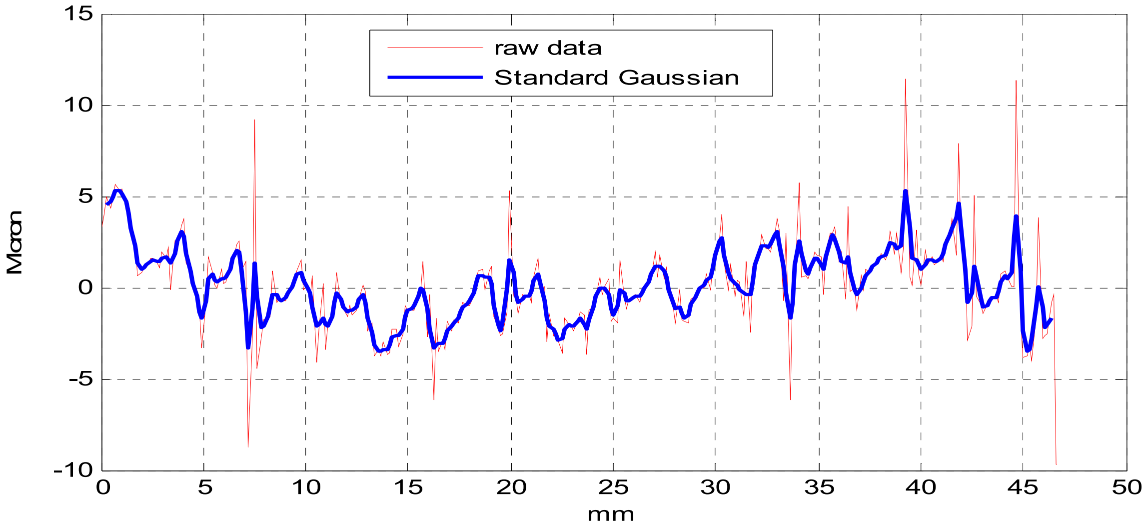

(a)

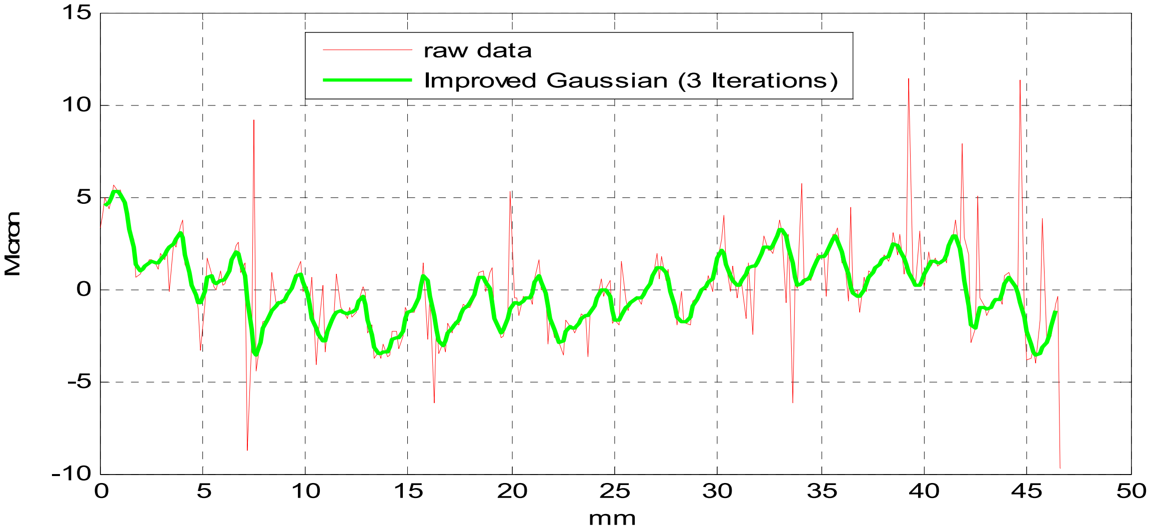

(b)

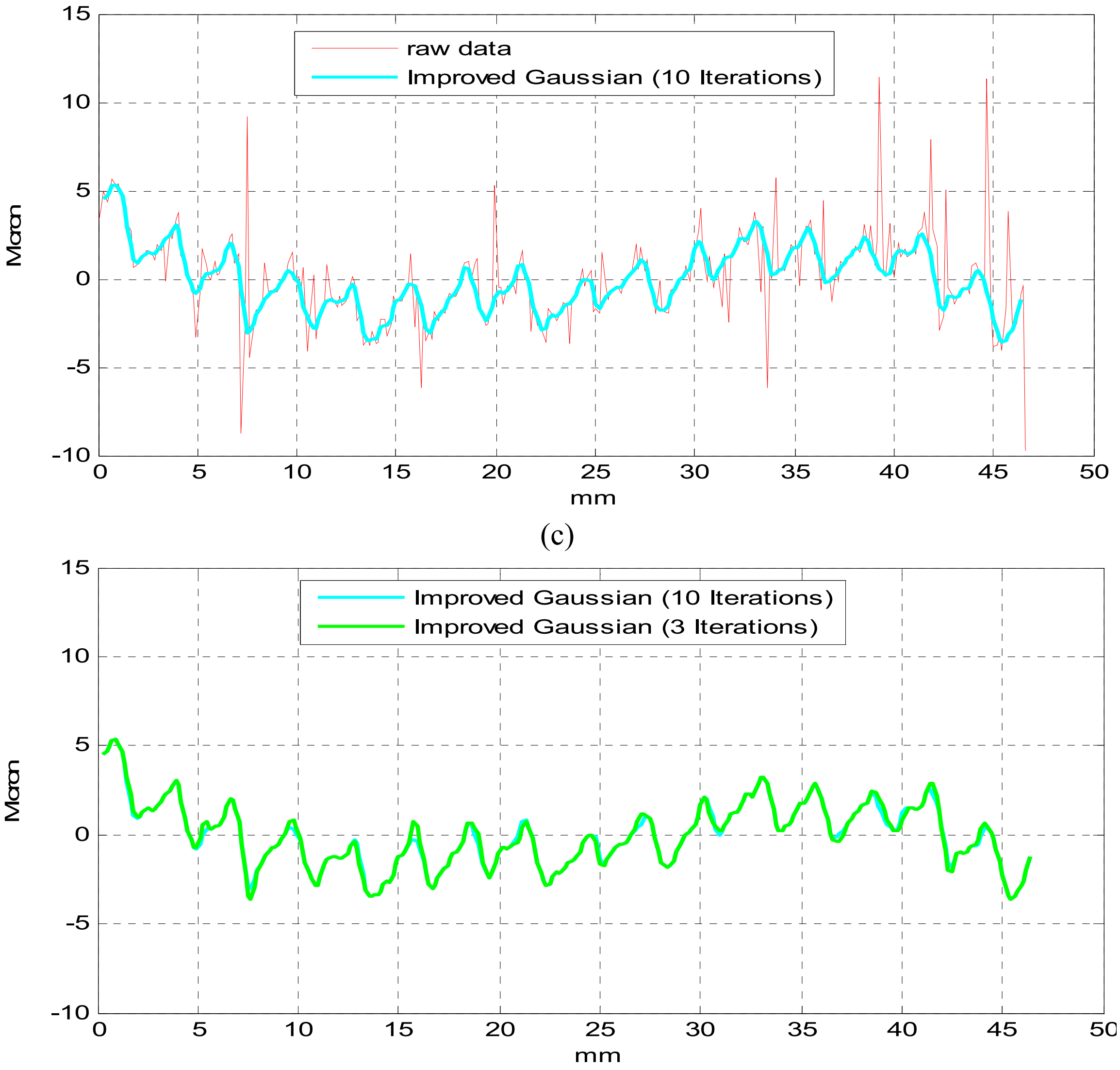

(c)

(d)

Figure 2.13 Compared the waviness extraction results of standard Gaussian filter and improved Gaussian filter.

2.3 Case Study: Severe Tool Wear Detection using 3D Surface Features

In order to show that surface waviness feature provides important information for detecting issues in the machining process, a correlation case study between surface waviness feature and tool flank wear is performed in this section. Flank wear occurs on the tool flank as a result of abrasion between the machined surface of the workpiece and the tool flank. The metric used to evaluate tool flank wear is VB, the flank wear width, as shown in Figure 2.14. When tool gradually loses its edge, the cutting force increases significantly with flank wear, and the extra stress involved is then starting to set up machine vibrations, creating a periodic variation of tool cutting depth, therefore reducing the quality of the surface finish and causing some problems to the workpiece functions, e.g., causing serious coolant, oil, or combustion gas leakages of some nominally flat mating surfaces in the automotive industry. In addition, flank wear in the corner actually shortens the cutting tool thus may introduce dimensional error in machining. Eventually, if the amount of flank wear exceeds some critical value, the excessive cutting force may cause tool failure.

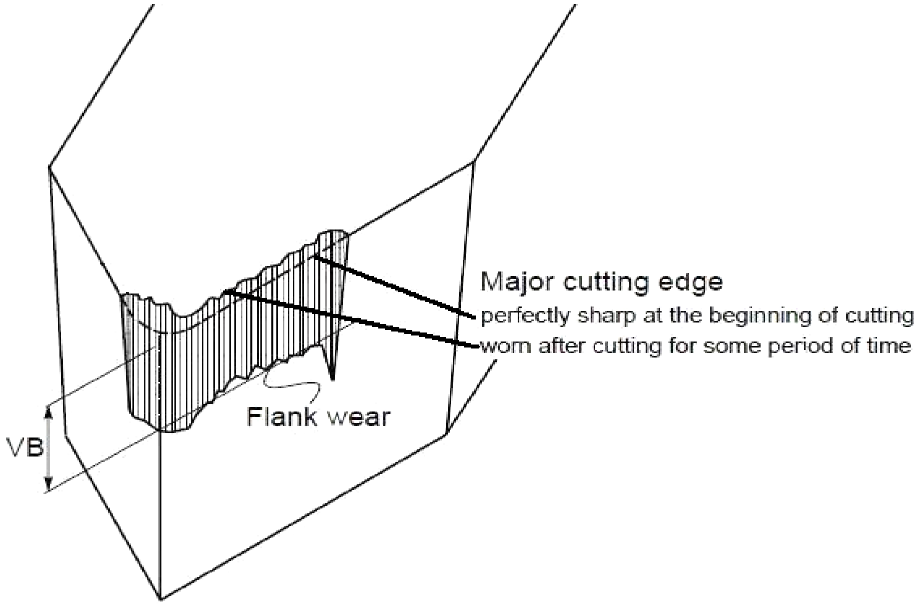

Figure 2.14 Flank wear observed in cutting tools.

2.3.1 Feature I: 3D Surface Waviness Parameter

In the correlation study, a 3D surface waviness feature S_{wa}, which is the average of the absolute value of waviness profile heights over the sample area, is defined and correlated to tool flank wear. The formula of S_{wa} is:

$$S_{wa} = \frac{1}{MN} \sum_{i=1}^{\mathrm{M}} \sum_{j=1}^{N} \left| w(x_i, y_i) \right| \tag{2.6}$$

Where $w(x_i, y_i)$ is the waviness surface extracted from the 3D surface height map, and *MN* means the total number of points on the surface. The reason for choosing this parameter is that, it can represent the amplitude information for the 3D waviness and compared to the extreme parameter (peak-to-valley parameter), it is not that sensitive to the noise.

2.3.1.1 Experimental Results for Aluminum Workpieces

In the first experiment, a polycrystalline diamond (PCD) insert was used to mill samples made by 308 aluminum, which is a hypoeutectic aluminum-silicon alloy widely used for die cast automotive powertrain components. A sample part is shown in Figure 2.15 (a), the 3D surface height map of this part is shown in Figure 2.15 (b). Nine sample parts were machined for this correlation study by single tooth face milling at a spindle speed of 2000 rpm and a feed rate of 0.1 mm/rev (typical cutting parameters in the automotive industry for 308 Aluminum). The cutter lead, axial rake, and radial rake angles were all five degrees. The surface samples were generated by cutting two 80mm × 60mm paths on the top surface in opposite directions, without overlap between the two. Between samples, iron blocks were machined to accelerate wear.

Flank wear VB of the tool used to machine the nine sample parts is listed in Table 2.4. The microscopic images of a new tool and worn tool with flank wear VB are shown in Figure 2.16. In our experiment, tool wear VB was measured manually by selecting the maximum wear distance based on a microscope image of tool's major cutting edge. Based on our experiences, the maximum flank wear a PCD insert can achieve (before breakage) is about 180 micron, and if the flank wear of an insert is larger than 150 micron, it enters the severe wear phase; if the flank wear of an insert is less than 30 micron, it is still in its break-in phase; otherwise, the insert is in its steady wear phase.

Table 2.4: Tool flank wear of nine sample workpieces.

Workpiece #	**Tool Flank Wear VB (μm)**	**Tool Wear Phase**
1	0	Break-in Wear
2	15	Break-in Wear
3	25	Break-in Wear
4	40	Steady Wear
5	60	Steady Wear
6	90	Steady Wear
7	130	Steady Wear
8	160	Severe Wear
9	180	Severe Wear

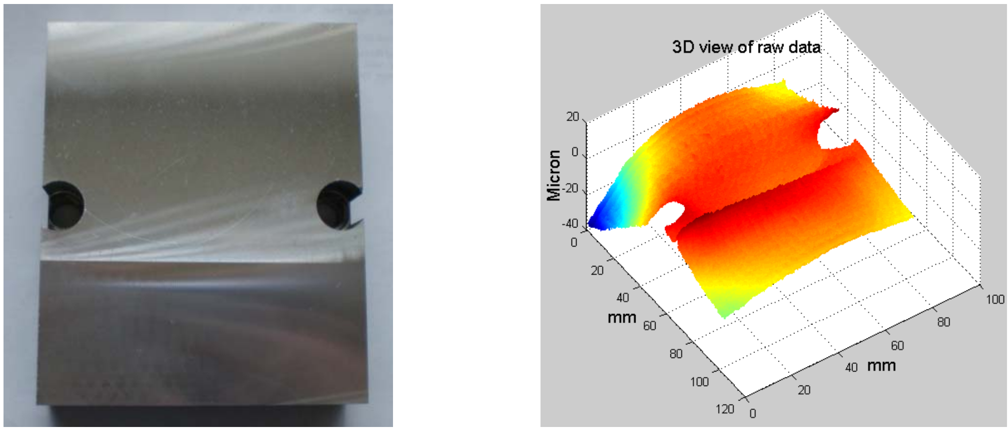

(a) (b)

Figure 2.15 Photo of aluminum parts used in experiment 1.

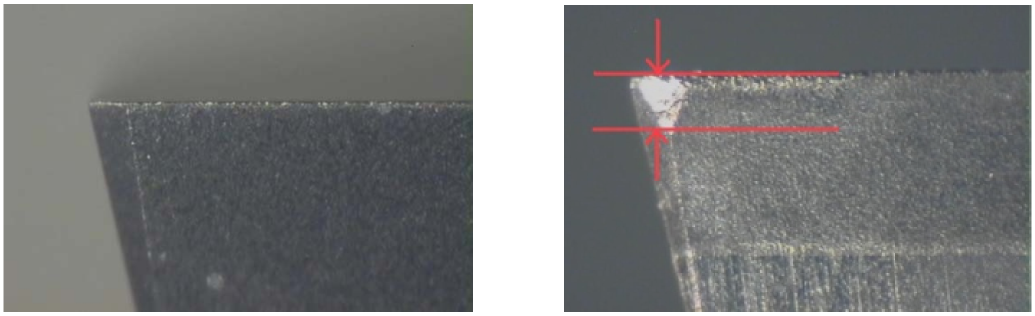

(a) (b)

Figure 2.16 Microscopic images of PCD tool: (a) new PCD tool, (b) PCD tool with flank wear.

Figure 2.17 shows the 3D surface waviness parameter S_{wa} of the nine machined workpieces versus the tool flank wear VB. It can be seen clearly that when the tool enters its severe wear phase, S_{wa} value increases rapidly. That is a result of significant tool vibration when tool is severely worn. Since tool vibration will also increase the tool wear rate [74], they are interacting. Therefore, it can be concluded that the onset of severe tool wear can be detected using 3D surface waviness parameter S_{wa}.

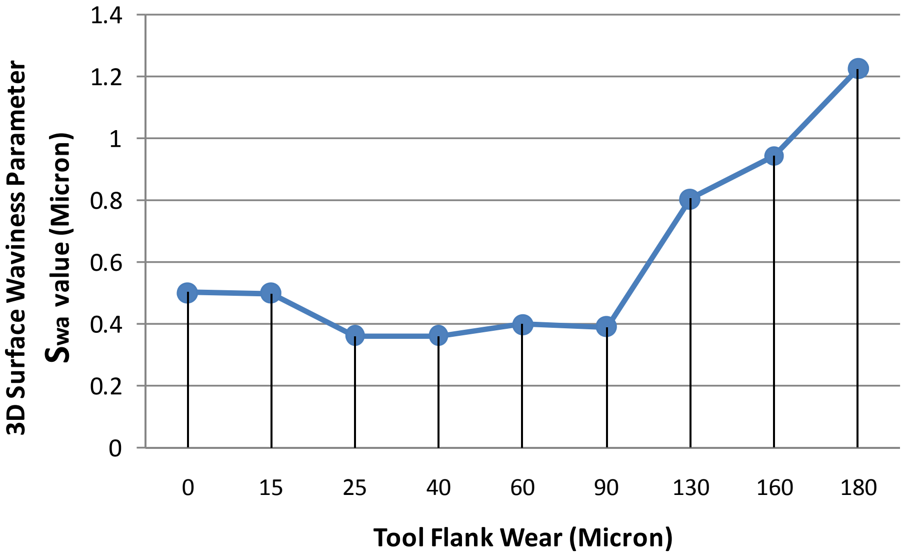

Figure 2.17 3D surface waviness parameter S_{wa} values for nine Al308 sample parts versus tool flank wear VB.

2.3.1.2 Experimental Results for Compacted Graphite Iron Workpieces

More experiments were preformed to check the correlation between 3D surface waviness parameter S_{wa} value and tool flank wear VB. In these experiments, a multiphase coated tungsten carbide insert was used to machine compacted graphite iron (CGI) samples, a material commonly used for diesel engines. Two different cutting conditions were selected, as shown in Table 2.5.

Table 2.5: Selected cutting parameters for CGI workpieces.

	Workpiece Material	Tool Insert Type	spindle speed	feed rate	Maximum VB	Total machined workpieces
Experiment 2	CGI	Multiphase Coated Tungsten Carbide	700 rpm	35mm/ min	290µm	9
Experiment 3	CGI	Multiphase Coated Tungsten Carbide	470 rpm	140m m/min	316µm	19

Figure 2.18 shows the microscopic images of new carbide insert and the insert with some flank wear respectively. Figure 2.19 shows tool flank wear of nine samples used in experiment 2 described in Table 2.5.

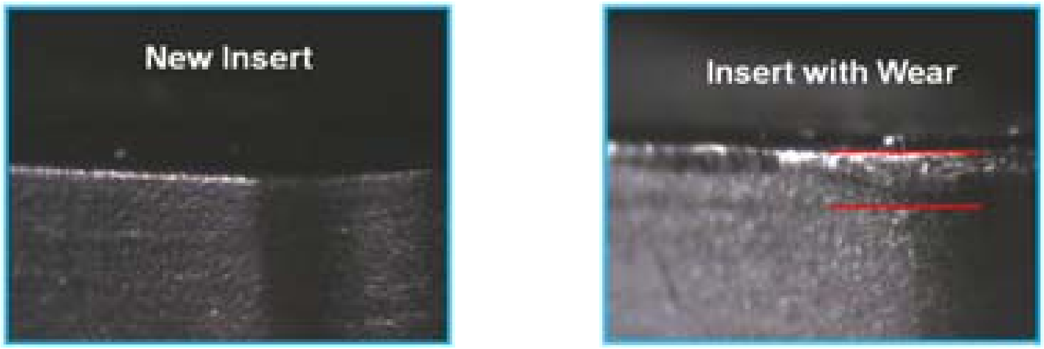

(a) (b)

Figure 2.18 Microscopic images of carbide insert: (a) new carbide insert, (b) carbide insert with flank wear.

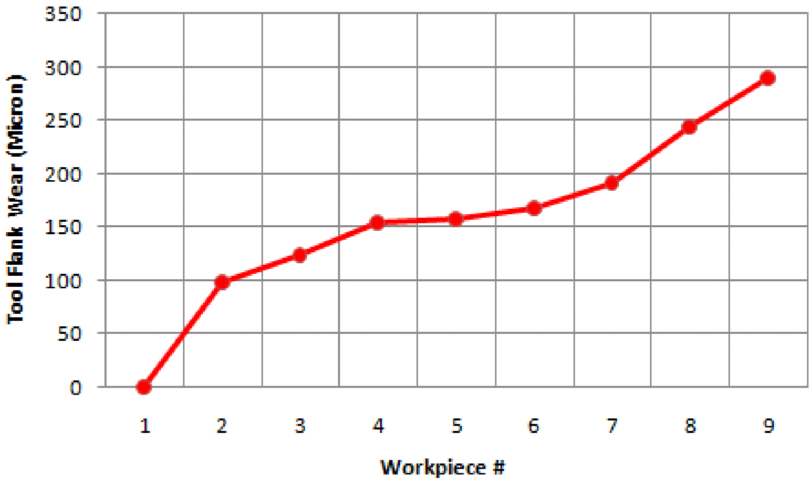

Figure 2.19 Tool flank wear of nine sample workpieces in experiment 1.

Figure 2.20 shows 3D surface waviness parameter S_{wa} versus tool flank wear VB in experiment 2 We can see that when the tool enters its severe wear phase, S_{wa} increases rapidly, the trend is similar to that observed from the PCD insert machining aluminum parts in Figure 2.17.

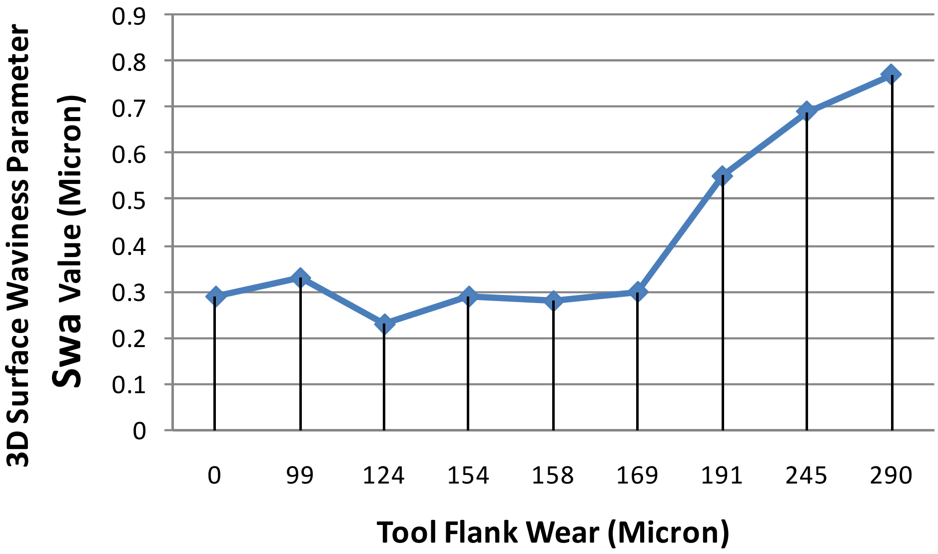

Figure 2.20 3D surface waviness parameter S_{wa} values for nine CGI sample parts versus tool flank wear VB in experiment 1.

In experiment 3, the feed rate was increased and the spindle speed was reduced, which make the tool wear more slowly thus more workpieces can be machined until the maximum tool wear. Figure 2.21 shows the 3D surface waviness parameter S_{wa} versus the tool flank wear VB in experiment 3. It can be seen clearly the result that when tool enters its severe wear phase, S_{wa} increases rapidly, which agrees with the results of experiment 2 as well as the results of experiment 1 (using PCD insert machining the aluminum workpieces).

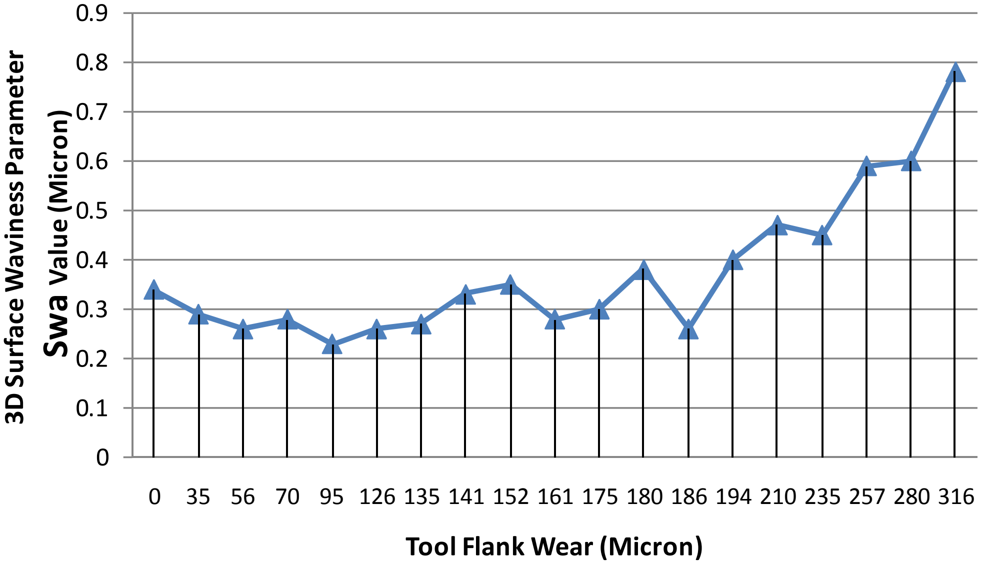

Figure 2.21 3D surface waviness parameter S_{wa} values for nineteen CGI sample parts versus tool flank wear VB in experiment 2.

In summary, in the experiments of both using PCD insert on aluminum workpieces and using carbide insert on CGI parts, when the tool started to wear, the 3D surface waviness parameter S_{wa} first decreased and then stayed steady, and when the tool entered its severely wear phase, the S_{wa} value increased rapidly. Reducing spindle speed and increasing feed rate wear the tool more slowly, but this change will not affect the changing trend of S_{wa} values. In the future implementation on a real production line, a suitable threshold can be set according to the cutter types, workpiece materials, cutting parameters and the requirements of surface finish.

2.3.2 Feature II: Image Intensity Distribution Parameter

Besides 3D surface waviness feature, there are also some other 3D surface features which can be used to correlate to tool flank wear conditions. In this section, we studied another 3D surface feature called image intensity distribution parameter. It is generated from the gray image of the machined workpiece surface captured by a monochrome camera with a pixel size of 7.4× 7.4 μm^2. The illumination system consists of 24 LEDs specially designed to produce uniform illumination and wide angular distribution of the incident light so that small features on the surface can be captured by the camera.

The pixels of the gray image are represented in 256 gray levels (0~255).The gray levels are equally divided into 51 non-overlapping categories: [0, 5, 10, … , 255]. The number of pixels at category i is denoted by n_i and the total number of pixels $N = n_1 + n_2 + \ldots + n_{51}$. Then the gray-level intensity histogram is normalized and regarded as a probability distribution:

$$p_i = n_i / N, \qquad p_i \geq 0, \sum_{i=1}^{51} p_i = 1 \tag{2.7}$$

According to equation 2.7, a histogram chart showing gray-level intensity probability distribution can be generated. The histogram charts of part #2 surface (machined by the tool in the break-in wear phase), part #5 (machined by the tool in the steady wear phase) and part #9 surface (machined by the tool in the severe wear phase) are shown in Figure 2.22.

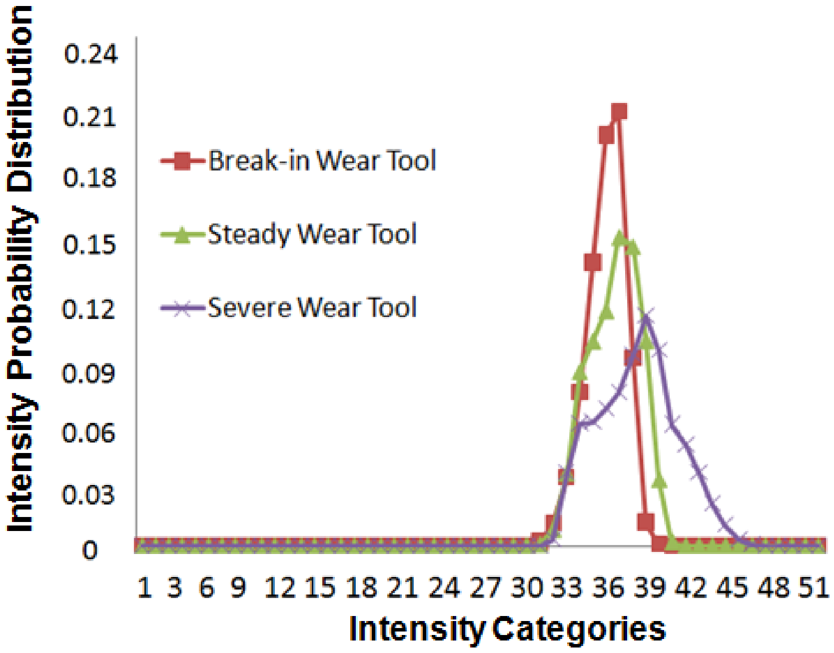

Figure 2.22 Image intensity histograms of part#2 (machined by break-in wear tool), part# 5 (machined by steady wear tool) and part#9 (machined by severe wear tool).

It should be noticed that the intensity level of an image is highly dependent on the reflectance, color and specularity of the surface, thus the intensity itself of a surface is not a good indicator for tool condition. However, as the tool wears and its edge becomes rounded, both the peaks and valleys of the machined surface become flattened and deformed. Also, small chips may adhere to the part surface and make the surface exhibit more irregularities in the reflection pattern compared to a part surface produced by the new tool. As a consequence, when tool wear increases, the gray-level intensity probability distribution of the workpiece surface has a lower peak and spreads broader as shown in Figure 2.22. Therefore, the total number of non-zero probability categories could perform as a good indicator for tool wear detection.

Figure 2.23 shows the total number of non-zero probability categories of the sample parts machined by the PCD insert with different flank wear. As can be seen, when tool enters severe wear phases, the total number of non-zero probability categories increases rapidly.

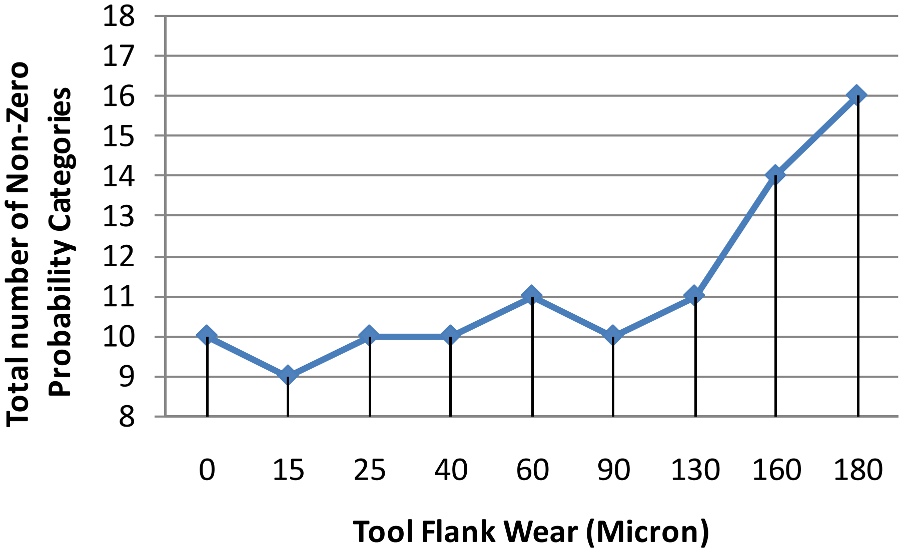

Figure 2.23 Total number of non-zero probability categories of intensity histogram versus tool flank wear.

2.3.3 Feature III: 3D Peak-to-Valley Height

Another 3D surface feature which varies with tool wear is 3D peak-to-valley height. As the cutting edge becomes more rounded and the flank wear becomes larger, there will be increased plowing on the workpiece surface which flattens surface peaks and valleys, hence reduces the surface peak to valley height.

An extreme parameter: height difference between the highest peak and the lowest valley within the surface sample area is too sensitive to the noise. Instead of using that, a statistical extreme parameter is calculated as the average value of the absolute height of the five highest peaks and the absolute depth of the five deepest valleys within the sample area, as shown in the following formula:

$$S_z = \frac{1}{5}\left(\sum_{i=1}^{5} \left|\eta_{pi}\right| + \sum_{i=1}^{5} \left|\eta_{vi}\right| \right) \tag{2.8}$$

Where $\eta(x_i, y_i) = z(x_i, y_i) - f(x_i, y_i)$ is the residual surface, which is the difference between the original surface $z(x_i, y_i)$ and the reference datum $f(x_i, y_i)$. The reference datum is a least squares mean plane of the original 3D surface height data. 3D peak-to-valley height parameter is a peak definition dependent parameter, and the value is determined by the numbers of neighboring points involved in the calculation. Thus it is necessary to specify the definition of a peak/valley. In this calculation, a peak/valley is defined based on the nearest eight neighbors, that is to say, for a pixel, first find its immediate eight neighbor pixels, if the height value of this pixel is larger than the height values of all the eight neighbors, this pixel is defined as a peak; if the height value of this pixel is smaller than the height values of all the eight neighbors, this pixel is defined as a valley. After finding all the peaks and valleys on the sampled surface area, the top five highest peaks and top five deepest valleys are selected for calculating S_z in equation 2.8.

Figure 2.24 (a) and (b) show 3D height maps of the surface machined by the new PCD tool (part #1) and by the worn PCD tool (part# 9) respectively after the data processing. In order to clearly see the difference between these two surface maps, small region with the size of $40mm \times 50mm$ is shown.

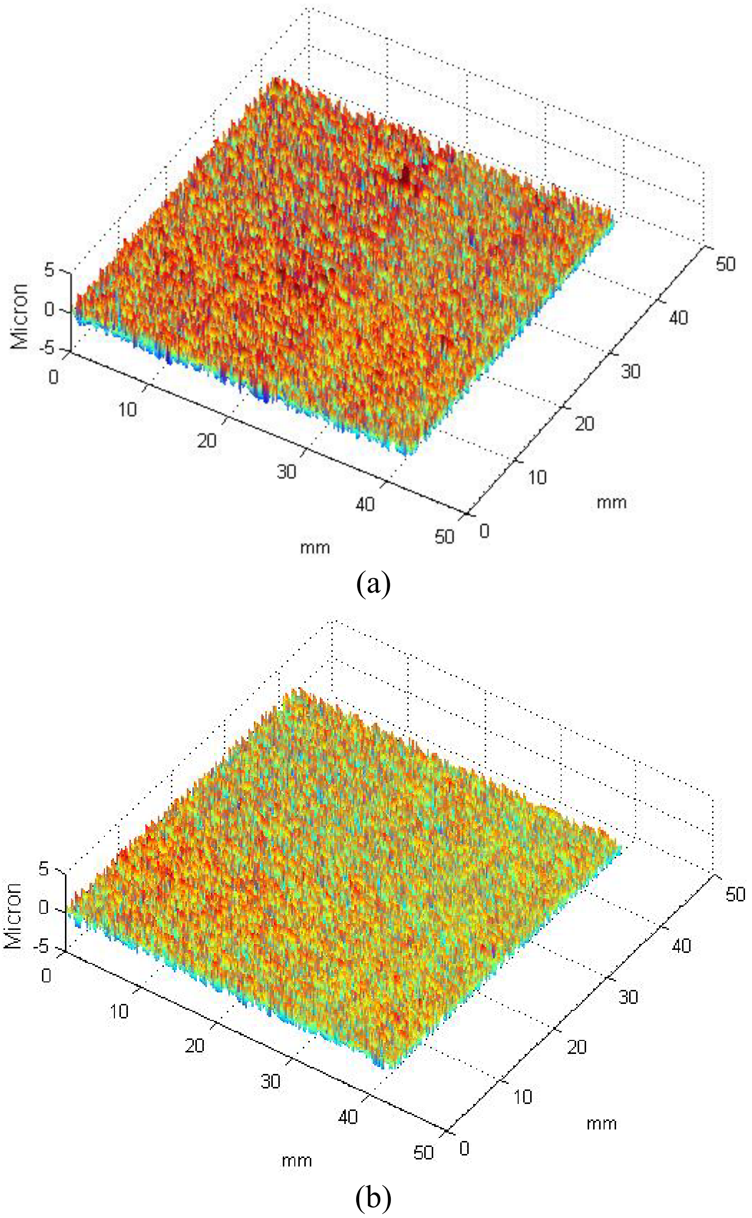

Figure 2.24 (a) 3D height map of the surface machined by new tool (part#1) (b) 3D height map of the surface machined by worn tool (part#9), the region shown has a size of 40mm× 50mm.

Figure 2.25 shows the ten-point peak-to-valley height S_z of the nine sample workpieces calculated using equation 2.8 versus the corresponding tool wear metric VB. The correlation coefficient between the ten-point peak-to-valley height S_z and tool wear metric VB is equal to -0.941. This means that the two variables are highly correlated.

Therefore, the 3D surface parameter S_z can be used as a good indicator to monitor tool wear conditions and determine tool change time. But it is defined based on the extreme peaks and valleys, which might be too sensitive to the peaks/valleys/noise, thus may generate some false alarms.

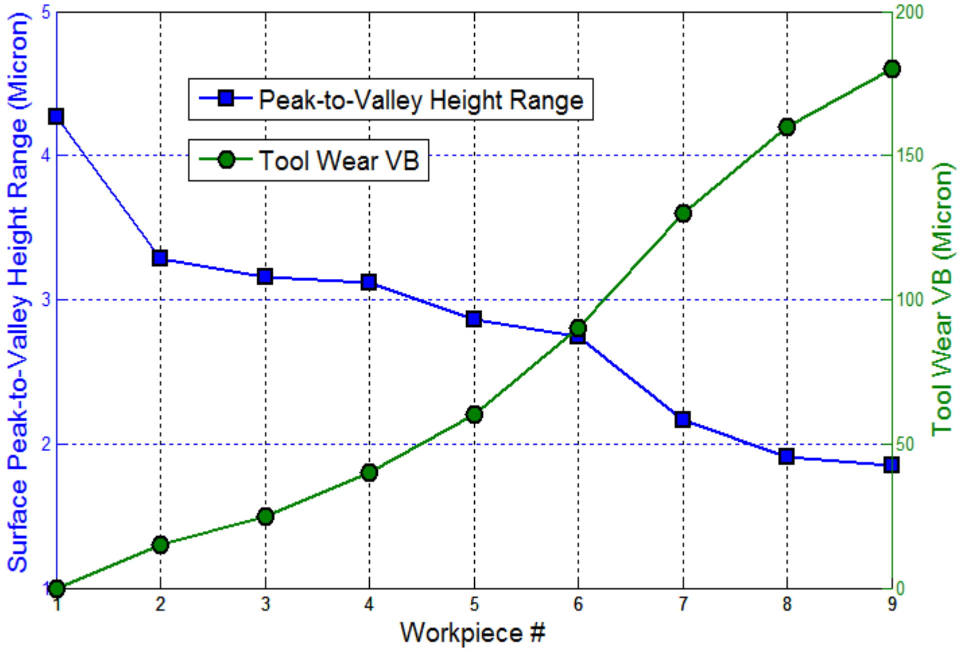

Figure 2.25 Surface ten-point peak-to-valley height versus tool wear VB.

2.4 Conclusions

In this chapter, an improved Gaussian filter was designed to accurately extract 3D surface waviness information from the surface height map measured by the large field of view holographic interferometer. The improved Gaussian filter was specially designed to improve the performance of a standard Gaussian filter when applying on a surface which has large form distortion and lots of sharp peaks/valleys and measurement noises. In this chapter we described each step in the improved Gaussian filter in detail and compared the waviness extraction results using the standard Gaussian filter and the improved Gaussian filter, the results show that the improved Gaussian filter is more robust over the noises and can extract true surface waviness.

In order to show that 3D surface waviness provides important information for detecting errors in the machining process, a correlation case study between surface waviness parameter and tool flank wear is performed. The experimental results show that the 3D surface waviness parameter S_{wa} is a good indicator for detecting severe tool wear in the machining process. Besides surface waviness parameter, two other 3D surface features are also clearly defined and tested, and they can both be used to detect the onset of the severe tool wear.

CHAPTER 3

3D SURFACE DECOMPOSITION AND MULTIPLE-SCALE SURFACE FEATURE EXTRACTION

3.1 Introduction

Besides roughness, waviness and form, a surface can be decomposed into finer frequency bands. Separating a surface into different frequency bands properly has been an important research topic for decades. Raja *et al.* [3] reviewed the recent filter techniques used in the separation of roughness, waviness and form. They studied the advantages and disadvantages of the filter techniques like 2RC [1][22][4][5], Gaussian [22][6][7][8][9], and several newer research methods such as the spline[10][11], morphological[12][13], and wavelet[14][15][16][17][18][19]. In addition to these methods, Fourier transforms [75][76] are also used to decompose surface data into different frequency components. However, during Fourier transforming to the frequency domain, spatial information is lost. The short-time Fourier transform was invented [77][78] to solve this problem, and provides some information about both where and at which frequencies an issue occurs. But the decomposed resolution is determined by the size of the window, which is the same for all frequencies.

Wavelet transform is a mathematical method that can separate a given function into different frequency bands and study each band with a spatial resolution that matches its scale. This special property perfectly meets our need for decomposing a surface into multiple-scale subsurfaces. In wavelet analysis, a signal is decomposed into a series frequency bands using a family of wavelet bases. Large-scale bases represent low frequency components while small-scale bases represent high frequency components. Therefore, wavelet filter is selected as the basic method in this chapter to decompose an engineering surface into multiple-scale subsurfaces, large scale wavelet bases will be chosen for separating low frequency components while small scale bases will be selected for separating high frequency components.

The development of wavelets can be linked to several separate trains of thought, starting with Haar's work in the early 20th century [79]. Notable contributions to wavelet theory include Zweig's discovery of the continuous wavelet transform in 1975 [80] and Daubechies' orthogonal wavelets with compact support in 1988 [81][82].

More recently, many researchers have developed wavelet techniques and applied them to characterize surface functions [19][83][84][85][86][87][88][89][90]. Raja *et al.* [85] compared different wavelet bases from two basic categories: orthogonal and biorthogonal wavelets, and concluded that biorthogonal 6.8 wavelet bases have very good amplitude and linear phase transmission characteristics when applied to engineering surfaces. Stout *et al.* [19] proposed a lifting wavelet representation for extraction of different frequency components of a surface according the intended requirements of functional analysis. Josso *et al*. [86] developed frequency normalized wavelet transform for surface roughness analysis and characterization. Olortegui-Yume *et al.* [88] studied crater wear patterns and their evolution on a series of multi-layer coated tools after machining based on the techniques of multi-scale 1D and 2D wavelets to eliminate noise and to decouple the large/small scale wear features. Li *et al.* [89] proposed an in-line quality inspection method to detect seams, a major type of surface defect in rolling. They used a 1D discrete wavelet transform to extract the features of the images of suspect seams (converted to 1D sequence), and established a T^2 control chart to discriminate between real seams and false positives.

In most of the previous researches, surface has been characterized with 2D parameters based on the data measured by a profilometer or similar methods. However, sometimes the 2D parameters are inadequate or not capable of characterizing all surface attributes of engineering significance [23]. In particular, a set of parameters for characterizing 3D surface texture needs to be developed and applied to diagnose corresponding manufacturing processes. Moreover in recent years, with the invention of optical interferometers, extracting parameters for 3D surfaces has become more feasible. Dong and Stout *et al.* [22][23][24][34][35][36][37] have done some researches on extending the 2D parameters to characterize 3D surface. They also reported in another paper [91] that the wear rate of surfaces in operational service can be determined by roughness, waviness and the multi-scalar topographical features of the surfaces, such as random peak/pits and ridge/valleys. Zeng *et al.* [92] developed a dual-tree complex wavelet transform technique to separate and extract frequency components such as surface roughness, waviness and form. These researches have made significant contributions to 3D surface function characterization.

Nevertheless, it is impossible to have all the data to define accurately the "functionality" of a workpiece surface to predict how it will perform. Most of the previous works were focused on tribological properties for the rotational or moving components [22][24][34][35][36][37][38][39][40][41][42][91][92]. And these works were more focused on the 3D small scale surface features from roughness domain. There is little work done on extracting 3D surface features from middle frequency domain (waviness domain) and utilizing these features to characterize surface functional performance such as sealing property, or to defect machining errors, such as tool wear, tool breakage.

In this chapter, we focus on extracting surface features from large machined surface (e.g., 300mm×300mm). The method of applying 2D wavelets to decompose 3D surface height map into multi-scale subsurfaces is first developed and demonstrated on actual machined part. When applying 2D wavelets to decompose a large 3D surface, a two-channel filter bank diagram is proposed to enable the separate filtering of successive profile in one direction, followed by the same operation in the other, thus greatly simplifies the implementation and brings computational efficiency and conceptual simplicity. We also discuss two issues in the 3D surface wavelet decomposition process: (1) border distortion elimination and (2) the linkage between wavelet scale and its physical dimension. These issues are important when using 2D wavelets to decompose an engineering surface.

Because it is impossible for the surface feature parameters to characterize all the surface functional aspects, the parameters discussed in this chapter are focused on some significant functional property of a flat mating surface, e.g., sealing property. Also some amplitude and energy parameters will be defined and used to detect the machining errors, e.g., abrupt tool breakage. In these case studies, the surfaces of actual automotive parts are decomposed into multiple-scale subsurfaces, and selected 3D feature parameters are extracted from different subsurfaces and applied to predict surface functions and detect errors in the machining process.

The rest of this chapter is organized as follows: Section 3.2 first presents the method of applying wavelets to decompose 3D surface height map into multi-scale subsurfaces. In section 3.3, several case studies are reported, which demonstrate that the 3D multiple-scale surface features extracted using 2D wavelets are good indicators for surface functional performances prediction and machining errors detection. This chapter is summarized in section 3.4.

3.2 Application of Wavelets to Surface Decomposition

3.2.1 One-dimensional Discrete Wavelet Surface Profile Decomposition

Wavelet transform is a mathematical method used to divide a given function into different frequency components and study each component with a resolution that matches its scale. A wavelet is a waveform of effectively limited duration that has an average value of zero. A mother wavelet is a finite energy function (square integrable) $\psi(x)$ with zero mean [80]:

$$\int_{-\infty}^{\infty} |\psi(x)|^2 \, dx < \infty, \quad \int_{-\infty}^{\infty} \psi(x) dx = 0 \tag{3.1}$$

A family of wavelets can be obtained by scaling and translating the mother wavelet with a scale factor *s* and a translation factor *t*:

$$\psi_{t,s}(x) = \frac{1}{\sqrt{s}} \psi\left(\frac{x-t}{s}\right) \tag{3.2}$$

A wavelet transform is defined as the sum over time of the signal multiplied by scaled, shifted versions of the mother wavelet function $\psi(x)$. The Discrete Wavelet

Transform (DWT) is most commonly used in digital signal and image analysis, where the scale factor *s* and translation factor *t* are sampled at discrete steps. Mallat [80] developed an efficient way to sample the scale factor *s* and translation factor *t* based on powers of two (so called dyadic sampling), that is $s = 2^{-k}$ and $t = i \cdot s$, where $i = 1, 2, ..., N$ and N is the number of discrete steps. According to Mallat's method, a family of discrete wavelets can be written as [80]:

$$\psi_{i,k}[n] = 2^{k/2}\psi(2^k n - i), \quad (n = 1, 2, ..., N) \tag{3.3}$$

The one dimensional DWT of a function $f[n]$ can be written as:

$$Wf[i,k] = \sum_{n=1}^{N} f[n]\psi^*[n-i] \tag{3.4}$$

Assuming the scale level is *J*, then the discrete scaling function at scale 2^J is defined as [80]:

$$\phi_{i,J}[n] = 2^{J/2}\phi(2^J n - i), \quad (n = 1, 2, ..., N) \tag{3.5}$$

Actually, a scaling function is a square integrable function (with zero mean), and for all $k \in Z$, $\phi_{i,k}[n]$ is an orthonormal family, and a multiresolution approximation is the vector space generated by this family of functions.

Thus, the low frequency approximation of a function $f[n]$ is:

$$Lf[i,J] = \sum_{n=1}^{N} f[n]\phi_J^*[n-i] \tag{3.6}$$

$f[n]$ can then be decomposed into an approximation and multiple scale details:

$$f[n] = \frac{1}{C_\psi 2^J} Lf[i,J] * \phi_{i,J}[n] + \frac{1}{C_\psi}\sum_{k=0}^{k=J} Wf[i,k] * \psi_{i,k}[n] \tag{3.7}$$

A 1D surface profile data from a cylinder head surface measured by a Taylor Hobson Profilometer and sampled at 4 micron intervals for a length of 40 mm, is used as an example. The linear trend of the profile was first removed by least squares fitting to yield the data shown in Figure 3.1 (a). The Fourier spectrum of this profile is shown in Figure 3.1 (b), and the spectrum shows that there are two dominant frequencies present in the profile, one at 0.025 cycle/mm (long wavelength) and the other at 0.325 cycle/mm (short wavelength). No other structure in the signal is evident.

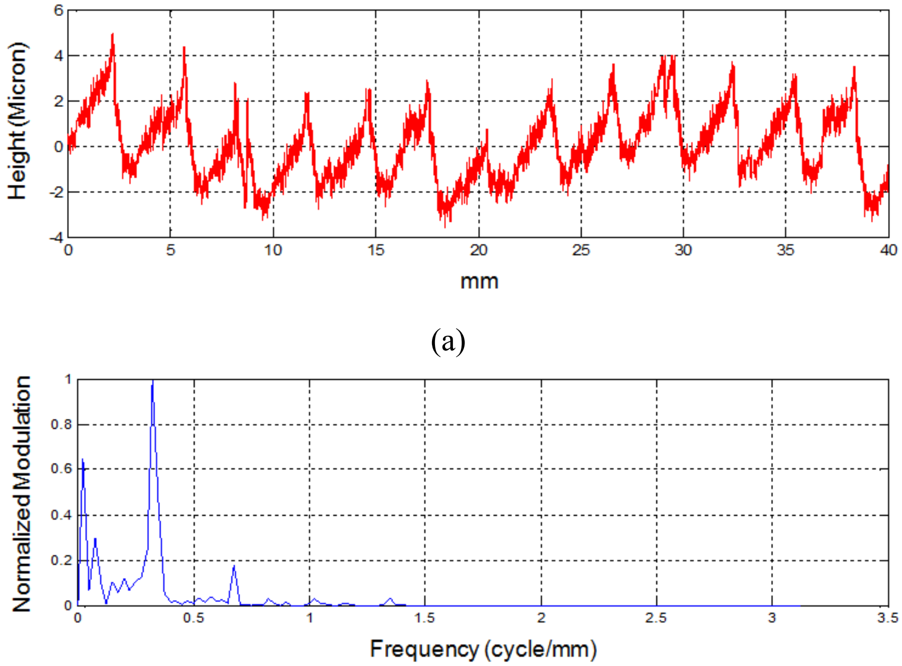

(a)

(b)

Figure 3.1 An example of 1D profile data measured from a cylinder head surface, (b) Fourier spectrum of profile data in (a).

For comparison, multi-scale wavelet decomposition is applied to the same profile data by using the filter bank on the low-pass data profile recursively. Assuming the profile is decomposed into 12 levels, the decomposition logic is shown in equation 3.8, where s is the profile (signal), a_i stands for approximation signal at level i, d_i stands for detail signal at level i.

$$\begin{aligned} s &= a_1 + d_1 \\ &= a_2 + d_2 + d_1 \\ &= a_3 + d_3 + d_2 + d_1 \\ &= \cdots \\ &= a_{12} + d_{12} + d_{11} + d_{10} + d_9 + d_8 + d_7 + d_6 + d_5 + d_4 + d_3 + d_2 + d_1 \end{aligned} \tag{3.8}$$

The multi-scale wavelet decomposition basically consists of two processes: filtering and down-sampling. A diagram for 3-level 1D wavelet decomposition is shown in Figure 3.2. The process is iterative, with successive approximations being filtered by the low-pass filter (LP) and high-pass filter (HP), so that the signal can be broken down into an approximation and multiple details eventually. A down-sampling process is applied to make the data length of the approximation and detail half the length of the previous approximation, thus to keep the total length of the decomposed data the same as that of the original data. This down-sampling does not discard any information if the representation is orthogonal [80].

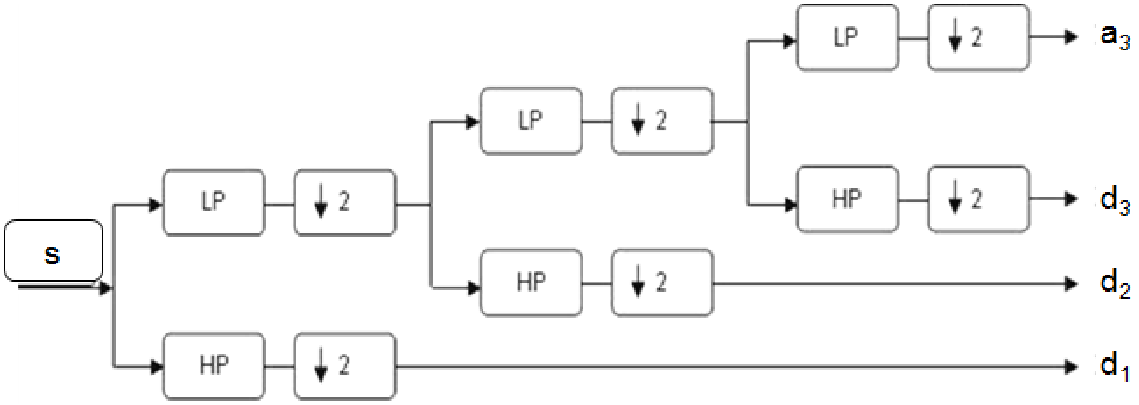

Figure 3.2 Multi-scale filter bank diagram for 1D wavelet decomposition.

Figure 3.3 shows the results of the wavelet decomposition of the profile in Figure 3.1 (a), the results contain one approximation sub-profile and 12 detail sub-profiles. In this study, a biorthogonal 6.8 wavelet is used, since Raja’s precious work on 1D wavelet decomposition showed that biorthogonal 6.8 wavelet has good amplitude and linear phase transmission characteristics for analyzing engineering surfaces [85].

In this example, the surface profile is decomposed into 12 levels. Detail at level 12 (d_{12}) corresponds to the largest scale (lowest frequency) component and detail at level 1 (d_1) corresponds to the smallest scale component. The approximation a_{12} shows some low frequency surface distortion, the detail d_{12} represents the coarse tooling marks, and other small scale features of the surface are well separated. From this example, we can see that Fourier transform analysis treats all frequency components with an equal resolution in both the spatial and frequency domains, but wavelet transform decomposes data into multiple scale (frequency) components and permits study of each component with a resolution that matches its scale, which provides more information to predict surface functional performances or detect errors in the machining process.

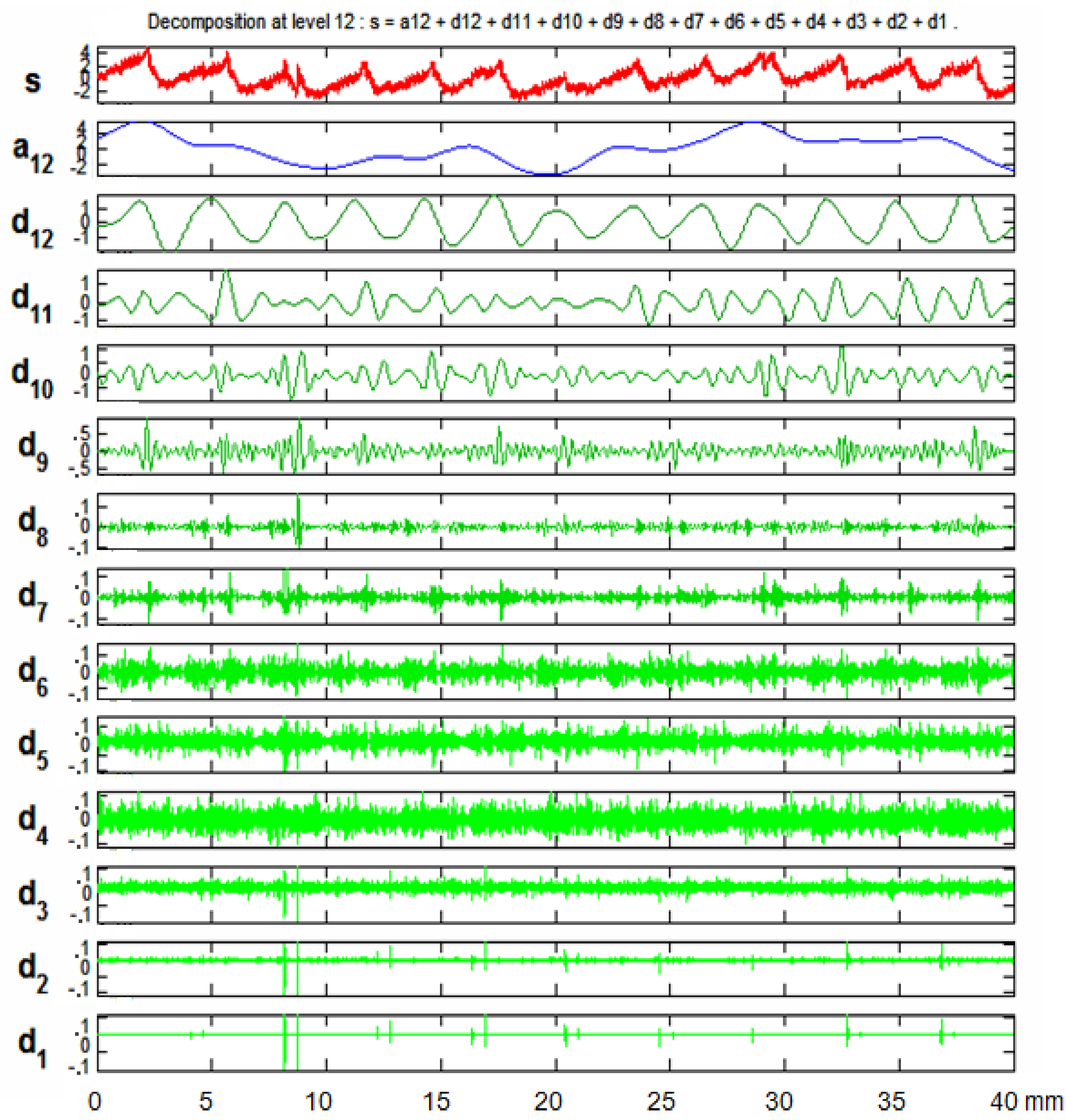

Figure 3.3 1D wavelet decomposition example.

3.2.2 Extend Discrete Wavelet to Decompose Three-dimensional Surfaces

In this section, 1D wavelet function is extended to decompose three-dimensional surface. The extension is quite straightforward, the 2D function can be defined as a tensor product of 1D function. The scaling function is given by:

$$\phi(x, y) = \phi(x)\phi(y) \tag{3.9}$$

The difference between 1D and 2D wavelet is that, instead of one wavelet function, the 2D wavelet has three wavelet functions in the horizontal, vertical and diagonal direction respectively, which can be defined as:

$$\begin{aligned} \psi^H(x,y) &= \phi(x)\psi(y), \\ \psi^V(x,y) &= \psi(x)\phi(y), \\ \psi^D(x,y) &= \psi(x)\psi(y). \end{aligned} \tag{3.10}$$

To implement 2D wavelet on 3D surface decomposition, Figure 3.4 proposes a multi-scale two-channel filter bank algorithm. The basic idea is the same as one dimensional wavelet filter bank shown in Figure 3.2. The difference is that the rows and columns of the surface are filtered and down-sampled perpendicularly (two-channel). This decomposition strategy is especially designed for a surface map with large amount of data points, which can largely reduce the number of arithmetic operations to calculate the convolution sum, thus speed up the whole calculating process.

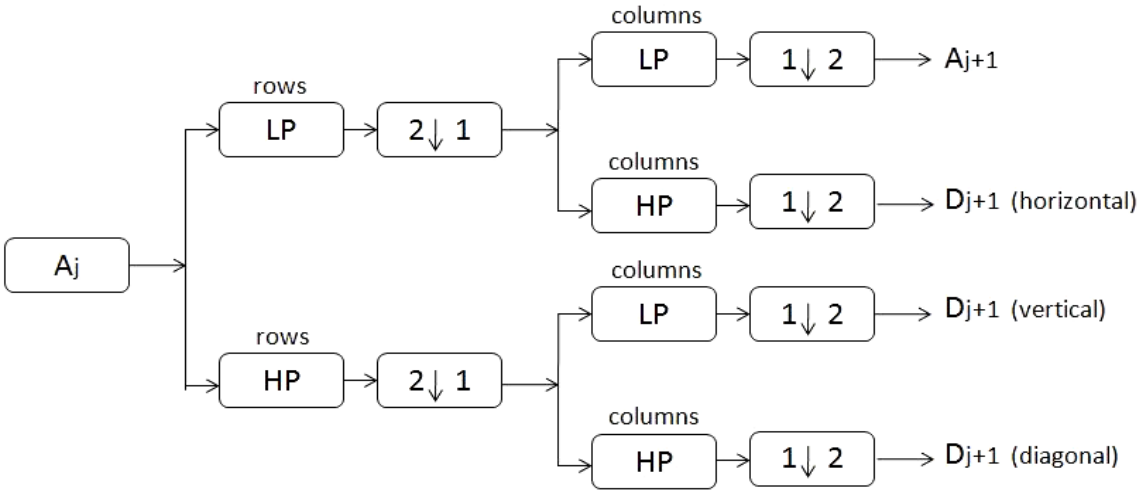

Figure 3.4 Multi-scale two-channel filter bank diagram for 2D wavelet decomposition.

The cylinder head surface shown in Figure 3.5 (a) is an example of applying 2D wavelets on 3D surface decomposition. This surface height map was measured using the holographic interferometer developed by Coherix Inc. [43] as we introduced before. In order to show the details on the surface clearly, only a part of the surface is selected, as shown in Figure 3.5 (b). In this example, the biorthogonal 6.8 wavelet is still used. The original surface is decomposed into approximation subsurface A_1 and 3 detail subsurfaces D_1^V , D_1^H and D_1^{D} in the horizontal, vertical and diagonal directions respectively. Then the approximation subsurface A_1 is decomposed again into the next level approximation and detail subsurfaces. This decomposition process is performed recursively as shown in the decomposition logic in equation 3.11.

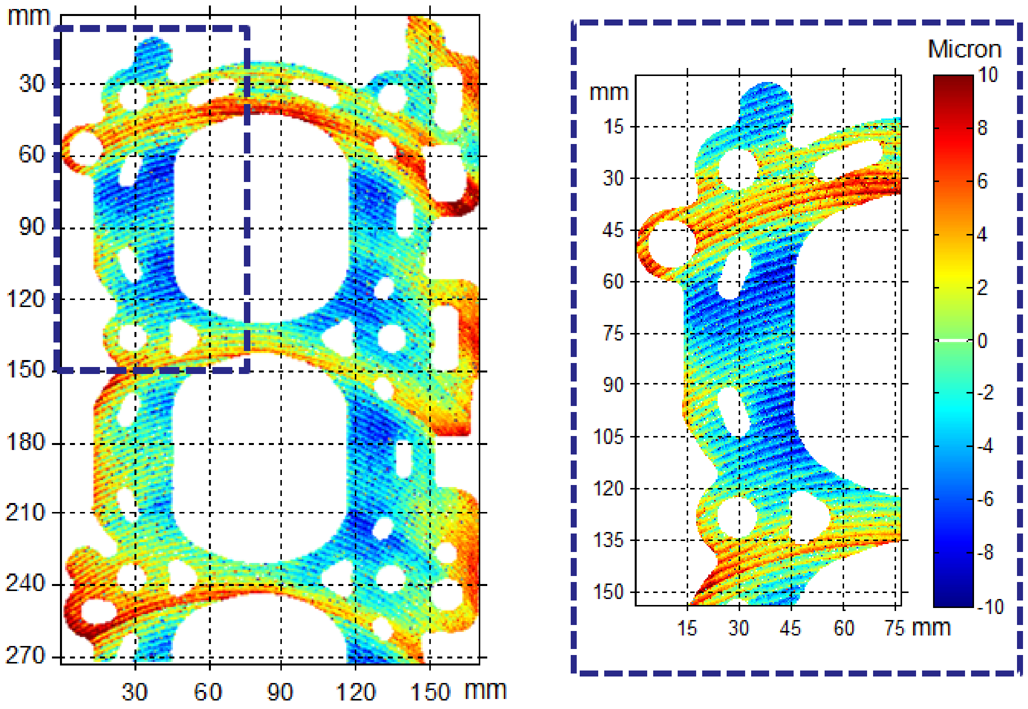

(a) (b)

Figure 3.5 (a) 2D height map of a cylinder head surface, (b) part of the height map in (a) selected as wavelet decomposition example.

$$
\begin{aligned}
S &= A_1 + (D_1^V + D_1^H + D_1^D) \\
&= A_2 + (D_2^V + D_2^H + D_2^D) + (D_1^V + D_1^H + D_1^D) \\
&= \underline{A_3} + \cdots \\
&= \underline{A_4 + (D_4^V + D_4^H + D_4^D)} + (D_3^V + D_3^H + D_3^D) + (D_2^V + D_2^H + D_2^D) + (D_1^V + D_1^H + D_1^D) \\
&= \cdots
\end{aligned}
\tag{3.11}
$$

Figure 3.6 (a) shows the 2D view of the approximation subsurface A_3 and then A_3 is decomposed into the next level approximation subsurface A_4 and detail subsurfaces D_4^H, D_4^V, D_4^D in the horizontal, vertical and diagonal directions. Figure 3.6 (b) shows a 2D view of A_4 and Figure 3.6 (c) shows a summation of the detail subsurfaces $D_4^H + D_4^V + D_4^D$.

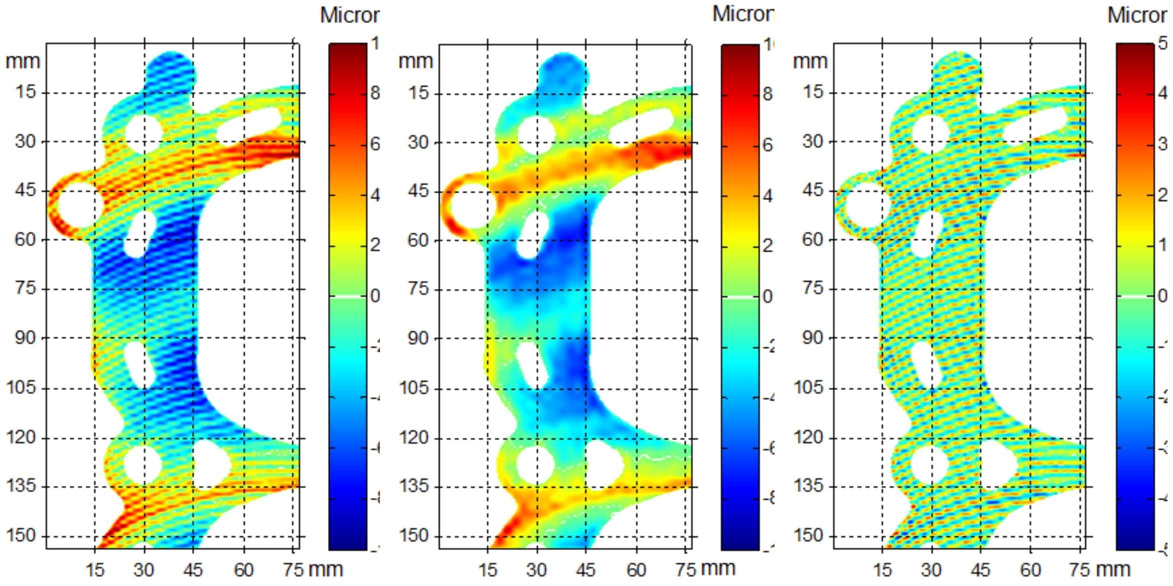

(a) (b) (c)

Figure 3.6 2D wavelet decomposition example: (a) approximation subsurface A_3, (b) approximation subsurface A_4, (c) detail subsurface $D_4^H + D_4^V + D_4^D$.

We can see from the approximation subsurface A_3 that the tooling marks of the machined surface are not separated from the surface form yet, but from the approximation subsurface A_4, it can be seen that the tooling marks (shown in the detail subsurface) of the surface were separated from the surface form (shown in approximation subsurface) completely.

Figure 3.7 shows a 3D view of the decomposition results, we can see more clearly that the tooling marks are totally separated at the decomposition level 4.

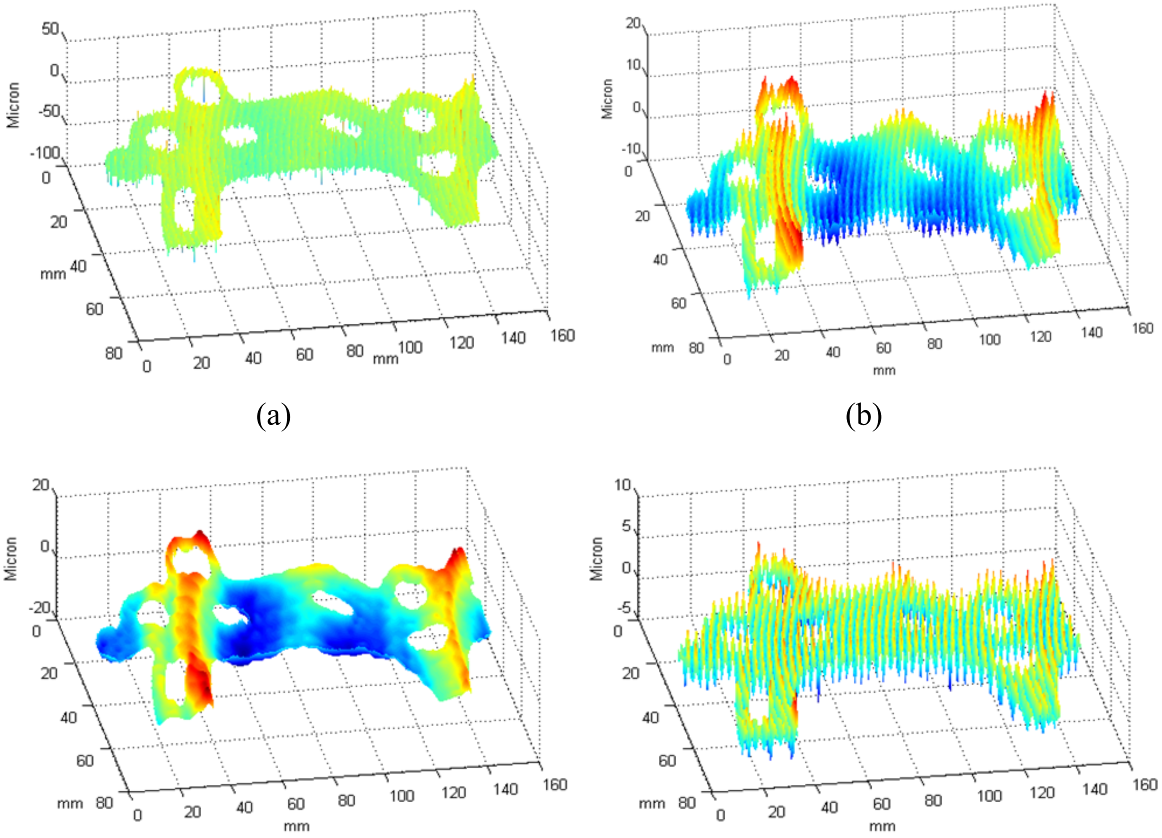

(a) (b)

(c) (d)

Figure 3.7 3D view of 2D wavelet decomposition example: (a) original surface data, (b) approximation subsurface A_3, (c) approximation subsurface A_4, (d) summation of detail subsurfaces $D_4^H + D_4^V + D_4^D$.

3.2.3 Eliminate Border Distortion in 2D Wavelet Decomposition

The algorithm for 2D discrete wavelet decomposition is basically a convolution, and when a convolution is performed on finite-size images, border distortion occurs. The distortion is even worse when the surface is an engineering surface, since the border of an engineering surface is complicated, and it is not a regular shape, such as a rectangular. To eliminate border distortion, extension of borders for the original height map is needed before the decomposition and truncation is necessary after the decomposition.

There are several border extension methods, such as zero padding, symmetrical padding, smooth padding, and periodic padding [93]. In this study, the simplest extension method, zero padding, is applied, because it is impossible to predict the height value outside the border and the height value outside the border will be truncated afterwards. By using zero padding method, it is assumed that the height value of the 3D surface is zero outside the original support.

In the truncation step, a simple method is developed: multiplying the decomposed subsurface with a surface mask. The surface mask is obtained from the original height map, in which pixels with valid height values are assigned a binary value of 1, while pixels without valid height values are assigned a binary value of 0. Figure 3.8 (b) shows a mask for the surface shown in Figure 3.5 (b). Figure 3.8 (a) and (c) show the subsurface before and after border distortion removal. It can be seen from the result that the border distortion effect can be completely eliminated by this simple extension and truncation method.

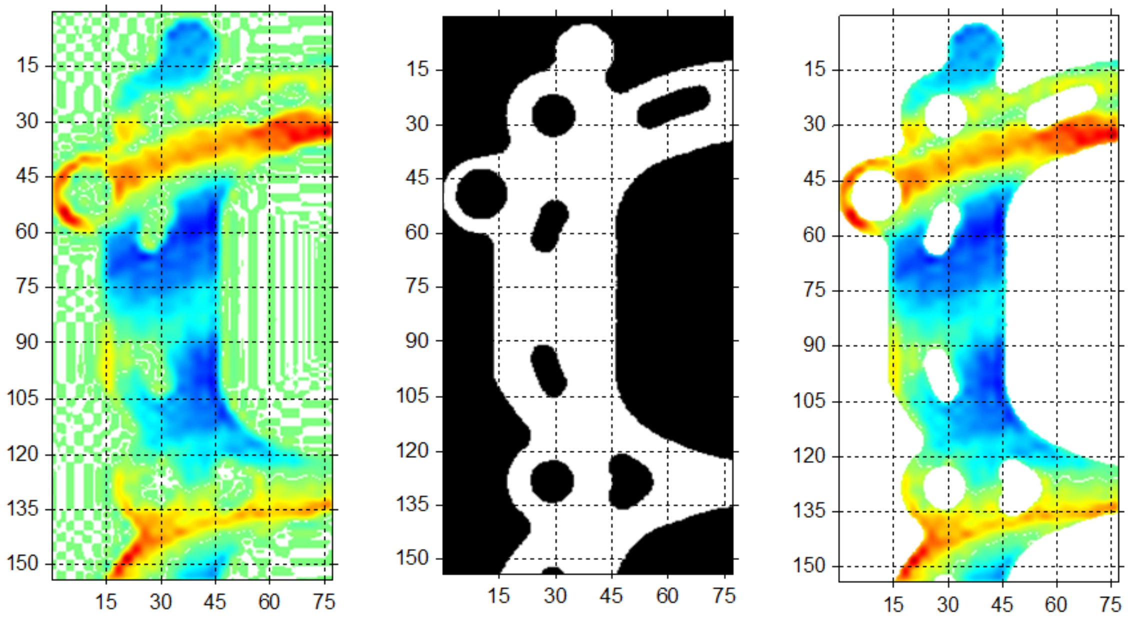

(a) (b) (c)

Figure 3.8 Border distortion elimination: (a) approximation subsurface A_3 before removal of border distortion, (b) surface mask obtained from original surface, (c) approximation subsurface A_3 after removal of border distortion.

3.2.4 Transformation between Wavelet Scale and Physical Dimension

The wavelet analysis is not spatial frequency view of a signal, but scale view of a signal. There is a correspondence between wavelet scales and frequencies as revealed by wavelet analysis:

Small scale s => compressed wavelet => high frequency ω,

Large scale s => stretched wavelet => low frequency ω.

Besides the correspondence, there is a need to quantify this relationship: build a connection between the scale of the wavelet at each decomposition level and the physical dimension (spatial frequency/period). The quantified relationship can play the role of guidance in the applications.

A method of quantifying this relationship using the center frequency F_c of the wavelet is proposed as:

$$\text{Pseudo-frequency: } F_s = \frac{F_c}{s \cdot \Delta}; \quad \text{Physical dimension}: D_s = \frac{1}{F_s} \tag{3.12}$$

Where s is the scale, Δ is the sampling period of the original data, F_c is the center frequency of a wavelet, F_s is the pseudo-frequency corresponding to the scale s and D_s is the physical dimension (pseudo-period) of scale s. The idea is to associate with a given wavelet a purely periodic signal of frequency F_c.

Figure 3.9 shows an example of fitting the center frequency of a wavelet with a periodic signal. The center frequency-based approximation captures the main wavelet oscillations, so the center frequency is a representative characterization of the leading dominant frequency of the wavelet. If we associate the frequency F_c to the wavelet function, then when the wavelet is dilated by a scale factor s, this center frequency becomes F_c / s. Lastly, if the underlying sampling period is Δ, it is natural to associate to the scale s the frequency: $F_s = F_c / s \cdot \Delta$. In our case, the sampling period of the original surface height map Δ=0.15mm.

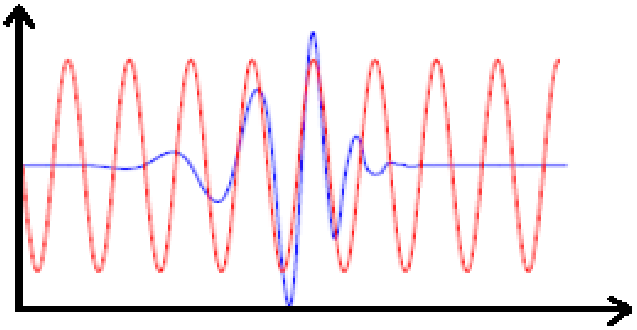

Figure 3.9 Fitting the center frequency of a wavelet with a periodic signal.

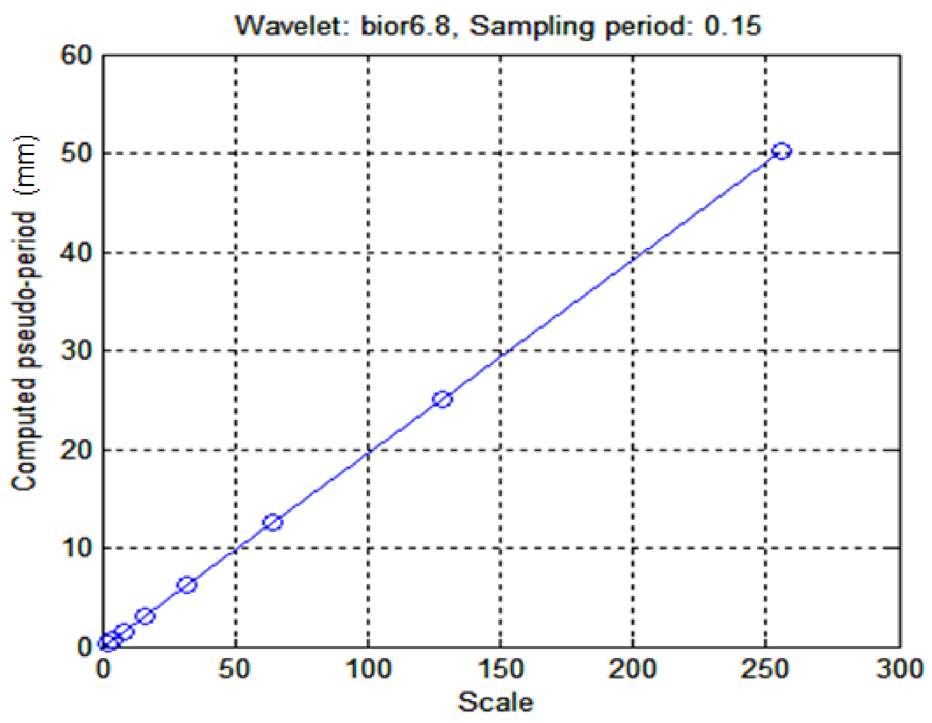

Figure 3.10 Transformation chart between the scale and its physical dimension (pseudo-period).

Table 3.1: Transformation between scale and the physical dimension (pseudo-period)

Level	1	2	3	4	5	6	7	8
Scale	2	4	8	16	32	64	128	256
Pseudo-period (mm)	0.39	0.78	1.57	3.14	6.28	12.55	25.10	50.20

Table 3.1 and Figure 3.10 show the transformation between the scale *s* and the corresponding pseudo-period (mm) of the biorthogonal 6.8 wavelet, assuming the decomposition levels is 8. Consequently, by using equation 3.12, a connection between the scale of the wavelet and the physical dimension at each decomposition level can be built, thus people can have a general sense of the leading dominant frequency of a wavelet.

3.3 Case Studies of Machined Surface Analysis Based on Features Extracted from Multi-scale Subsurfaces

A three-dimensional machined surface can be separated into different frequency bands using wavelet decomposition algorithm developed in the previous sections. By analyzing multiple-scale subsurfaces, we can map appropriate subsurfaces (frequency bands) to the machining process steps which produce the surface and detect errors in the manufacturing process. We can also use the multi-scale subsurface features to predict the functional performance of the surface. In this section, we will show how we extract the important surface features from the multi-scale subsurfaces and use these features from different scales to detect machining conditions, such as abrupt tool breakage, chatter, and also to predict some important surface functions, such as non-clean up of rotating parts and possible leak path of mating/sealing surfaces.

3.3.1 Case Study 1: Abrupt Tool Breakage Detection

In this case study, an example is given to demonstrate the detection of abrupt tool breakage using selected feature parameters extracted from subsurfaces based on wavelet decomposition. In this example, 16 sample V6 cylinder head joint surfaces are studied. One of the parts, part 10, was machined by a tool which broke during the cut. The original surface height maps for part 1, cut without incident, and part 10 are shown in Figure 3.11 (a) and (b). From the original surface, we cannot tell which surface was machined by a broken tool arbitrarily.

2D wavelets are then used to decompose the cylinder head surfaces. Figure 3.11 (c) and (d) show the subsurface $D_4^H + D_4^V + D_4^D$ of part 1 and part 10 respectively (at level 4). From the subsurfaces, the parts which were machined by a good tool or a broken tool can be clearly discriminated.

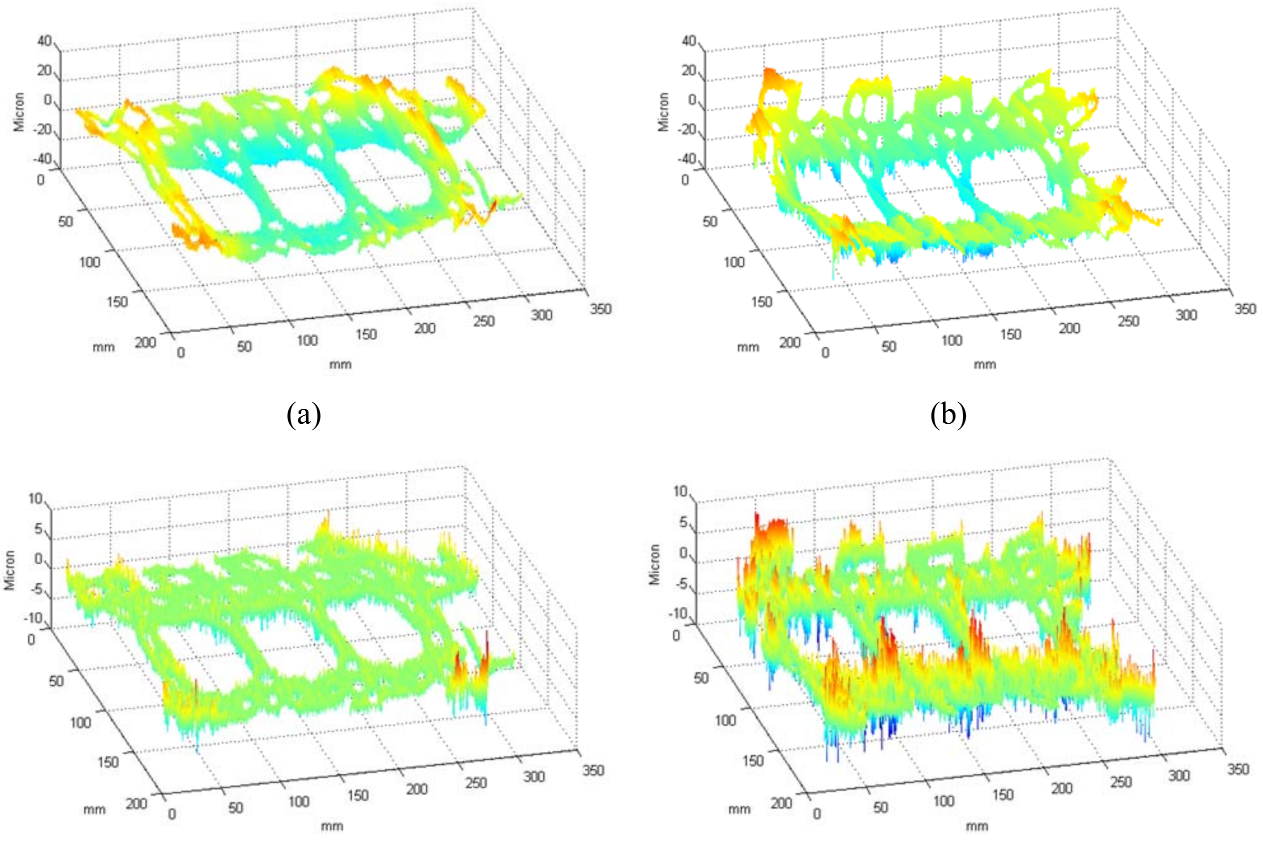

(a)
(b)
(c)
(d)

Figure 3.11 (a) Original surface height map of part 1, (b) original surface height map of part 10, (c) detail subsurface $D_4^H + D_4^V + D_4^D$ of part 1 (at level 4), (d) detail subsurface $D_4^H + D_4^V + D_4^D$ of part 10 (at level 4).

In the following steps, several features (parameters) are defined and extracted to detect tool breakage.

Let $f(x, y)$ be the original surface of size $M \times N$, and $d(x, y)$ be the decomposed detail subsurface of $D_4^H + D_4^V + D_4^D$ at level 4. The first parameter S_t is a statistical extreme parameter, calculated as the average value of the absolute height of the five highest peaks and the absolute depth of the five deepest valleys on the detail subsurface

$D_4^H + D_4^V + D_4^D$, as shown in equation 3.13 below. In this calculation, the peak is defined based on the nearest 5×5 neighbors.

$$S_t = \frac{1}{5}\left(\sum_{i=1}^{5} \left| d_p(x_i, y_i) \right| + \sum_{i=1}^{5} \left| d_v(x_i, y_i) \right| \right) \tag{3.13}$$

The second parameter S_a is a statistical average parameter, which is defined as the average of the absolute value of profile heights over the detail subsurface $D_4^H + D_4^V + D_4^D$:

$$S_a = \frac{1}{MN} \sum_{i=1}^{N} \sum_{j=1}^{N} \left| d(x_i, y_i) \right| \tag{3.14}$$

In this case study, we also use the energy function to identify a texture pattern. At a decomposition level *j*, the wavelet decomposition results in four subsurfaces: one approximation subsurface $f_{LL}^{j}(x, y)$, and three detail subsurfaces $f_{LH}^{j}(x, y)$, $f_{HL}^{j}(x, y)$, $f_{HH}^{j}(x, y)$, which represent the horizontal, vertical and diagonal directional subsurfaces. The energy function of each decomposed subsurface can be calculated as follows:

The energy of the approximation subsurface at level *J*:

$$E_a^J = \sum_x \sum_y [f_{LL}^J(x, y)]^2 \tag{3.15}$$

The energy of the horizontal detail subsurface at level *j*, *j=1,2,…,J.*

$$E_h^j = \sum_x \sum_y [f_{LH}^j(x, y)]^2 \tag{3.16}$$

The energy of the vertical detail subsurface at level *j*, *j=1,2,…,J.*

$$E_v^j = \sum_x \sum_y [f_{HL}^j(x, y)]^2 \tag{3.17}$$

The energy of the diagonal detail subsurface at level j, $j=1,2,\ldots,J$.

$$E_d^j = \sum_x \sum_y [f_{HH}^j(x,y)]^2 \tag{3.18}$$

The total energy of the subsurface at level J is give by:

$$E = E_a^J + \sum_{j=1}^{J} E_h^j + \sum_{j=1}^{J} E_v^j + \sum_{j=1}^{J} E_d^j \tag{3.19}$$

The energy parameters defined and applied in this case study are: $\overline{E_a^4} = \frac{E_a^4}{E}$, the normalized energy of the approximation subsurface at level 4; $\overline{E_h^4} = \frac{E_h^4}{E}$, the normalized energy of the horizontal detail subsurface at level 4; $\overline{E_v^4} = \frac{E_v^4}{E}$, the normalized energy of the vertical detail subsurface at level 4; $\overline{E_d^4} = \frac{E_d^4}{E}$, the normalized energy of the diagonal detail subsurface at level 4; $\overline{E_t^4} = \overline{E_a^4} + \overline{E_h^4} + \overline{E_v^4} + \overline{E_d^4}$, the total normalized energy of the approximation subsurface and detail subsurfaces at level 4.

Figure 3.12 shows the plots of: (a)-(b), S_t and S_a as defined in euqation 3.13 and 3.14; (c)-(g), energy parameters at wavelet decomposition level 4: (c) $\overline{E_t^4}$ total normalized energy, (d) $\overline{E_a^4}$ normalized energy of the approximation subsurface, (e)-(g) $\overline{E_h^4}$, $\overline{E_v^4}$, $\overline{E_d^4}$ normalized energy of the detail subsurfaces in the horizontal, vertical and diagonal directions.

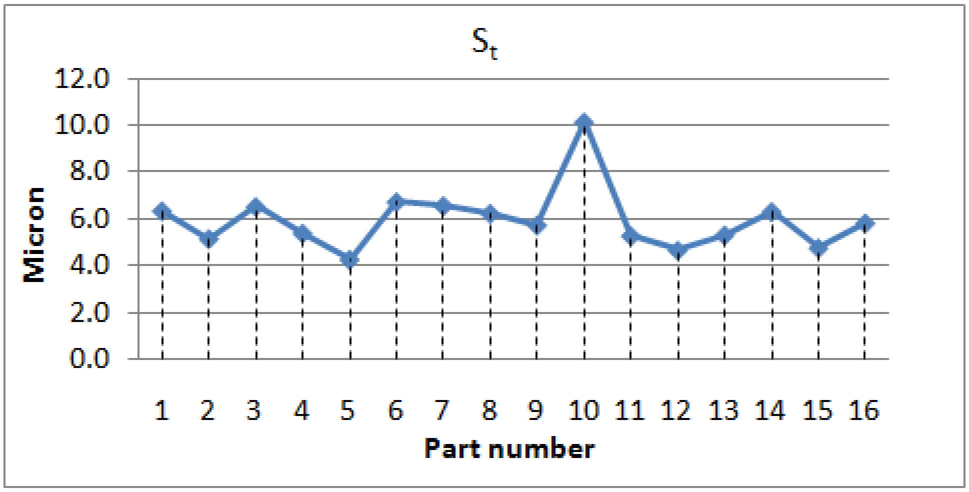
S_t
12.0
10.0
8.0
6.0
4.0
2.0
0.0
Micron
1
2
3
4
5
6
7
8
9
10
11
12
13
14
15
16
Part number

(a)

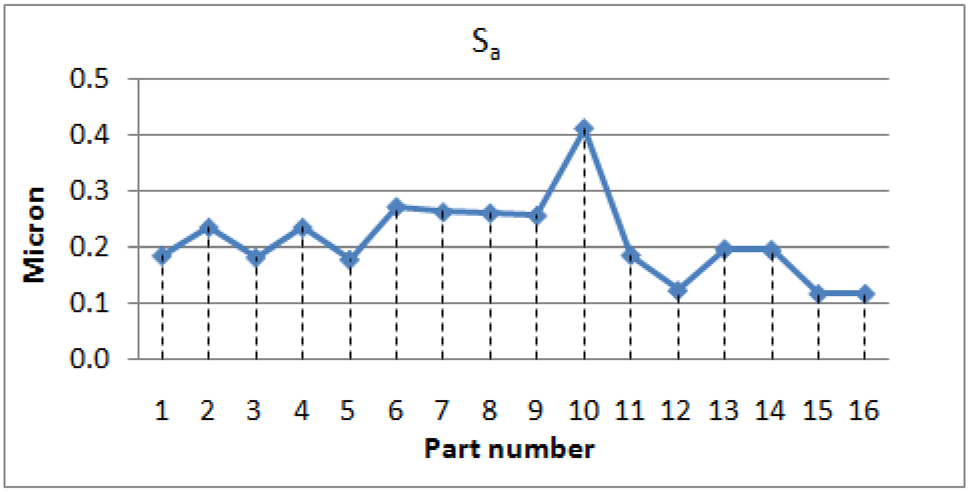
S_a
0.5
0.4
0.3
0.2
0.1
0.0
Micron
1
2
3
4
5
6
7
8
9
10
11
12
13
14
15
16
Part number

(b)

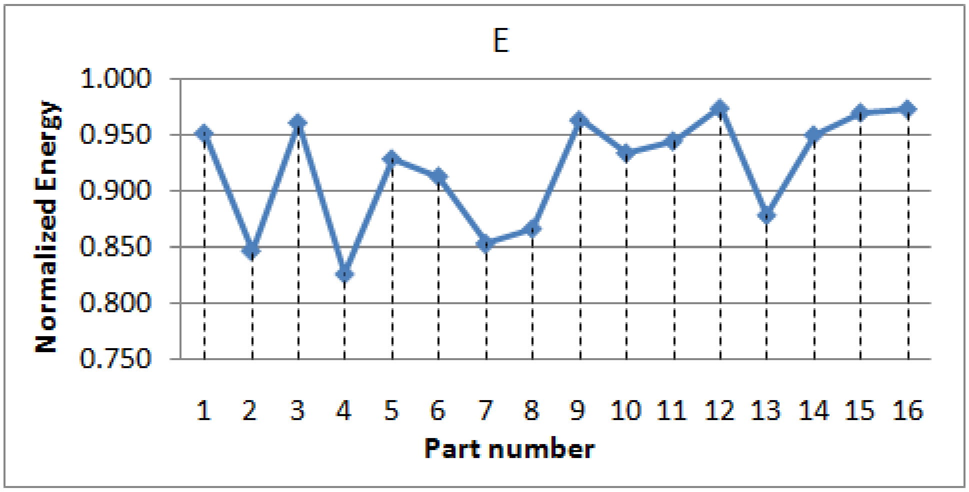
E
1.000
0.950
0.900
0.850
0.800
0.750
Normalized Energy
1
2
3
4
5
6
7
8
9
10
11
12
13
14
15
16
Part number

(c)

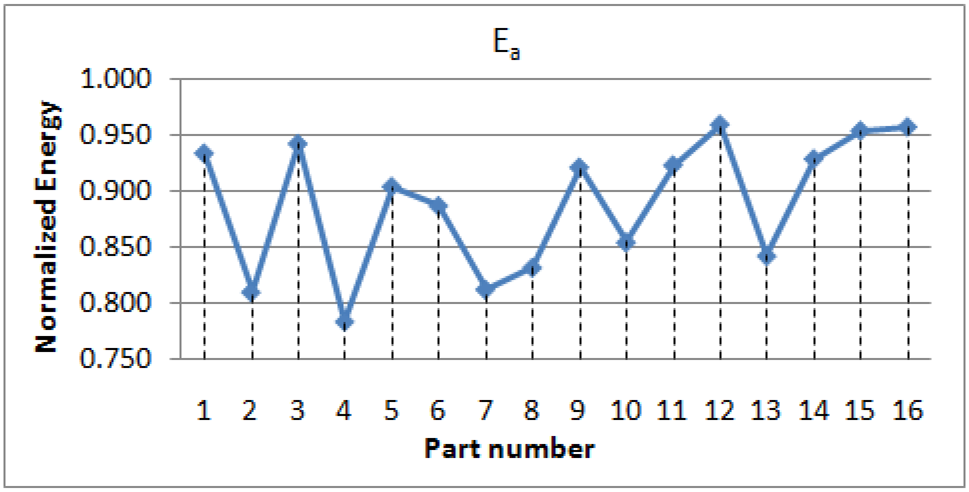
E_a
Normalized Energy
1.000
0.950
0.900
0.850
0.800
0.750
1 2 3 4 5 6 7 8 9 10 11 12 13 14 15 16
Part number

(d)

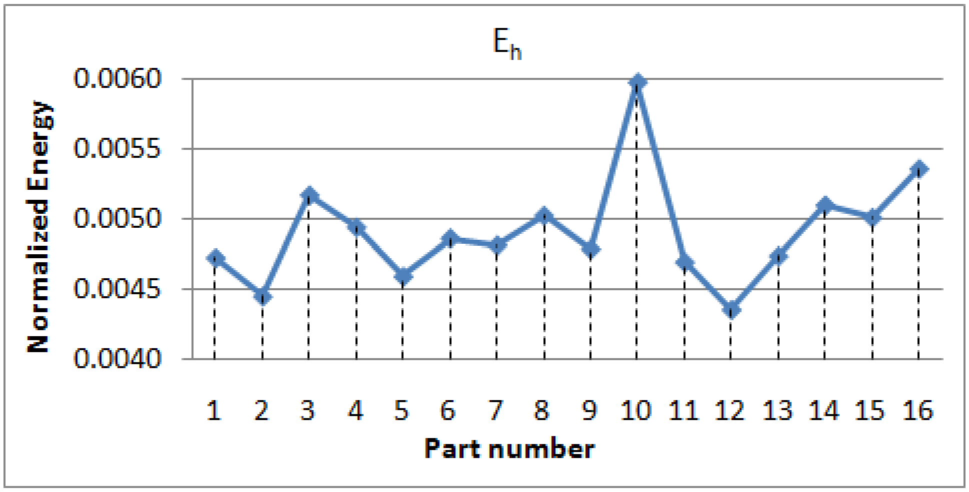
E_h
Normalized Energy
0.0060
0.0055
0.0050
0.0045
0.0040
1 2 3 4 5 6 7 8 9 10 11 12 13 14 15 16
Part number

(e)

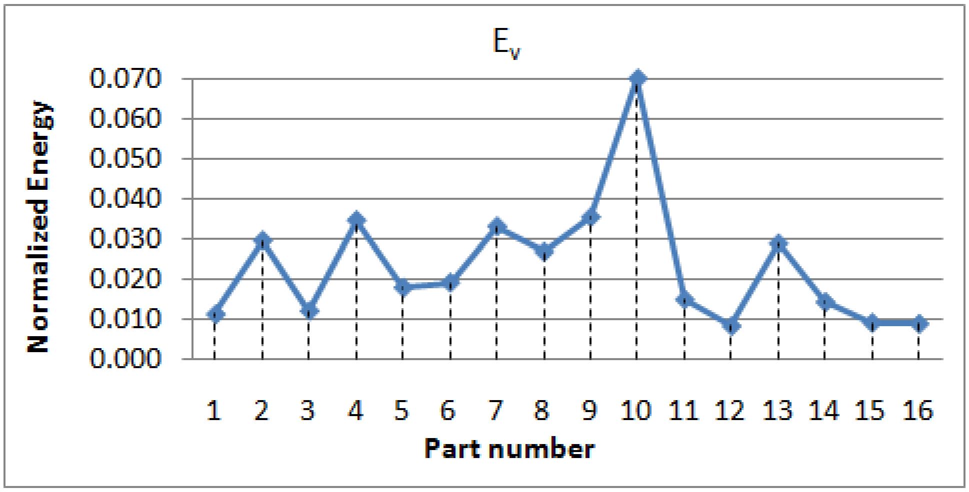
E_v
Normalized Energy
0.070
0.060
0.050
0.040
0.030
0.020
0.010
0.000
1 2 3 4 5 6 7 8 9 10 11 12 13 14 15 16
Part number

(f)

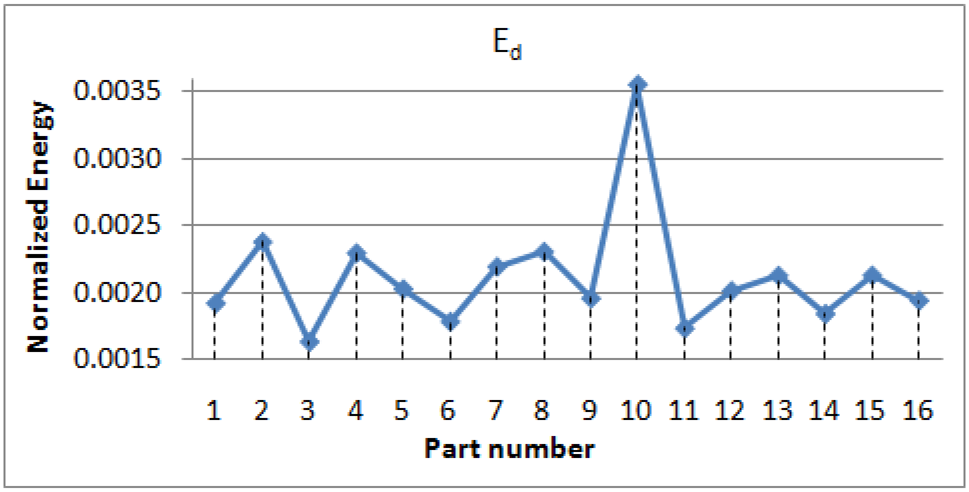

(g)

Figure 3.12 (a)-(b), plots of parameter S_t and S_a as defined in function 3.13 and 3.14, (c)-(g), plots of energy parameters at wavelet decomposition level 4: (c) $\overline{E_t^4}$ total normalized energy, (d) $\overline{E_a^4}$ normalized energy of the approximation subsurface, (e)-(g) $\overline{E_h^4}$, $\overline{E_v^4}$, $\overline{E_d^4}$ normalized energy of the detail subsurfaces in the horizontal, vertical and diagonal directions.

As shown in Figure 3.12(a) and (b), both the S_t and S_a values calculated from the detail subsurface height are good indicators to detect the defective part, part 10. The plots of the energy parameters in Figure 3.12 (c) and (d) indicate that the total normalized energy $\overline{E_t^4}$ and the normalized energy of approximation subsurface $\overline{E_a^4}$ at level 4 are not good indicators of surface detail condition changes caused by the broken tool, since the approximation subsurface is a smooth subsurface of the original surface and it only reveals the wavelength components larger than 3.14mm. Also the total energy $\overline{E_t^4}$ is not sensitive to the detail change because the approximation subsurface holds most of the energy. On the other hand, Figure 3.12(e), (f), (g) shows that the energy of the detail subsurfaces $\overline{E_h^4}$, $\overline{E_v^4}$ and $\overline{E_d^4}$ are all good indicators, especially the subsurfaces in the vertical direction, since the tooling marks are almost along the vertical direction.

Based on these results, we can conclude that the selected height or energy parameters extracted from wavelet decomposed subsurfaces can reveal surface texture changes caused by machining errors such as abrupt tool breakage, and can be used to monitor cutter conditions and to check for proper setup after a cutter change.

3.3.2 Case Study 2: Chatter Detection

Chatter in machining can cause scrap, tool breakage, and machine damage. Chatter can be detected based on the analysis of decomposed subsurfaces. As an example, we consider the machining of a compacted graphite iron (CGI) plate using a cutter with multiphase coated tungsten carbide inserts.

An example of surface height map of a part for which chatter occurred is shown in Figure 3.13 (a). When the surface is decomposed using biorthogonal wavelet 6.8 to 8 levels, the detail subsurfaces at level 5, which shows the features with scale between 3.14 to 6.28 mm, revealed the chatter marks most clearly. The approximation subsurface A_5 is shown in Figure 3.13 (b) and the summation of the detail subsurfaces $D_5^H + D_5^V + D_5^D$ is shown in Figure 3.13 (c). We can see from the figures that the chatter marks can be completely separated from the surface form at level 5.

Further, a threshold can be set up to filter out only the chatter marks on the surface, as shown in the binary image of Figure 3.13 (d), where the white pixels (with value 1) show the pixels on the chatter marks. Therefore, if chatter occurs, it can be detected rapidly from the decomposed subsurfaces. The efficacy of countermeasures can also be easily assessed using this method.

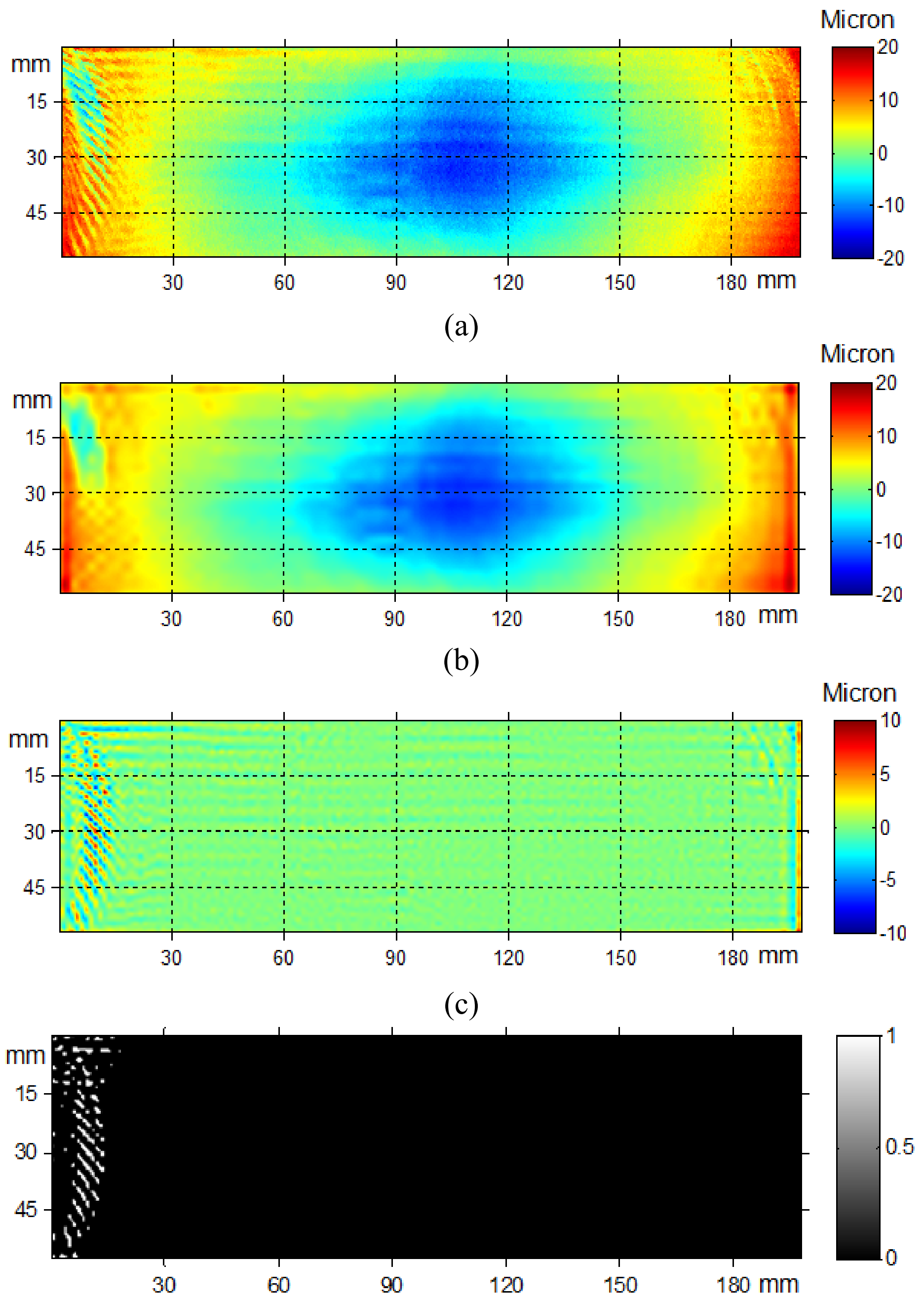

(d)

Figure 3.13 Example of chatter detection using wavelet decomposition: (a) original surface, (b) approximation subsurface A_5 (at level 5), (c) detail subsurface $D_5^H + D_5^V + D_5^D$ (at level 5), (d) binary image shows the chatter marks (in white pixels).

3.3.3 Case Study 3: Cylinder Head Mating/Sealing Surface Leak Paths Detection

This case study illustrates the application of wavelet decomposition to predict possible gasket leak paths for a cylinder head mating surface (deck surface). Leakage is always a serious concern for surfaces manufactured to contain pressurized gases in engine, compressor, and similar applications. Leakage in an internal combustion engine can lead to compression loss, power reduction, and engine overheating. Typically, a conformable interface (gasket) is applied to provide sealing between the rigid engine block and the engine head, thus to prevent leakage from or into the joined objects while under compression [94][95]. In this type of interface, long wavelengths (form distortion) can be tolerated by the conformability of the gasket material. Furthermore, some roughness effects can be tolerated [96]. However, the presence of significant middle wavelengths (large waviness peak-to-peak variation) cannot be tolerated and may result in highly localized contact and leakage.

In current practice, surface leakage is detected by measuring a limited number of points along the combustion chambers, using a Coordinate Measuring Machine (CMM), which is not reliable. The wavelet method we proposed is based on the large field of view holographic interferometer height map, which can measure the entire mating surface within 2 minutes [43] (surface larger than 300mm×300mm requires stitching of multiple images) and provide comprehensive information for the leak paths detection.

An example of a cylinder head surface height map is shown in Figure 3.14 (a). This cylinder head surface passed the leaking test by CMM, but still has serious leaking problem. We decompose the surface using biorthogonal wavelet 6.8 into 8 levels, and the detail subsurfaces at level 4, which contain the features with the physical dimension between 1.57 to 3.14 mm, reveal the tooling marks on this surface most clearly. It can be seen from Figure 3.14 (b) that the darker color (red and blue alternating) shows the tooling marks with the largest peak-to-peak variation. The larger the peak-to-peak values of the tooling marks, the higher the possibility of leakage.

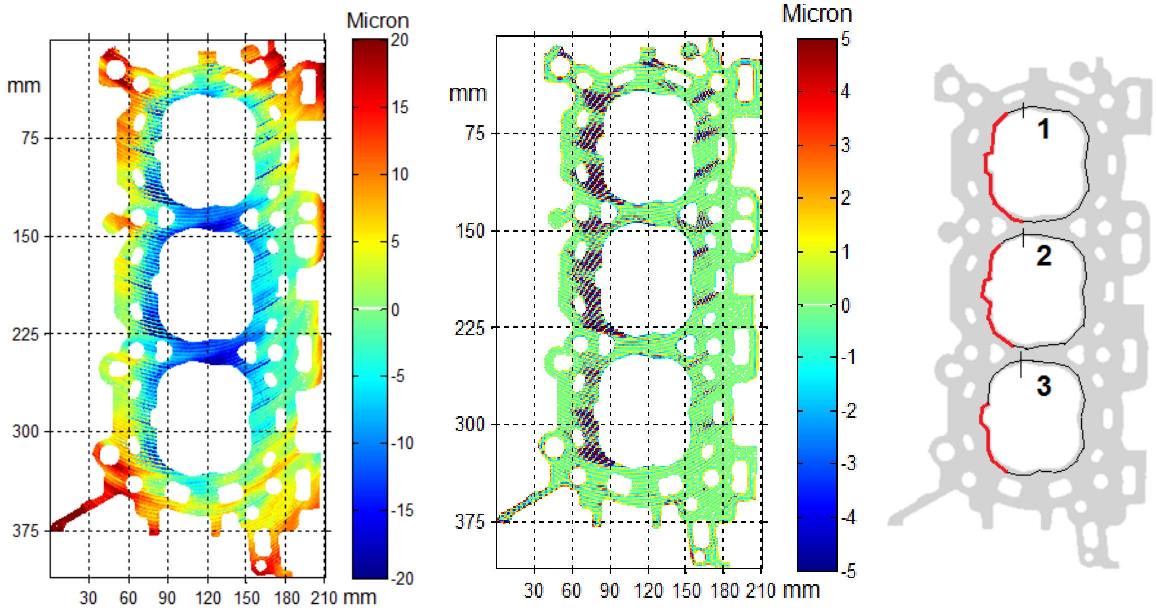

(a) (b) (c)

Figure 3.14 (a) Height map of cylinder head mating surface (b) sumation of detail subsurfaces $D_4^H + D_4^V + D_4^D$ (at level 4), (c) possible leak paths (highlight in red) along the combustion chambers.

To better assess possible leak paths, three paths around the combustion chambers of the surface are selected as shown in Figure 3.14 (c). Take path 1 as an example, Figure 3.15 shows the wavelet decomposition results of path 1. The detail sub-profile at decomposition level 4 reveals tooling marks most clearly, and is selected for the next step of analysis. The total length of this path is 320 mm, which is divided into 32 sections, 10 mm for each section. The peak-to-peak variation is calculated for each section as shown in Figure 3.16. A customer defined threshold can be set up (5 micron in this case study), and if more than 3 consecutive peak-to-peak values are larger than the threshold, which means over 30mm length of the path has peak-to-peak variation larger than 5 micron, the section is flagged as a possible leaking path. The result of this case study is shown in Figure 3.14 (c), where thick red lines mark possible leak paths along the cylinder head combustion chambers.

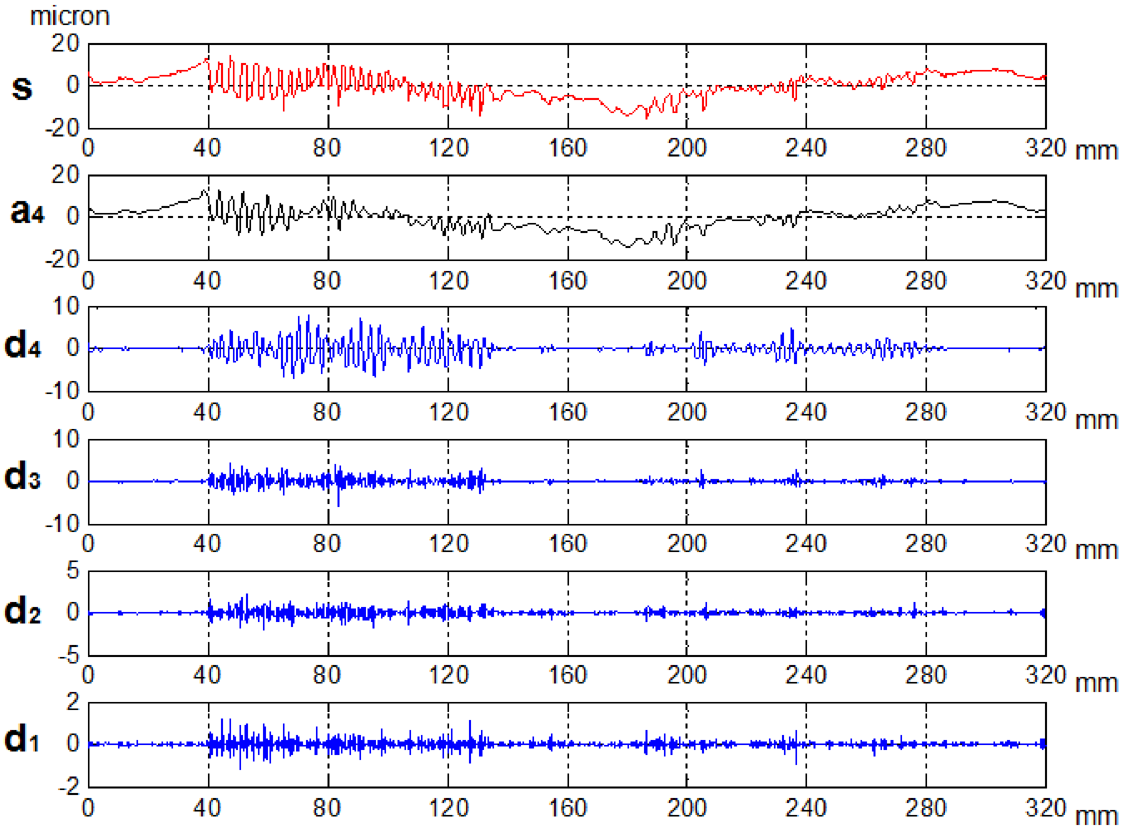

Figure 3.15 Wavelet decomposition results of path 1 around the cylinder head combustion chambers.

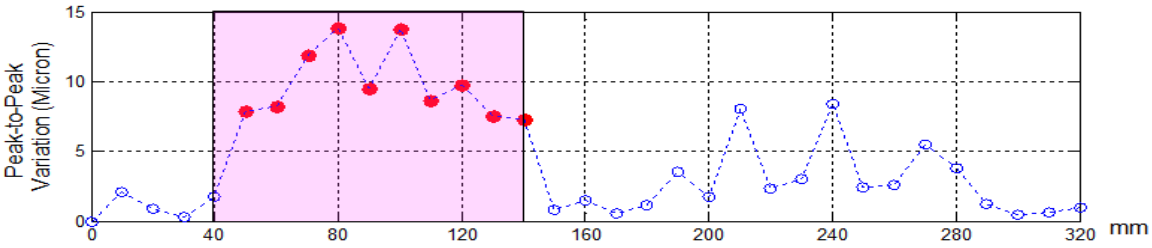

Figure 3.16 Peak-to-peak variation (sample length of 10mm) of detail sub-profile at level 4.

3.3.4 Case Study 4: Transmission Clutch Piston Surface Non-clean Up Region Detection

In case study 4, we consider the detection of non-clean up (non-machined) regions of a surface. Non-cleanup occurs due to casting dimensional variations, improper clamping, or improper tolerance stackups. In this case study, a transmission clutch piston surface is selected as an example. As shown in Figure 3.17 (a), the left lower corner of this surface was not machined as intended. Compared to the machined surface, the non-machined (cast) surface has higher roughness. Therefore, we decomposed the height map shown in Figure 3.17 (b) using biorthogonal wavelet 6.8. Figure 3.17 (d) shows the summation of the detail subsurfaces $D_1^H + D_1^V + D_1^D$ at level 1, which contains features with scale less than 0. 39 mm. This detail subsurface shows the non-clean up region most clearly.

(a)

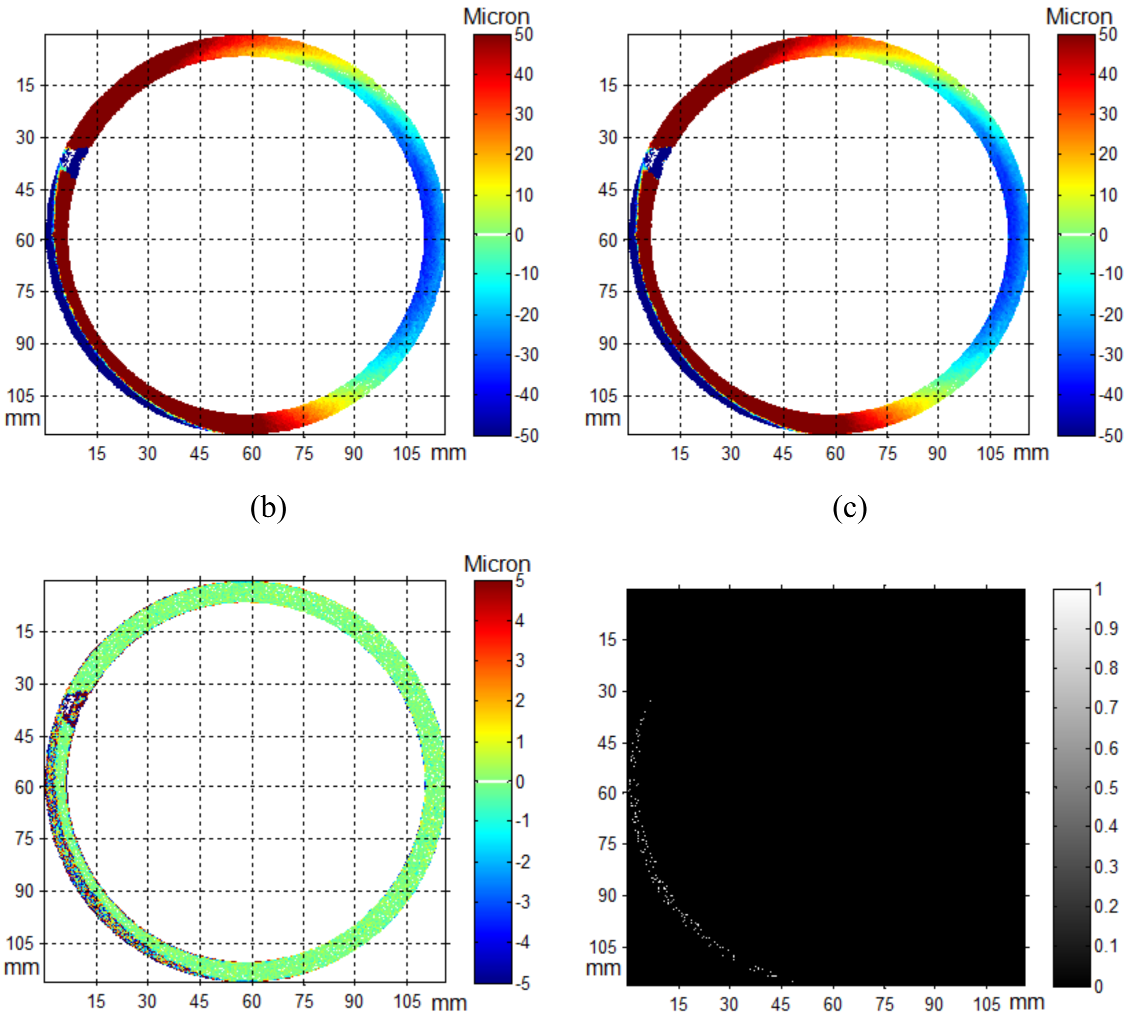

(b) (c)

(d) (e)

Figure 3.17 (a) Gray image of a non-clean up transmission clutch piston surface, (b) heght map of the piston surface, (c) approximation subsurface A_1 (at level 1), (d) the summation of detail subsurfaces $D_1^H + D_1^V + D_1^D$ (at level 1), (e) binary image which shows the non-clean up region in white pixels.

For further analysis, the non-clean up region can be automatically detected by setting up a threshold. Figure 3.17 (e) shows a binary image in which the pixels in the non-cleanup region are assigned a value of 1. This case study demonstrated that the detail subsurfaces at level 1 (feature scale less than 0.39 mm) can be utilized to detect the non-clean up defective region when machining a cast surface.

3.4 Conclusions

This chapter developed a multiple-scale two-channel filter bank wavelet decomposition algorithm for 3D engineering surface separation. Firstly, a 1D discrete wavelet was applied to decompose a 1D surface profile on a cylinder head surface measured by a profilometer. Then the 1D wavelet transform was extended to decompose and analyze a 3D surface. A two-channel filter bank diagram algorithm was designed to simplify the implementation and brings computational efficiency when applying 2D wavelets to decompose a 3D surface which contains large amount of data points. The 3D height map of a cylinder head surface measured by the holographic interferometer was used for demonstration. During the decomposition process, two important issues: the elimination of the border distortion and the transformation from the wavelet scale to the physically meaningful dimension were studied as well.

Following this, four automotive case studies were used to illustrate the application of wavelet decomposition techniques to surface functions prediction and machining errors detection. These case studies included abrupt broken tool detection, chatter detection, leak path identification, and non-clean up region detection. In these case studies, we decomposed the 3D surface into multiple-scale subsurfaces and extracted surface features from different subsurfaces to detect issues during the machining process and predict surface functional performances. The tool breakage detection and cylinder head mating/sealing surface leak paths identification were all based on the features from the detail subsurfaces which have the feature scale between 1.57 and 3.14 mm (tooling marks' scale), while the chatter detection used the features with the scale larger than 3.14 mm. In the case study of non-clean up region detection, the features at scale smaller than

0.39mm were of most interest. These case studies demonstrated that the two-channel wavelets decomposition is a very good tool to rapidly assess surface functional performance and detect errors in the machining processes based on the 3D surface features extracted from the multi-scale decomposed subsurfaces.

CHAPTER 4

SURFACE DEFECT DETECTION, FEATURE EXTRACTION AND CLASSIFICATION

4.1 Introduction

The presence of surface defects on flat machined surfaces such as cylinder heads/blocks and transmission cases may allow leaks of coolant, oil, or combustion gas between critical mating surfaces, thus causing damage to the engine or transmission. Reliable defect detection could remove defective parts before additional assembly and test costs are incurred; it could also reduce service costs when engines or transmissions fail after delivery to the consumer. Manufacturers have employed manual visual inspection methods to detect surface porosity after the machining for 30 years [97]. The human inspectors are able to look for porosities larger than 500 μm in diameter within 20-30 seconds for a part. This is time consuming, tedious, and not capable of reliably detecting defects smaller than 500 μm. Automated surface defect detection not only saves huge amount of labor cost, but also is able to reliably detect smaller defects in a shorter time. Because of this, researchers are seeking a rapid and reliable automated machine vision method for 100% inspection of machined surfaces.

Machine vision based techniques seeking low-cost, high-speed and high quality detection of defects, therefore have been applied to machined surface inspection. Much research on surface inspection is devoted to texture recognition and defect detection in textured surfaces such as fabric, wood, sand paper [98][99][100][101][102][103][104][105]. Defect detection normally relies on identification of regions that differ from either a uniform background or a textured background. The methods used for inspection include gray-level thresholding, edge detection, eigenfilters, neural networks, discrete Fourier transform, Gabor filters, wavelet transforms, model-based clustering and so on. Kumar has reviewed the advantages and limitations of all these methods [98]. Gabor filter methods were successfully applied to texture segmentation because of its joint spatial-frequency representation properties. Paper [101] investigated unsupervised web inspection using multichannel filtering scheme based on Gabor filters, and evaluated their method on a variety of fabric defects. Escofet [102] proposed a method of image processing to detect local defects in materials with periodic regular texture. In that proposed method, a multi-scale and multi-orientation Gabor filter scheme algorithm was designed to automatically segments defects from regular texture. His group also developed an automatic segmentation technique for detecting flaws in woven fabrics by applying Fourier analysis to the sample image under inspection, without considering any reference image [103]. Tsai *et al.* [104] implemented wavelet reconstruction method for inspecting surface defects embedded in homogeneous structural and statistical textures, with proper selection of a smooth sub-image or the combination of detail sub-images at different multi-resolution levels for image reconstruction. As a result of this method, the global repetitive texture pattern can be effectively removed and only local anomalies were preserved in the restored image, and then a simple binary thresholding was therefore used to separate the defective regions from the background.

Works on machined surface inspection based on machine vision techniques were mainly focused on texture recognition of machine tool wear and abnormal surface appearance [106][107][108]. There are a small number of people working on machined surface defect detection. Ramana *et al.* [109] proposed the inspection of machined surface (e.g., grinding, milling and shaping) using a widely used statistical method: co-occurrence matrix approach. The features calculated from these matrices were correlated well with surface parameters, such as roughness. Steiner *et al.* [110] developed measurement techniques for the inspection of pores on the machined surfaces. They presented a technique to detect and measure the correct size of a pore on machined surfaces and check the depth of the pore by using two cameras to reduce false detection. This technique was demonstrated and validated on the joint face of an engine cylinder head. However, they used a line scan camera and moved the engine cylinder head along x axis. The disadvantage for the line scan camera is that it does not generate a complete image at once and requires an external hardware to build up images from multiple line scans. Therefore, both the cameras needed to be placed at exactly the same distance from the inspected surface to eliminate the need for registration in the y direction. Besides they had to process registration on the x axis using the leading edge of the engine cylinder head, which may add some distortions and errors to the images. Furthermore, this device was designed only to detect pores on the machined surface, and is not capable of detecting and distinguishing other types of surface defects.

Therefore, in today's automotive industry, surface defect inspection is still done by skilled human operators, the automated defects inspection is still a topic of considerable research and people are continue proposing different techniques to realize a reliable, robust and fast enough surface inspection system to detect and classify all kinds of surface microscopic defects. Taking powertrain manufacturing as an example, Table 4.1 lists 5 types of surface defects commonly found on flat mating/sealing surfaces of machined components, which may cause serious coolant, oil, or combustion gas leakage.

Table 4.1: Definitions and characterizations of 5 types of machined surface defect.

Defect Type	**Typical cause**	**XY Size range**	**Above Surface?**	**At Surface?**	**Below Surface?**
Pore	material defect	< 1 mm to several mm	N	N	Y
2D Blemish	stain, corrosion, mark, dried detergent residue	< 1 mm to several cm	N	Y	N
Residue Dirt	handling residue, machining residue, deposition	<1 mm to several mm	Y	N	N
Scratch	sharp scraping action	width <1 mm, length = mm to cm	N	N	Y
Gouge	sharp digging action	< 1 mm to several mm	N	N	Y

The requirements for an acceptable in-line automated surface defect inspection and classification system are described in the following items:

(1) Accurately detect and classify 5 types of surface defects as described in Table 4.1. A successful surface defect detection system must incorporate the ability to detect, distinguish and understand the microscopic 2-dimensional and 3-dimensional surface defects that may otherwise be confused with each other. (The root causes of thesis defects are different.)

(2) Reliably detect the actual surface defects as well as achieve a low false alarm rate. Poor performance on either side of the decision process would reduce the value of the detection process.

(3) The system must have a spatial resolution sufficient to reliably detect defects which have a minimum dimension larger than 300 microns (except for scratches which may be smaller in their minimum dimension).

(4) The detection process must be rapid enough to follow the cycle time of the manufacturing process so that 100% inspection can be assured.

In this chapter, a novel machine vision system was designed and built using multiple-directional LED illumination. Related image processing algorithms were developed to realize 5 types of surface defects detection and classification. Our technique was demonstrated and validated on both an artificially machined surface and actual powertrain machined parts. The experimental results show that the 2D and 3D microscopic surface defects can be accurately detected and classified.

The rest part of this chapter is organized as follows: Section 4.2 presents the proposed approaches to realize defect detection and classification. In this section, the inspection procedures: (1) Image acquisition and contrast enhancement, (2) defect segmentation and feature extraction and (3) defect classification are described in detail. In Section 4.3, the results of case studies on actual automotive parts (a transmission pump surface and a cylinder head surface) are reported. According to the results, we conclude that our technique can be successfully applied to microscopic defect inspection and classification on the flat machined surfaces. This chapter is summarized in section 4.4.

4.2 Approaches

Figure 4.1 illustrates the flow chart of the overall algorithm of the defect detection and classification process. There are three main steps: step 1, image acquisition and contrast enhancement; step 2, defect segmentation and feature extraction; and step 3, defect classification. The following contents will explain each step in detail.

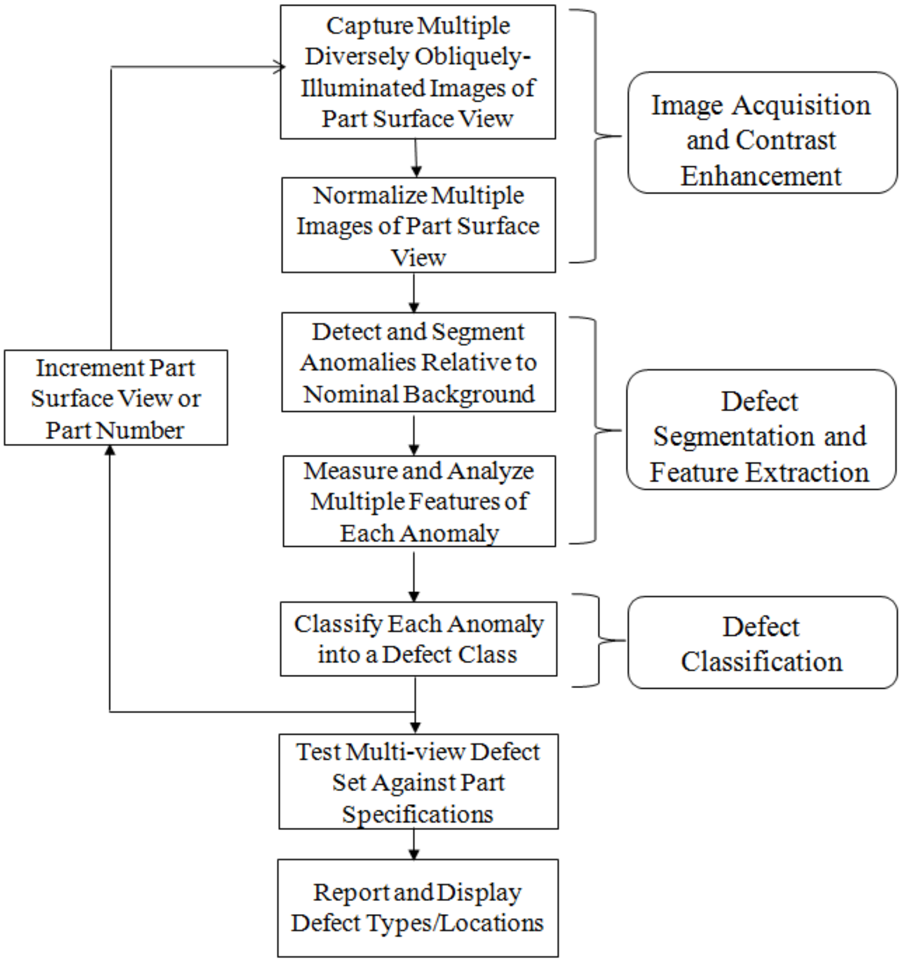

Figure 4.1 Overall algorithm flow chart of the defect detection and classification process.

4.2.1 Image Acquisition and Contrast Enhancement

4.2.1.1 Image Acquisition: Multiple Directional Illumination Structure Construction

Machine vision system has been applied to surface inspection for 30 years, but most of the efforts have been put on developing fast and reliable image processing algorithms to recognize surface texture or segment surface defects. There are only a few researchers concerned and discussed the effect of illumination directions on the feature extraction and classification. Chantler [111] showed that the directed illumination used in image acquisition process can act as a directional filter of three-dimensional texture in his paper. His work theoretically and empirically proved that changes in the illuminant direction do significantly affect the characteristics of image texture. Besides this work, Racky *et al.* [112] used several images taken under different illumination directions to segment surface deformations and embossed patterns. Lindner and Leon [113][114] presented a new method to segment images of structured surfaces from illumination series based on a parallel light source at different incident angles. They investigated meaningful surface features based on the intensity signal as well as frequency decomposition with respect to the illumination directions, and these features were then utilized to robustly segment a wide variety of textures on structured surfaces. Leung and Malik [115] provided a unified model to construct a vocabulary of prototype tiny surface patches with associated local geometric and photometric properties extracted from images under directional lights, and they studied a large collection of images of different materials such as concrete, rug, marble, leather to build 3D texton vocabulary and then used the vocabulary to characterize any materials.

In this study, the fact that illumination direction is fundamental to the surface defect detection and classification process is highly concerned, thus a multiple directional illumination structure is designed and built to acquire a series of images. The multiple directional illuminations act in combination as a directional filter of three-dimensional surface features. The inspection system and related image processing algorithms are developed to detect and classify 5 types of surface defects: pore, 2D blemish, residue dirt, scratch and gouge as listed in Table 4.1.

Porosity (pore) is caused during the casting process, if air bubbles are trapped inside a part. When the part is machined, the bubbles appear on the surface as porosity. Porosity is a type of defect below the surface and it absorbs oblique light making it appear as dark area. 2D blemish such as stain, detergent residue also appear as dark areas to the camera, which will be easily confused with pore. We used image series captured under multiple directional illuminations to distinguish 2D blemish from pore. Gouge also looks like a pore except that the shape of a gouge is less irregular compared to a pore. Scratch is another common type of defect on machined surfaces, and normally its width is less than 1 mm and its length ranges from millimeters to centimeters. When the illumination direction is perpendicular to the long edge of a scratch, it appears bright; otherwise it will be hard to observe from the background. Residue dirt appears as a bright spot on the image and the shadow will be created if illuminating the residue dirt from a low elevation angle and it will occur along the same direction of the illumination. In the applications of surface texture recognition, the result may suffer from shadows and reflections, but in our study, shadow of residue dirt and reflections from the edges of pore or gouge will be extracted as important surface features for defect classification.

A single image of surface provides not enough information to perform multiple types of defect segmentation and classification, but image series generated based on multiple directional illuminations provide a much richer information set sufficient for reliable classification.

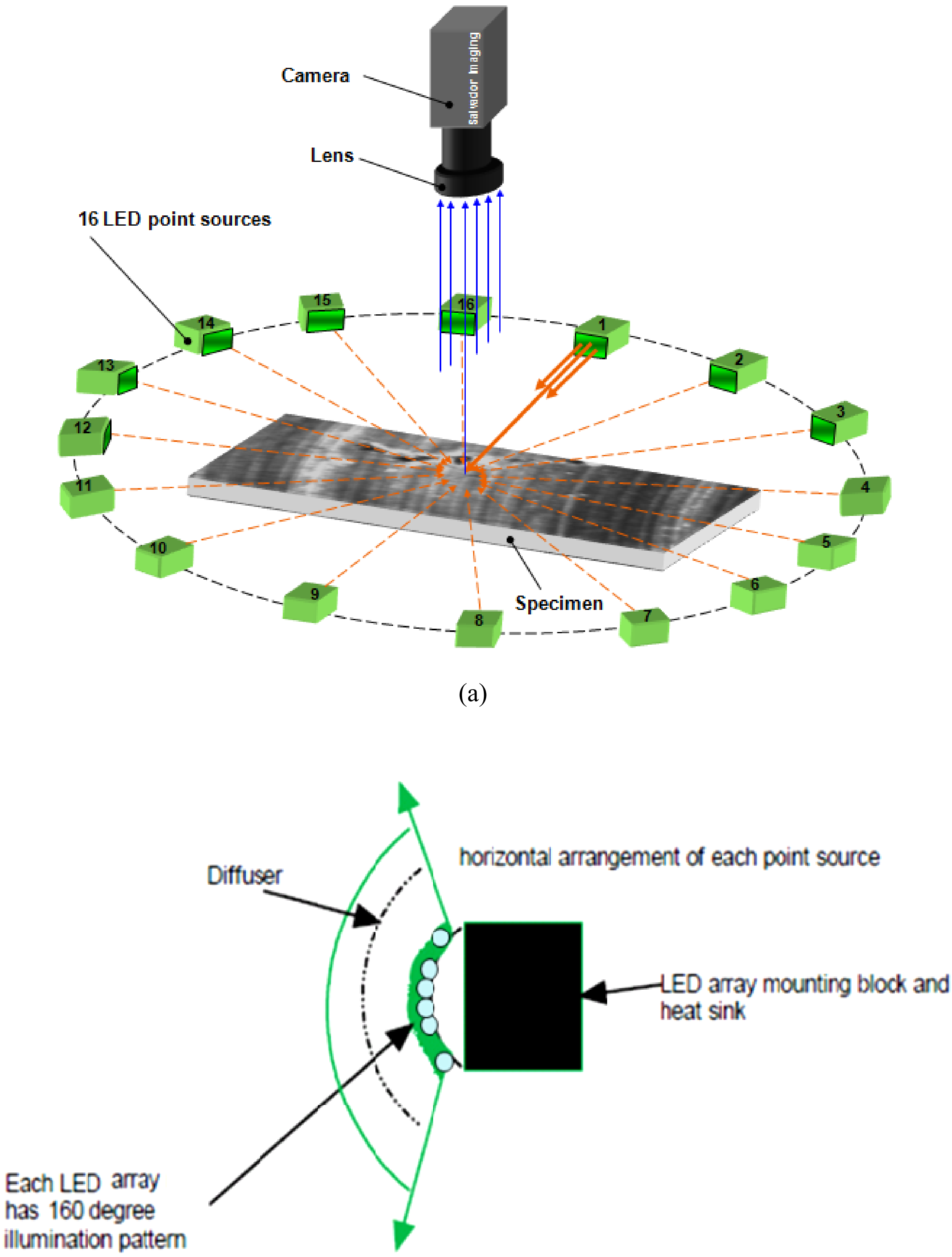

(a)

(b)

Figure 4.2 (a) Schematic of the illumination system, (b) structure of LED array mounting block.

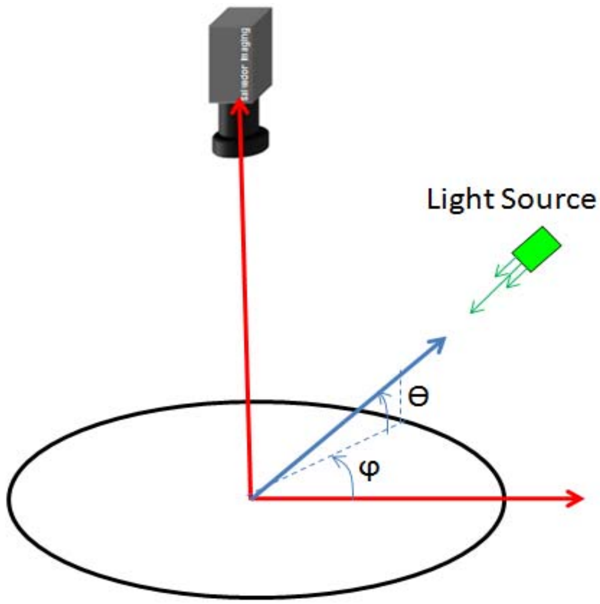

Figure 4.3 Directional illumination described by the azimuth angle φ and elevation angle θ.

Figure 4.2 (a) shows a schematic of the illumination structure: a single camera vision system involving 16 computer controlled LED blocks. The elevation angles of all the LED blocks are fixed (θ=20 degree), the azimuth angles (φ) are evenly distributed along a circle. The LED light sources illuminate the target surface with a small elevation angle from the side at different azimuth angles sequentially. The azimuth angle φ and elevation angle θ of the directional illumination are defined and shown in Figure 4.3.

In this machine vision system, a monochrome camera with 3248×4864 pixels is used and the photosensor pixel size is 7.4 µm×7.4 µm. Since this system is aiming to detect surface defects larger than 300 micron, the magnification of the system is designed to be 1/5, thus XY resolution of the system is 37.5 micron (defect larger than 300micron will contain at least 8 pixels in dimension). The camera captures 3 frames per second of 12 bits image, so that the gray level value is from 0 to 4095.

As shown in Figure 4.2 (b), for each LED block, 6 LEDs are mounted on the block, therefore each LED array has almost 160 degree spread angle, which can be seen as a parallel lighting source. For each LED block, a holographic diffuser is put in front of the LEDs, which has the transmission efficiency larger than 85%. The purpose of the diffuser is to make the illumination more uniform, and can be replaced with vellum paper to reduce the cost. For each LED block, a top and a bottom cover are added to channel the illumination to the target workpiece surface area. These covers are painted to be lambertian diffusive surfaces and have larger than 95% reflection.

The breadboard construction of the surface defect detection and classification system is shown in Figure 4.4. In our system, the field of view is 150mm×225mm, if the inspected surface is larger than the field of view, multiple views of images can be accurately stitched together with cross-correlation software. The system employs a XY moving table, which is controlled by the computer. The image sequences acquisition, image processing, and the results display are all controlled by the computer.

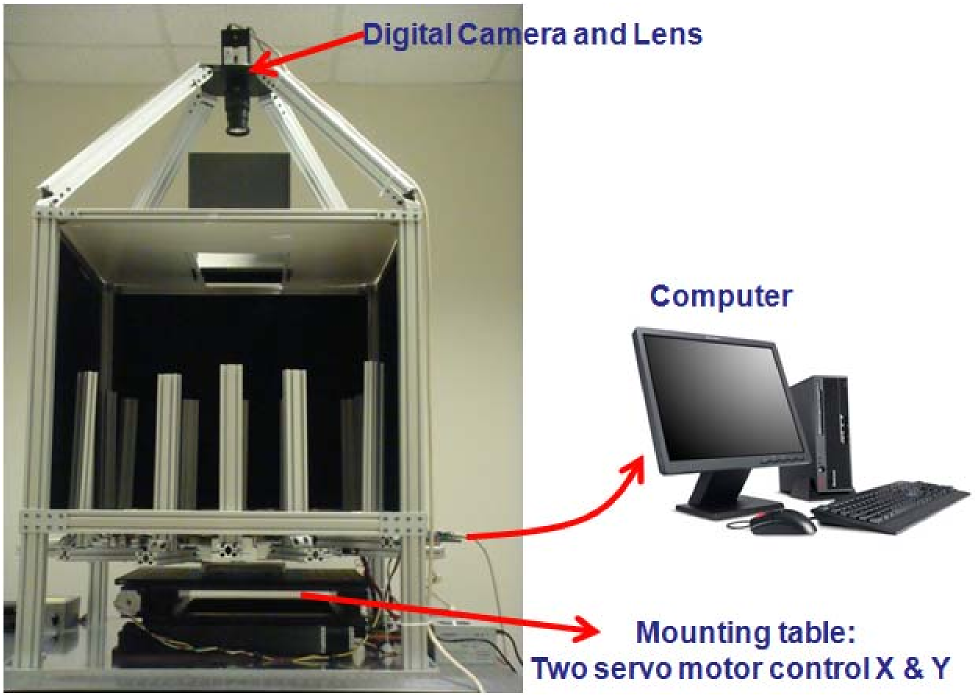

Figure 4.4 Breadboard structure of the surface defect detection and classification system.

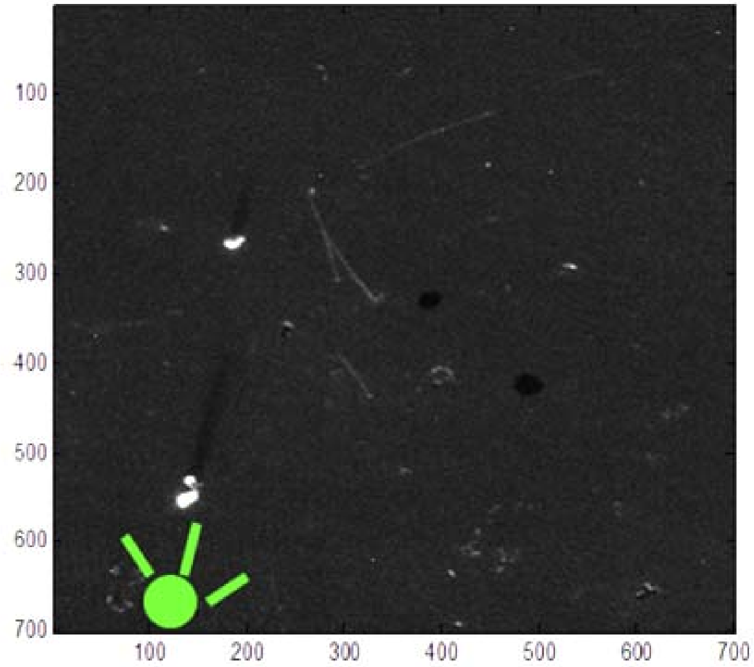

(a)

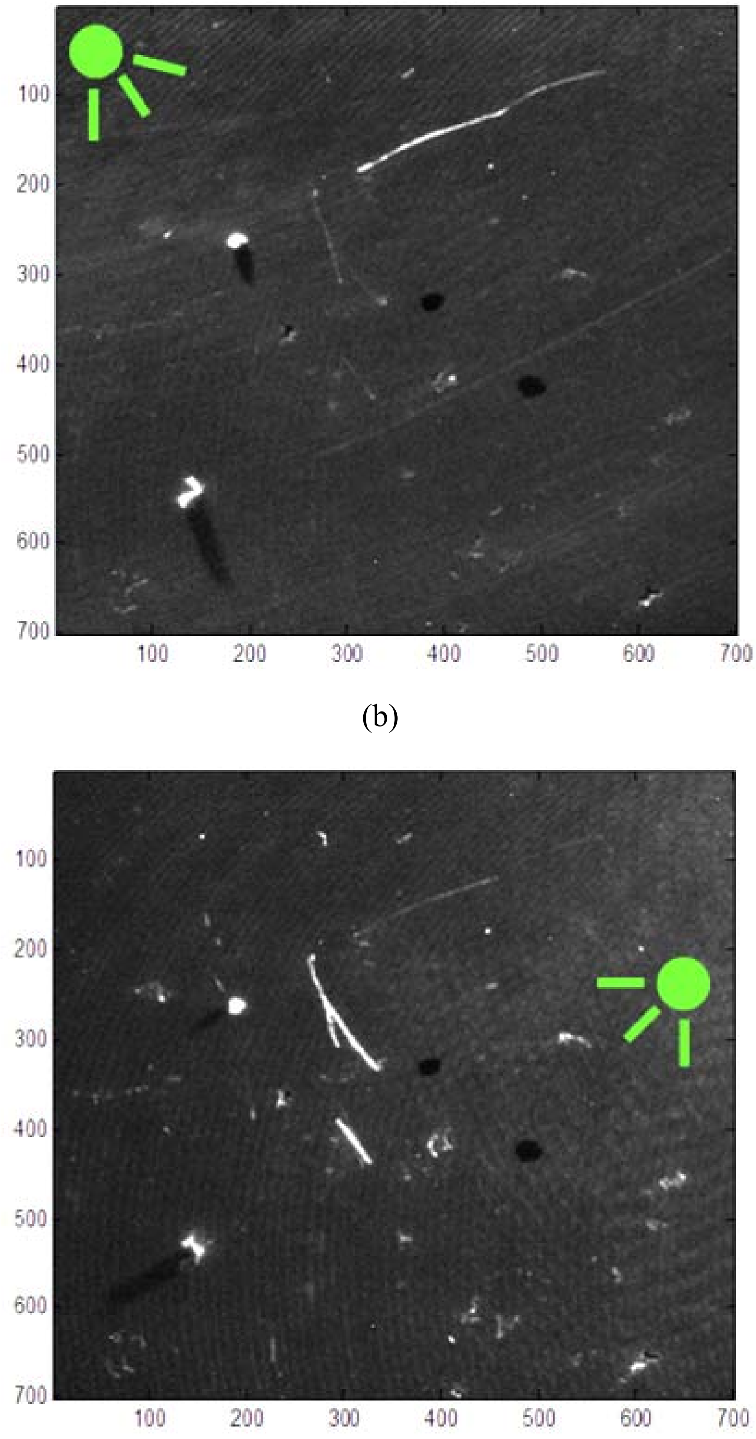

(b)

(c)

Figure 4.5 Illumination image sequences example of an artificially machined surface.

Figure 4.5 shows some examples of the image sequences of an artificially machined surface under different illumination directions. The artificially machined part contains 4 types of defects: pore, 2D blemish, residue dirt and scratch. From these images, we can tentatively observe that: if the defect is a pore below the surface, the shining edges will change when the illuminating direction changes; if the defect is a residue dirt above the surface, the direction of its shadow which is along the illuminating direction will change; if the defect is a 2D blemish on the surface, nothing changes when the illuminating direction changes. The scratches are bright in some images while cannot be observed in the others.

4.2.1.2 Image Contrast Enhancement

The first step, image acquisition provides multiple image series as the source for surface detect feature extraction and classification. Another important treatment before feature extraction is image contrast enhancement. In our illumination system, the directional lightings illuminate the target surface from the side at small elevation angle, thus the distance from each pixel on the surface to the light source is different. Not only the gray level intensity contrast of each individual image needs to be compensated, the 16 images in a series need to be adjusted to the same intensity level as well, since the uniformity of the acquired images plays a vital role in segmenting defects and simplifying the algorithms in the following steps.

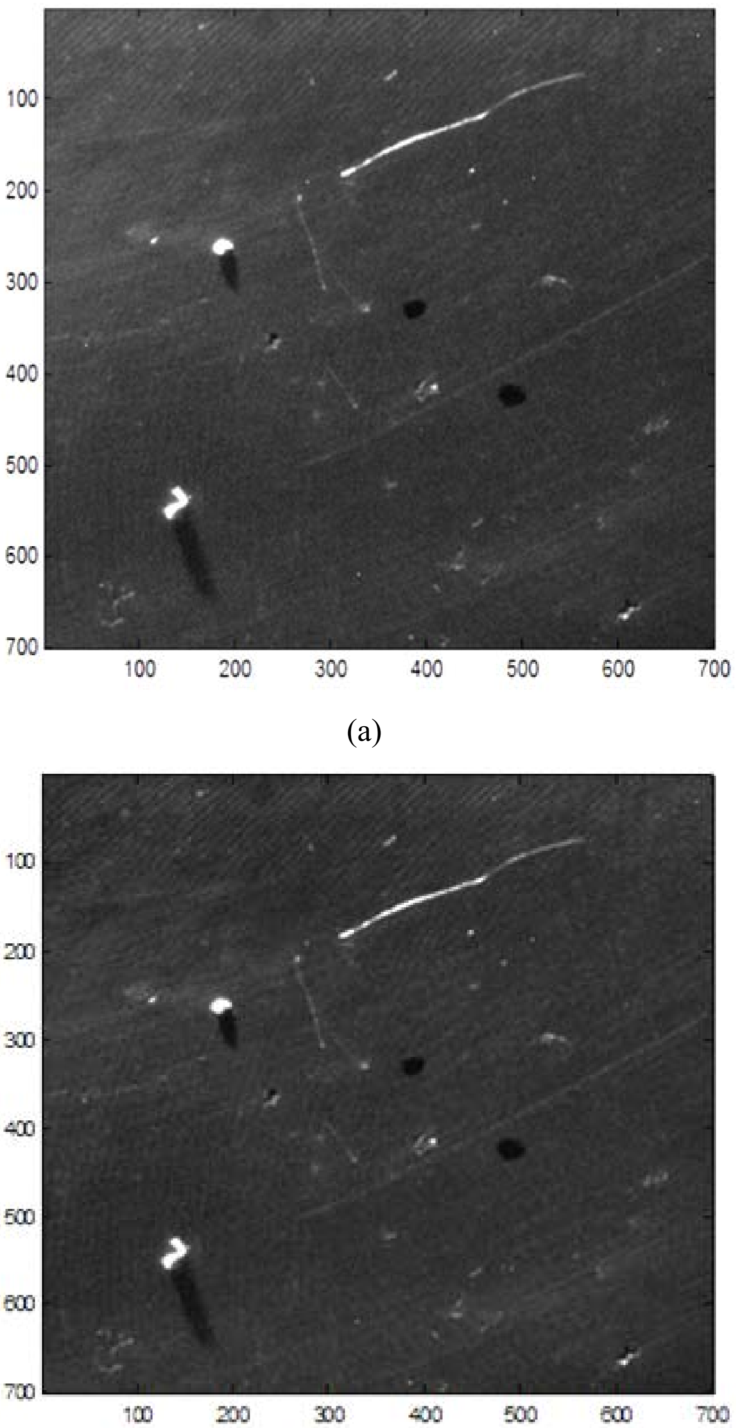

(a)

(b)

Figure 4.6 (a) An example of image before contrast enhancement, (b) after individual contrast enhancement.

Firstly, the contrast enhancement for individual image is processed. As shown in Figure 4.6 (a), the background of the original image is not uniform, the upper left corner is shinier than the rest part of the image. If the background of each individual image is not uniform, the feature extraction process in the next step will be greatly affected. The method implemented to normalize individual image intensity is to fit a polynomial regression surface to the image. The polynomial regression functions are shown in equation 4.1. The first order, second order and third order polynomial models are tried to fit to the image in Figure 4.6 (a). Then the R^2 values (range from 0~1) are compared to check the goodness of the fits. In the regression operation, the R^2 coefficient of determination is a statistical measure of how well the regression plane approximates the real data points. An R^2 value of 1.0 indicates that the regression plane perfectly fits the data. The computation of R^2 value is defined in equation 4.2, where y_i is the observed data while f_i is the modeled (predicted) value, SS_{err} is the sum of squares of residuals and SS_{tot} is the total sum of squares [63].

First order: $Z = a_1x + a_2y + a_3$

Second order: $Z = a_1x^2 + a_2xy + a_3y^2 + a_4x + a_5y + a_6$

Third order: $Z = a_1x^3 + a_2x^2y + a_3xy^2 + a_4y^3 + a_5x^2 + a_6xy + a_7y^2 + a_8x + a_9y + a_{10}$ (4.1)

$$R^2 \equiv 1 - \frac{SS_{err}}{SS_{tot}}, \quad SS_{err} = \sum_i (y_i - f_i)^2, \quad SS_{tot} = \sum_i (y_i - \bar{y})^2 \tag{4.2}$$

Figure 4.7 shows the polynomial surfaces fitted to the image, we can compare the R^2 values that when the order of the polynomial function increases from the first order to the second order, R^2 value increases significantly, but when the order increases from the second order to the third order, the R^2 value does not increase significantly. That means the second order polynomial regression model is adequate, a higher order model will largely increase the calculating time and may cause over-fit problem. After removing the background difference, the image is shown in Figure 4.6 (b). We can see that the background intensity of the image become more uniform.

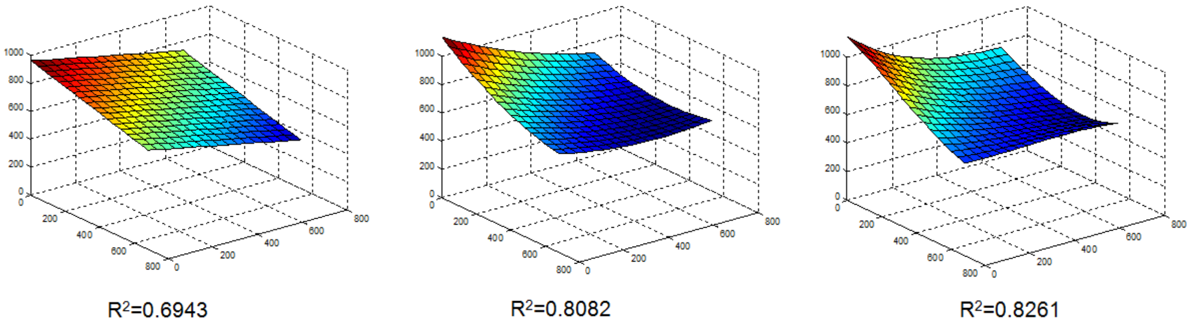

(a) (b) (c)

Figure 4.7 Polynomial regression planes fitted to the image: (a) first order polynomial plane, (b) second order polynomial plane, (c) third order polynomial plane.

Secondly, contrast enhancement is performed for all the 16 images captured under multiple illumination directions in an illumination sequence. Shown in Figure 4.8 (a) and (b), are two images from the image sequence, the gray level intensities are not at the same level. We can also see the difference from the probability density function (pdf) chart shown in Figure 4.8 (c) and the cumulative distribution function (cdf) chart shown in Figure 4.8 (d) that both the mean intensity value and the intensity distribution are different for the two images. The contrast equalization among images is desired, since this will make the feature exaction process in the next step much simpler and faster.

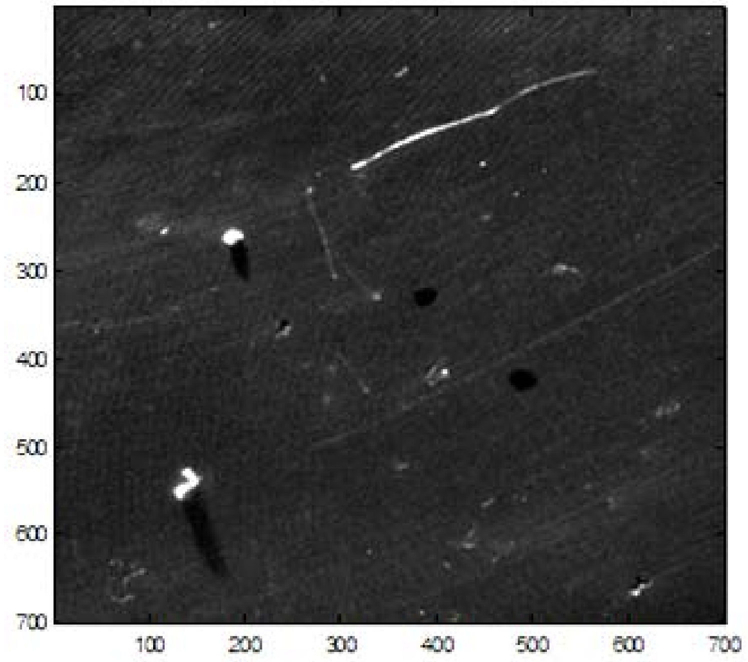
100
200
300
400
500
600
700
100
200
300
400
500
600
700

(a)

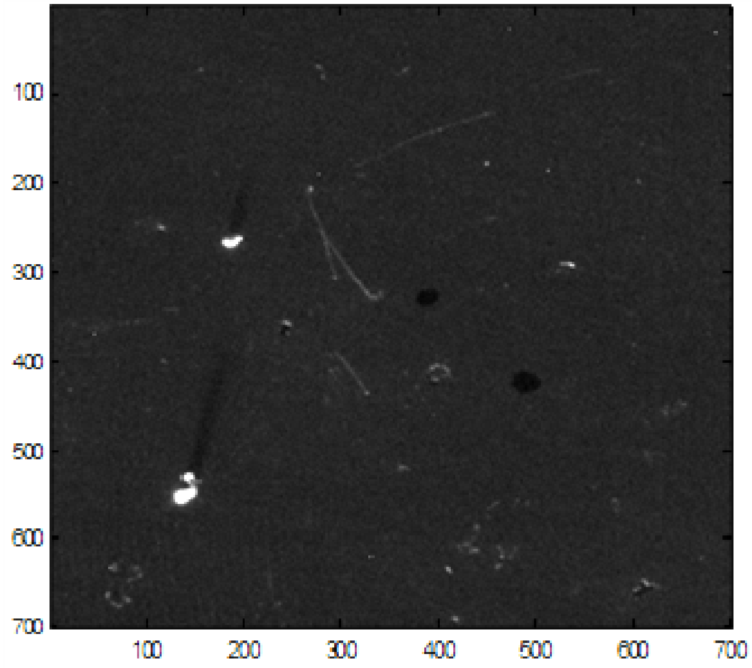
100
200
300
400
500
600
700
100
200
300
400
500
600
700

(b)

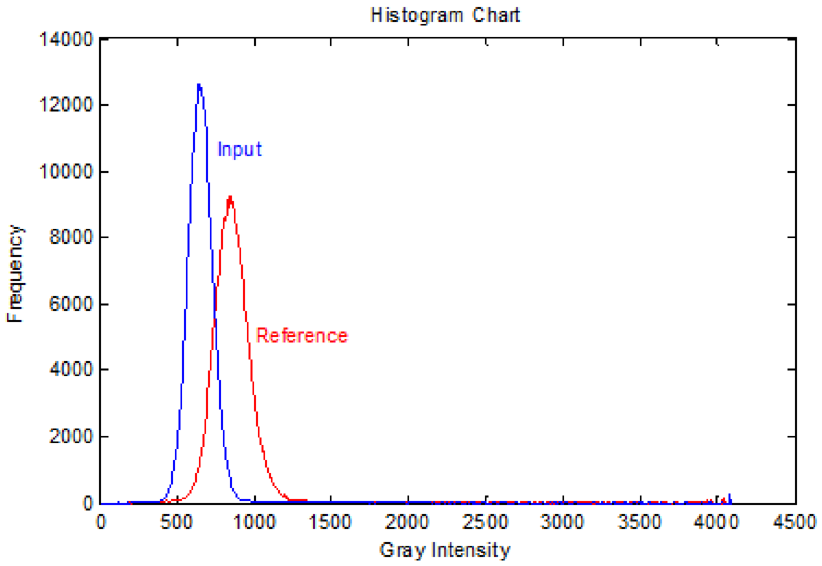

(c)

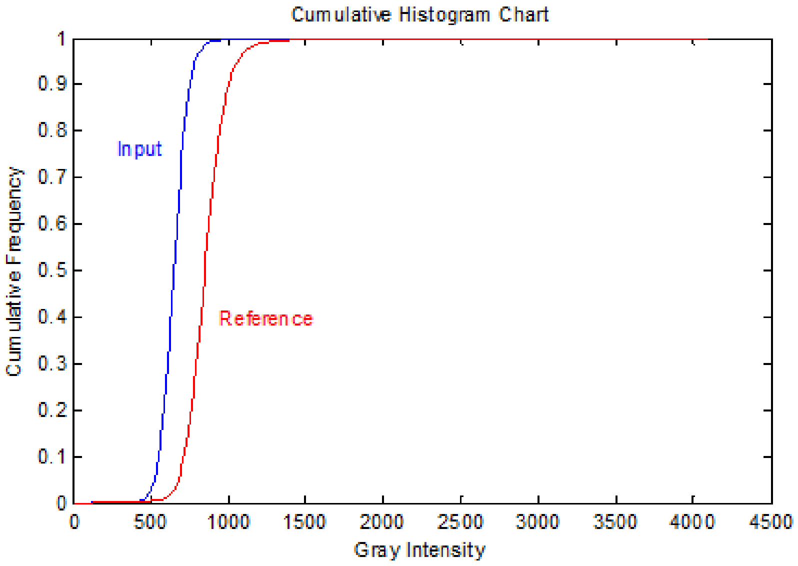

(d)

Figure 4.8 An example of contrast equalization of 16 images (a) Reference image (can be any one of the 16 images), (b) an example of input image (one from the rest 15 images), (c) pdf charts of the reference and input images, (d) cdf charts of the reference and input images.

Gain/offset correction and histogram equalization are two classic algorithms that make the input image span the entire dynamic range of the output intensity channel [116]. Gain/offset correction method relies on assuming an underlying pdf of the pixel intensities, which can be assumed to be uniform or Gaussian. But the method is very sensitive to noise and image content. The method of histogram equalization is to transform the input image in such a way that the output image has a uniform pdf [116]. In our image processing algorithms, for each anomaly segmented from the image, 16 frames of this segmented anomaly will be analyzed together. The similarity of the intensity levels among these image series is more important than whether the distribution spans a uniform pdf or not. In other words, the 16 images are required to approximately have the same pdf distribution. Therefore, in our algorithms, a histogram equalization operation is performed by selecting one of the 16 images as the reference image (can be any one of the 16 images), and enhancing the contrast of other images by transforming the values in the intensity image, so that the histogram of the output image approximately matches the histogram of the reference image.

Let's define K=4096 for the 12 bits gray image, $p(k)$ denotes the frequency at intensity value k (the number of pixels at gray level k divided by the total number of pixels at all gray levels), $k = 0,1,...,K-1$. The cumulative distribution function (cdf) of intensity value x is defined as:

$$F(x) = \sum_{k=0}^{K-1} p(k)u(x-k), \qquad normalized \;\; p(k): \quad \sum_{k=0}^{K-1} p(k) = 1 \tag{4.3}$$

Where, u(.) is the unit step function, only when $k \le x$, $u(x-k) = 1$, otherwise, $u(x-k) = 0$.

Suppose the cdf of the reference image at intensity value x is:

$$F_R(x) = \sum_{k=0}^{K-1} p_R(k)u(x-k) \tag{4.4}$$

The cdf of input image at intensity value x is:

$$F_X(x) = \sum_{k=0}^{K-1} p_X(k) u(x-k) \tag{4.5}$$

The transformation is then defined as:

$$y = T(x) = F_R^{-1}(F_X(x)), \quad (equivalent \quad to: \quad F_R(y) = F_X(x)) \tag{4.6}$$

Which means for each input k_i (pixel intensity value), it should be mapped to a value k_o that:

$$F_R(k_o) = F_X(k_i) \tag{4.7}$$

We can also express the transformation in the following way:

$$\sum_{k=0}^{k_o} p_R(k) \approx \sum_{k=0}^{k_i} p_X(k) \tag{4.8}$$

In the numerical calculation, k_o can be obtained by:

$$T(k_o) = \max\left\{ k_o : \sum_{k=0}^{k_o} p_R(k) \le \sum_{k=0}^{k_i} p_X(k) \right\} \tag{4.9}$$

By using equation 4.9, the output image is shown in Figure 4.9 (b), it can be seen that the contrast of Figure 4.9 (b) is enhanced to be similar to Figure 4.9 (a), which is the reference image. Figure 4.9 (c) shows the cumulative distribution histogram charts for the reference and output images, we can see clearly that the cumulative histogram chart of the output image is approaching that of the reference image. This procedure is repeated to all of the rest 14 images. Consequently, after the histogram equalization process, the intensity values of the image serious will all have similar intensity distribution.

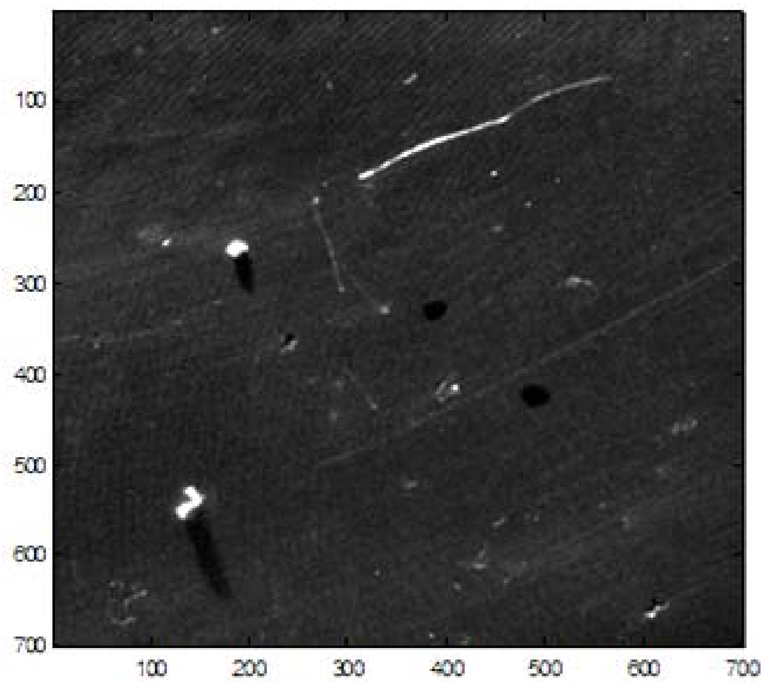
100
200
300
400
500
600
700
100
200
300
400
500
600
700

(a)

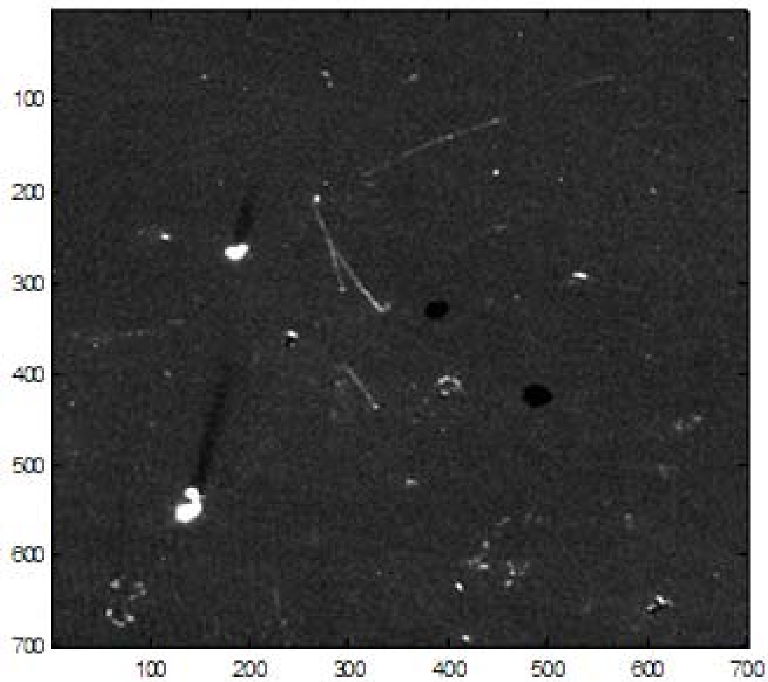
100
200
300
400
500
600
700
100
200
300
400
500
600
700

(b)

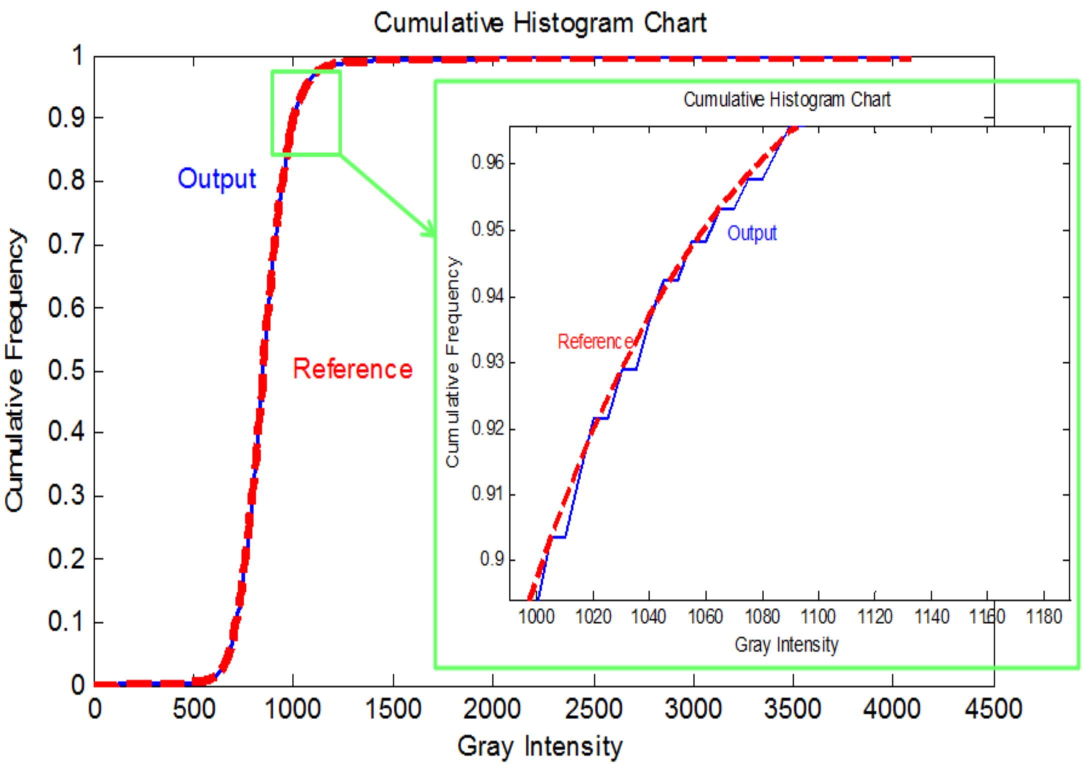

(c)

Figure 4.9 Reference image, (b) output image, (c) cdf charts of reference and output images

4.2.2 Defect Segmentation and Feature Extraction

4.2.2.1 Defect Segmentation from Background

After image acquisition and contrast enhancement, the next step is defect segmentation and feature extraction. For initial segmentation, the core portion of each anomaly is first extracted from the background, which does not contain the shadow of an anomaly (if applicable). To process the segmentation, the 16 images are added together to obtain an average intensity map, as shown in Figure 4.10. The advantage of segmenting anomalies from an averaged image is that, this process can smooth and average out the tooling marks on the machined, which may affect the defect segmentation. After the initial segmentation based on the average intensity map, the bounding box of each anomaly can be found. And then, for each anomaly, only the pixels inside the bounding box are processed in order to speed up the calculation.

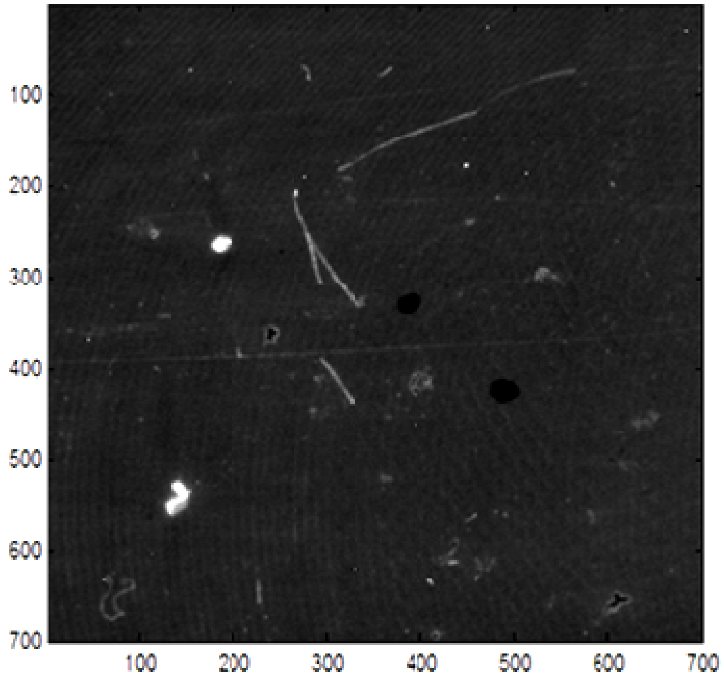

Figure 4.10 Average intensity map of the 16 frames.

The methods for image segmentation are generally based on one of the two basic properties of image intensity values: discontinuity and similarity [116][117]. The approach of the first category is to segment an image based on abrupt changes in intensity, such as edges. The method in the second category is based on partitioning an image into regions that are similar according some predefined criteria. In our case, we are aiming to extract small anomalies from the background, thus we use the approaches in the first category. In the first category, edge detectors and thresholding methods are the most popular methods to segment anomalies based on the intensity differences [117]. In our study, a global thresholding method is proposed because of its intuitive properties and simplicity of implementation. And based on the specific application of our case, the edge pixels of anomalies are extracted to improve the global thresholding result.

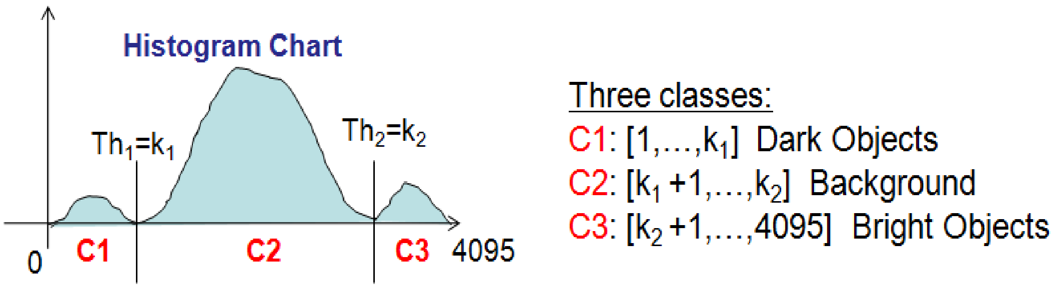

Figure 4.11 Schematic diagram of thresholding method based on histogram distribution.

As shown in Figure 4.11, three classes C_1, C_2, C_3 are defined and two thresholds k_1, k_2 are used for separating the three classes. The pixels with intensity less than k_1 belongs to Class C_1, they are dark objects. Pixels with intensity larger than k_2 are in Class C_3, they are bright objects. Pixels between k_1 and k_2 are background pixels, in Class C_2. The key point in this step is to find optimal thresholds k_1 and k_2 thus to properly segment both the bright and dark objects from the background.

The method we proposed is choosing global thresholds based on the image histogram distribution, but not all the pixels on the surface are considered, since in our application, the background pixels are dominant compared to the objects pixels. A good threshold can be selected when the histogram peaks are tall, narrow, symmetric and separated by deep valleys. If the background pixels compared to the objects are dominant, the peaks of both bright and dark objects will be submerged into noises. Therefore, one approach we use to improve the shape of histograms is considering only those pixels that near the edges between the objects and background. This way, the histogram would be less dependent on the relative sizes of objects and the background.

The probability that any of those pixels lie on objects would be approximately equal to the probability that they lie on the background, thus improving the symmetry of the histogram chart.

Any edge detector is applicable to extract the pixels lie on the edges. In our study, Canny edge detector [118] is used, since it is the optimal edge detection algorithm [116], and "optimal" means: good detection, good localization. Besides these, Canny edge detector is also robust over image noises. Then a morphological dilation operation was performed to extract the pixels near the edges of the objects.

Figure 4.12 (a) shows the histogram chart of all the pixels on the image, and because of the domination of the background pixels, the bright objects and dark objects are submerged into background pixels. Figure 4.12 (b) shows the histogram chart of only the pixels near the edges of the objects, we can see clearly three well separate peaks. Therefore the two thresholds k_1=650, k_2=1950 can be easily defined by smoothing the histogram chart and finding the thresholds between the peaks.

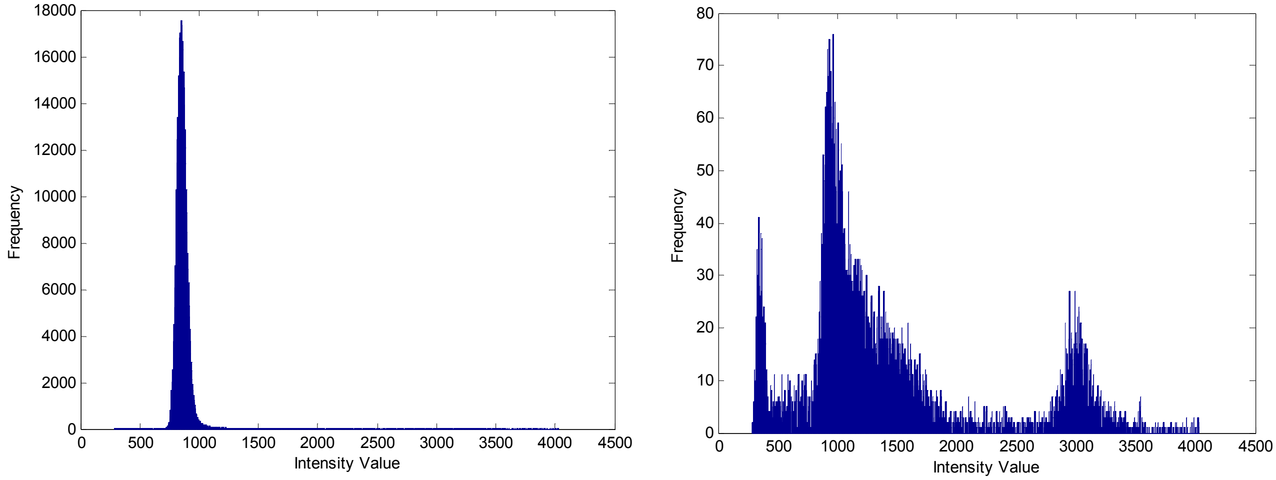

(a) (b)

Figure 4.12 (a) Histogram chart of all the pixels on the image, (b) histogram chart of only considering the pixels near the edges of the objects.

According to the thresholding process, both the dark and bright objects can be properly extracted from the background. A morphological opening operation is then used to eliminate the objects which contain less than 60 pixels. An anomaly with size smaller than 60 pixels (dimension less than 300 micron) is not considered as surface defect. The exacted anomalies are marked by the white pixels in the binary image in Figure 4.13 (b). After the segmentation, the bounding box of each anomaly can be found, as shown in Figure 4.13 (c). In order to include the shadows (if applicable) in the region of interest for each anomaly, the bounding box is enlarged by 30 pixels at each side to define the region of interest for each anomaly.

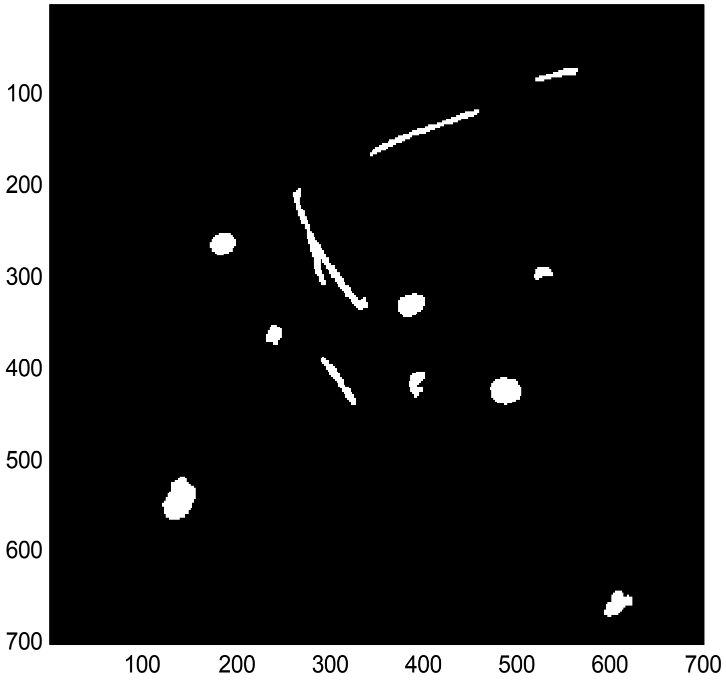

(a)

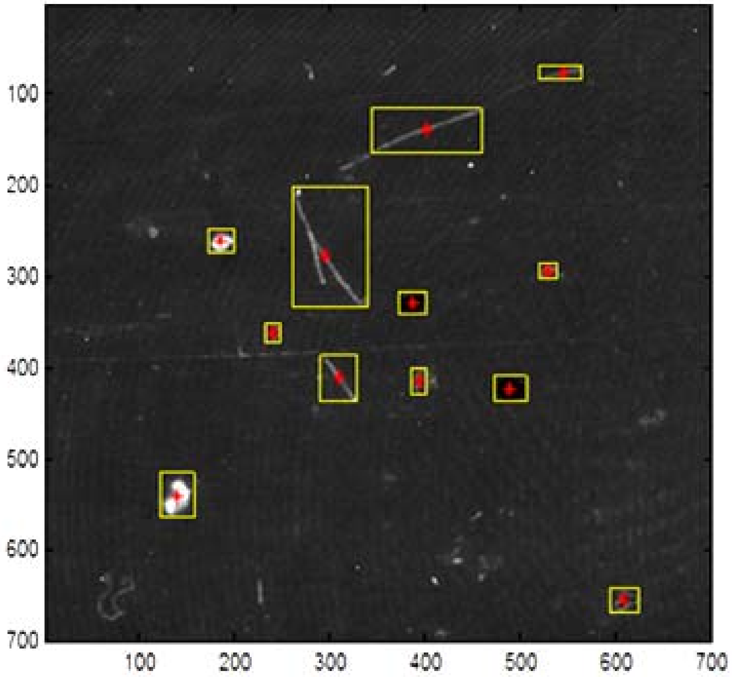

(b)

Figure 4.13 (a) Binary image of Figure 4.10 where the while pixels show the extracted Class C_1 (dark objects) and Class C_3 (bright objects) pixels, (b) bounding box of each anomaly.

4.2.2.2 Defect Feature Analysis

After initial segmentation, each anomaly can be analyzed independently and several anomalies can be analyzed in parallel to speed up the process and only the pixels defined as the region of interest of each anomaly will be processed. Each anomaly has 16 frames captured under different LED illumination directions. The bright portion and dark portion (shadow) of an anomaly are segmented separately, if some anomaly does not have bright or dart portion, the segmented bright or dark region will be empty. Figure 4.14 (a) shows the intensity map (one of the 16 frames) of an anomaly as an example. With a thresholding process, the white pixels in Figure 4.14 (b) shows the selected pixels which have the intensity larger than the threshold; in Figure 4.14 (c), the selected point clouds containing less than 15 pixels are removed; and in Figure 4.14 (d) among the remaining point clouds, the largest point cloud is extracted as the bright portion of this anomaly. The same algorithms are processed for the segmentation of the dark portion of this anomaly, the steps are shown in Figure 4.14 (e)-(h). One thing has to be pointed out that, this method is extremely useful for extracting the dark portion of an anomaly, since the contrast between the dark portion and the background is lower than the contrast between the bright portion and the background in our application.

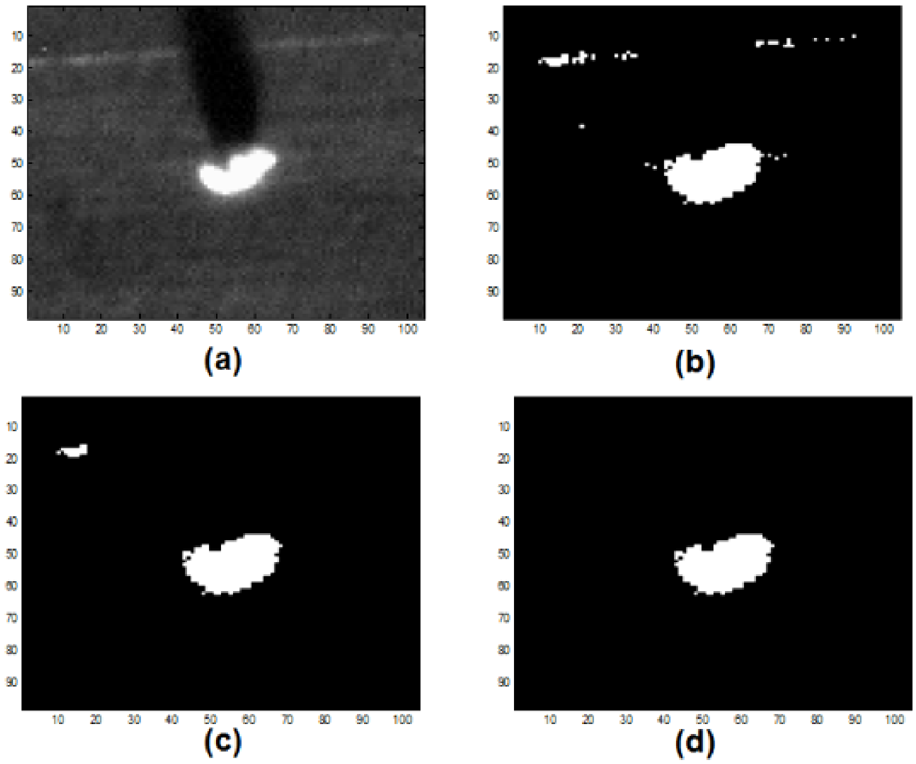

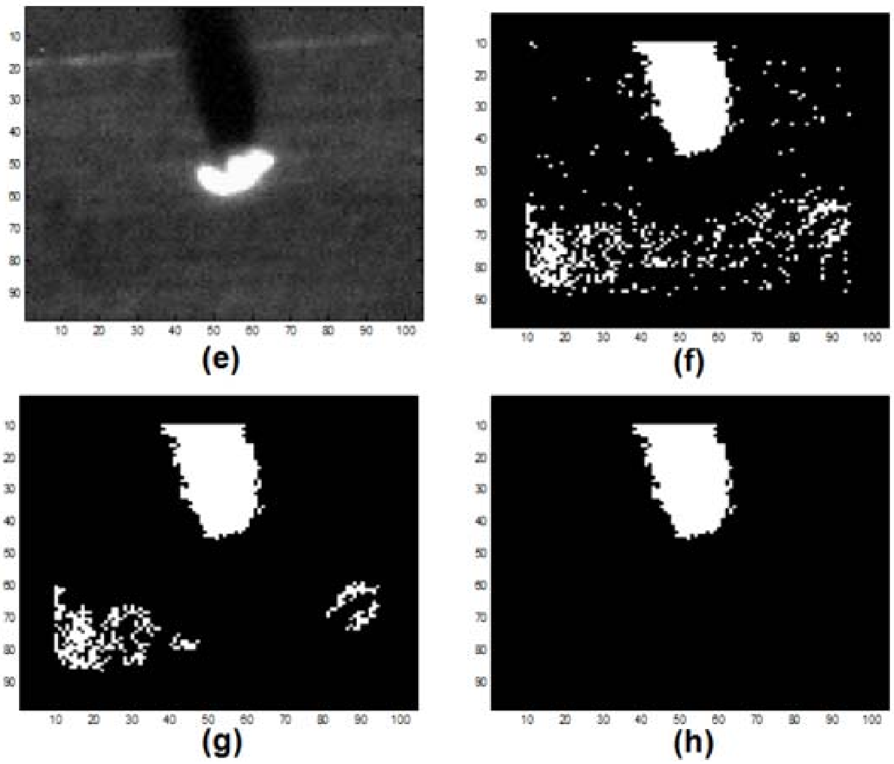

Figure 4.14 (a)-(d) The procedures for bright portion segmentation for an anomaly, (e)-(h) the procedures for dark portion segmentation for an anomaly.

After segmenting the bright and dark portion of an anomaly, the bright to dark angle and the dark to bright angle of each anomaly are calculated. The definition of these angles is shown in Figure 4.15 (a) and Figure 4.16 (a) respectively. If an anomaly does not contain bright portion or dark portion, it will not have the bright to dark angle or the dark to bright angle.

The purpose of calculating the bright to dark angle and the dark to bright angle of each anomaly is to fit a correlation coefficient between these angles and the LED illumination angles. Figure 4.15 (b) shows an example of a scatter plot of the LED illumination angles (azimuth angles) versus the bright to dark angles of the anomaly shown in Figure 4.15 (a) and a robust least squares regression line fitted to these data. Figure 4.16 (b) shows another example of a scatter plot of the LED illumination angles versus the dark to bright angles and a robust least squares regression line fitted to the data. The correlation coefficient of the regression will be later used to classify the anomalies. The LED illumination angles of the 16 frames are listed in Table 4.2.

Figure 4.17 (a)-(d) show the images of four anomalies we selected as the examples in the following analysis. Table 4.3 lists some important features calculated for the four anomalies in order to classify these anomalies into different defect classes. Feature "core area" is measured as the number of pixels inside the edge of the core area of an anomaly. Feature "major axis length" is the distance between two farthest pixels, which is also measured in pixels. Feature "minimum width" is approximately equal to the core area divided by the major axis length. Roundness is defined in equation 4.10, the roundness value of a perfect circle is 1, while that of a line is 0.

$$Roundness = \frac{4\pi \times Area}{Perimeter^2} \tag{4.10}$$

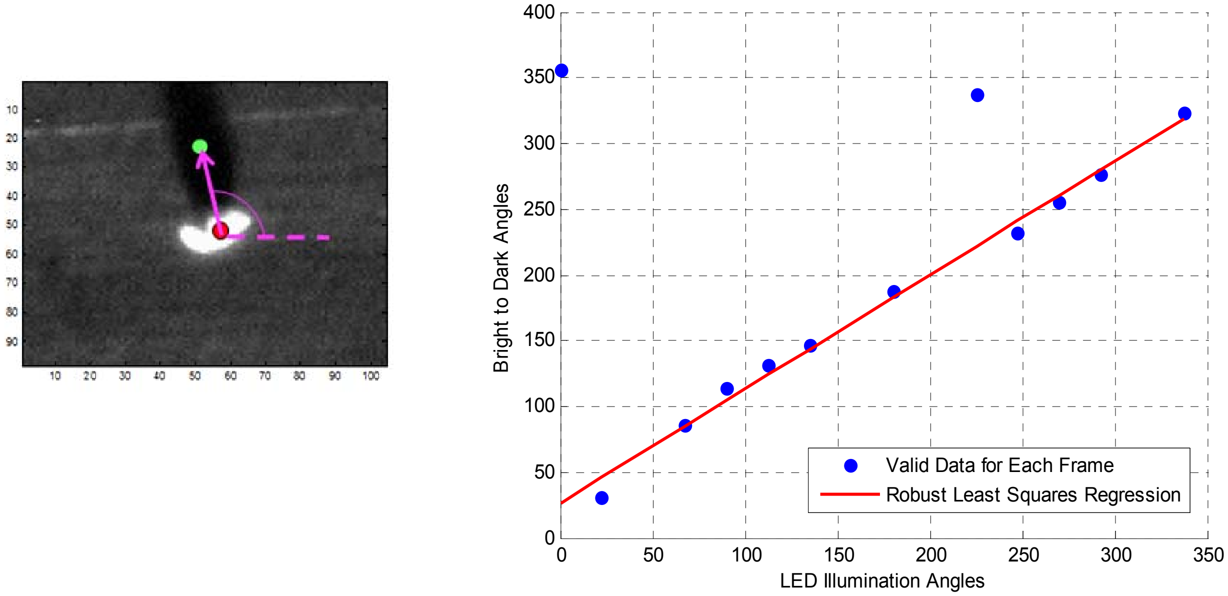

(a) (b)

Figure 4.15 Definition of the "bright to dark angle", (b) LED illumination angles versus the bright to dark angles for 16 frames.

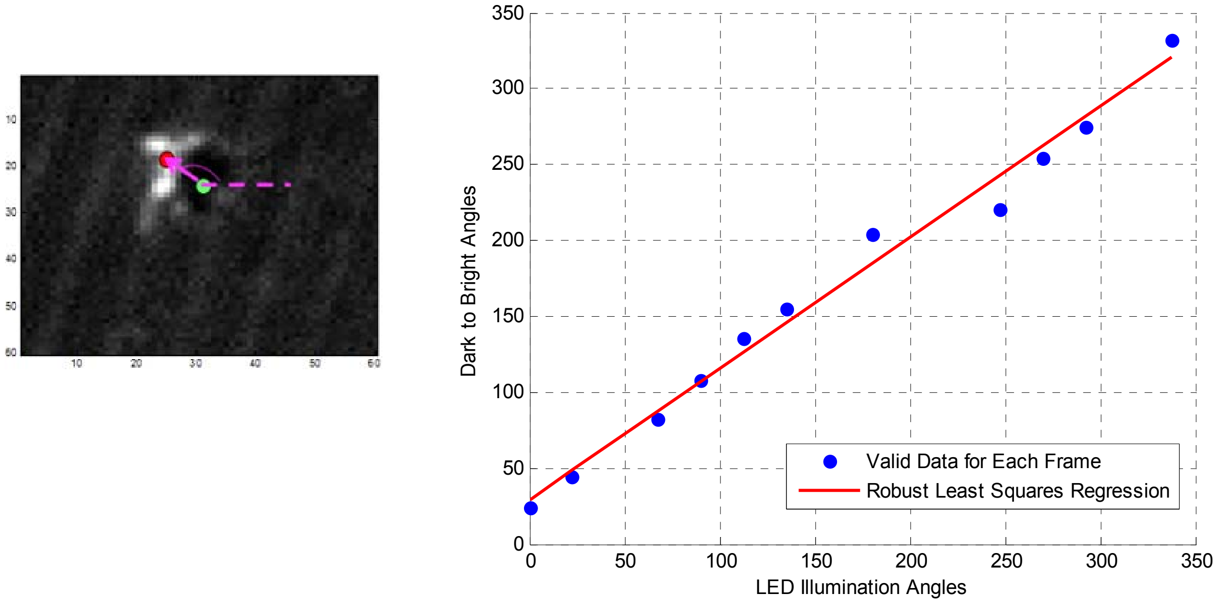

(a) (b)

Figure 4.16 (a) Definition of the “dark to bright angle”, (b) LED illumination angles versus the dark to bright angles for 16 frames.

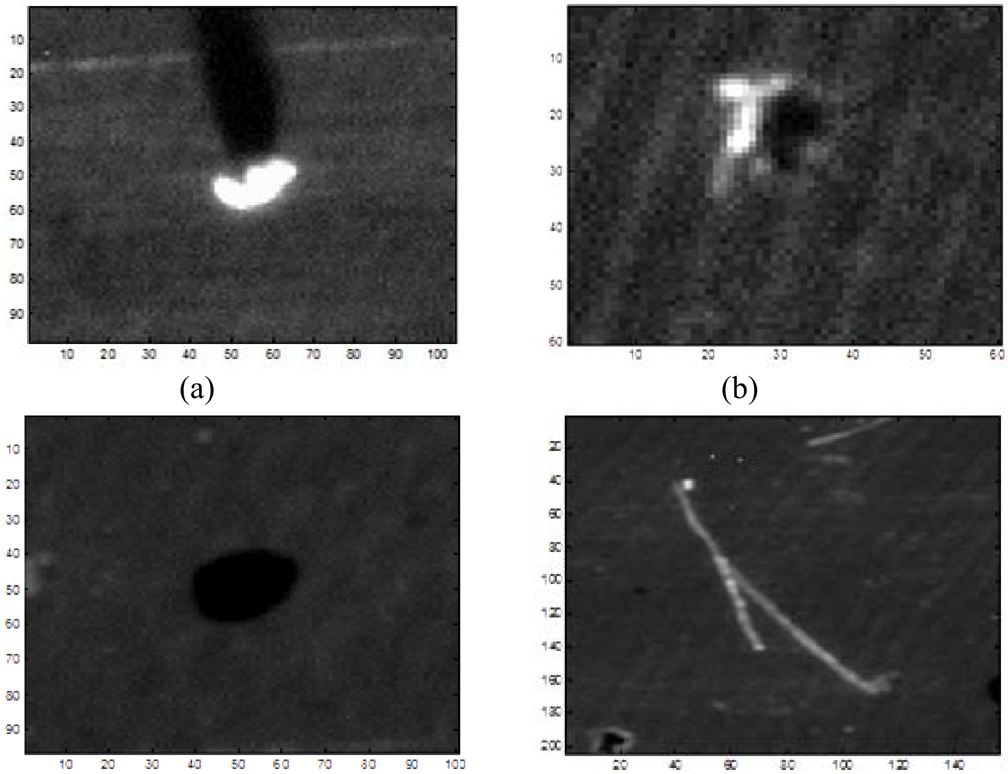

(a) (b)

(c) (d)

Figure 4.17 Intensity maps of (a) Anomaly #1, (b) Anomaly #2, (c), Anomaly #3 (d) Anomaly #4.

Table 4.2: LED illumination angles (azimuth angle φ) of the 16 frames.

Frame #	1	2	3	4	5	6	7	8
LED Illumination Angles (degree)	22.5	45	67.5	90	112.5	135	157.5	180
Frame #	9	10	11	12	13	14	15	16
LED Illumination Angles (degree)	202.5	225	247.5	270	292.5	315	337.5	360

Table 4.3: Important features of anomaly #1, #2, #3 and #4.

	Core Area	Core Area Intensity	Background Intensity	Roundness	Major Axis Length	Minimum Width
Anomaly #1	290	2389	941	0.8004	21	13
Anomaly #2	236	639	975	0.6753	19	12
Anomaly #3	438	650	930	0.6280	26	17
Anomaly #4	259	1373	954	0.1481	133	3

	Valid # of Bright to Dark angles	Angle Correlation Coefficient
Anomaly #1	12	0.992
Anomaly #2	11	0.995
Anomaly #3	3	Not valid
Anomaly #4	5	0.326

4.2.3 Defect Classification

Table 4.4 lists 5 classes of surface defect we studied in this research. In the future work, the classes of defect can be extended. There are many types of classification methods, the most widely used classifiers are the neural network, support vector machines, k-nearest neighbors, Gaussian mixture model, naive Bayes, decision tree and RBF (radial basis function) classifiers [119][120][121][122]. Classifier performance depends greatly on the characteristics of the data to be classified. There is no single classifier that works best on all given problems. Determining a suitable classifier for a given problem is however still more an art than a science. In our case, we choose a decision tree classifier. The advantages of the decision tree classifier are: firstly, it is simple to understand and interpret; secondly, every class needs not be tested to arrive at a decision; thirdly, it is easy to extend to more classes [121][122]. In the classification process, the multiple dimensional feature space is split into unique region sequentially. Table 4.5 lists a description of the selected feature vector and the threshold vector based on the experimental results. Figure 4.18 shows the flow chart of the decision tree for surface defect classification process.

Table 4.4: Defect classes and names.

Classes	Defect Names
S1	Pore
S2	Residue Dirt
S3	2D Blemish
S4	Scratch
S5	Gouge
S6	Unknown

Table 4.5: Description of feature vector and related threshold values.

Feature Vector **Z**	Feature Name	Threshold Vector **Th**
Z(1)	Core Area Intensity	Th(1)=950
Z(2)	Bright to Dark Angle Correlation Coefficient	Th(2)=0.9
Z(3)	Dark to Bright Angle Correlation Coefficient	Th(3)=0.9
Z(4)	Major Axis Length/Minimum Width	Th(4)=8
Z(5)	Roundness	Th(5)=0.3
Z(6)	Number of data points satisfy "Dark to Bright Angle Changing Ratio<0.1"	Th(6)=5

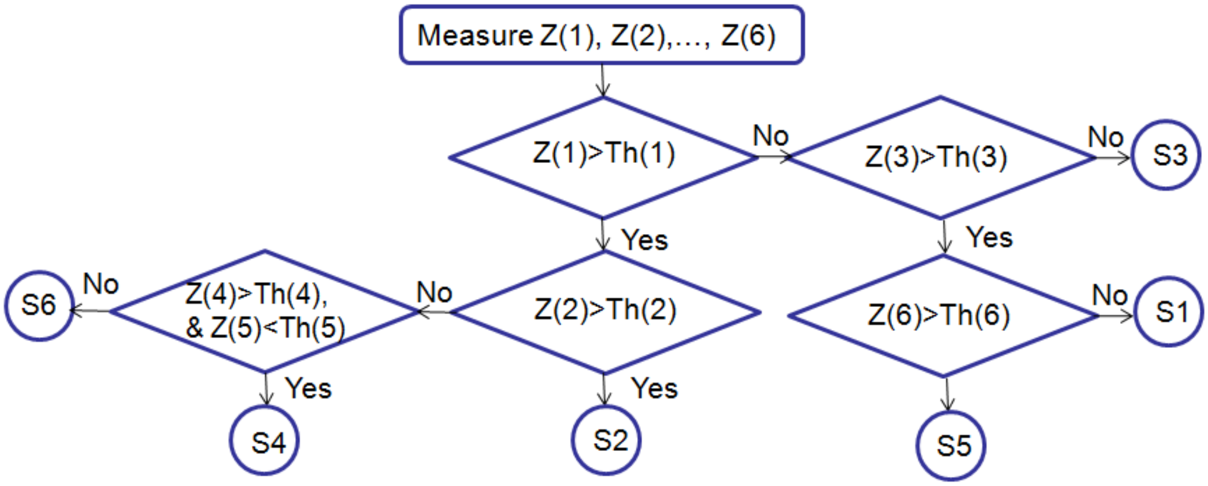

Figure 4.18 Flow chart of decision tree classifier for surface defect classification.

As illustrated in Figure 4.18, the feature vector Z (described in Table 4.5) is first calculated for each anomaly, and then sequential decisions are made to arrive at a defect class. For example, considering anomaly#1 shown in Figure 4.17(a): Z(1), core area intensity is larger than Th(1), background intensity; and Z(2), bright to dark angle correlation coefficient is larger than Th(2), thus anomaly #1 is therefore classified as defect type S2, residue dirt. This is because, if the core portion of an anomaly is brighter than its surrounding background, and the direction of its shadow is highly correlated to the LED illumination angles, it is residue dirt.

Another example, anomaly#3 shown in Figure 4.17(c): Z(1), core area intensity is smaller than Th(1), background intensity; and Z(3), dark to bright angle correlation coefficient is smaller than Th(3), therefore, anomaly #3 is therefore classified as defect type S3, 2D blemish. It is because, if the core portion of an anomaly is darker than the surrounding background, and when the LED illumination direction changes, the image of this anomaly does not change or the change does not related to the LED illumination directions, this anomaly is classified as a 2D blemish. If the core portion of an anomaly is darker than the surrounding background, and the dark to bright angles are highly correlated to the LED illumination angles, this anomaly will be classified as a pore. We will discuss the difference between the defect type pore and gouge later in the case study.

4.2.4 Result Display

Based on the classification method described in the previous section, the result of defect detection and classification for the artificially machined part is shown in Figure 4.19. The location of a defect which means the XY coordinates of the centroid point of this defect, the bounding box and the type (name) of the defect are superimposed on the image and marked with different colors. The defect type of gouge is not on the artificially machined part and will be shown later in the case study section.

In our process, if a defect is classified as porosity, the exact size of the pore is then re-calculated using the Laplacian of Gaussian edge filter [117]. The flow chart of the algorithms is shown in Figure 4.20 (d). Laplacian filter is a derivative filter used to find areas of rapid change (edges) in images. Since the derivative filter is very sensitive to noise, it is common to smooth the image (e.g., using a Gaussian filter) before applying the Laplacian. The combination of Laplacian filter and Gaussian filter is called Laplacian of Gaussian filter.

Here for anomaly #2 (shown in Figure 4.17 (b)), the size of the pore calculated by the Laplacian of Gaussian edge filter is 221 pixels, which is a little bit different from the size of 236 calculated based on the binary image using thresholding method (the features are listed in Table 4.3). The reason for the difference is that the pore size calculated by the thresholding method will be affected by the selection of the threshold value.

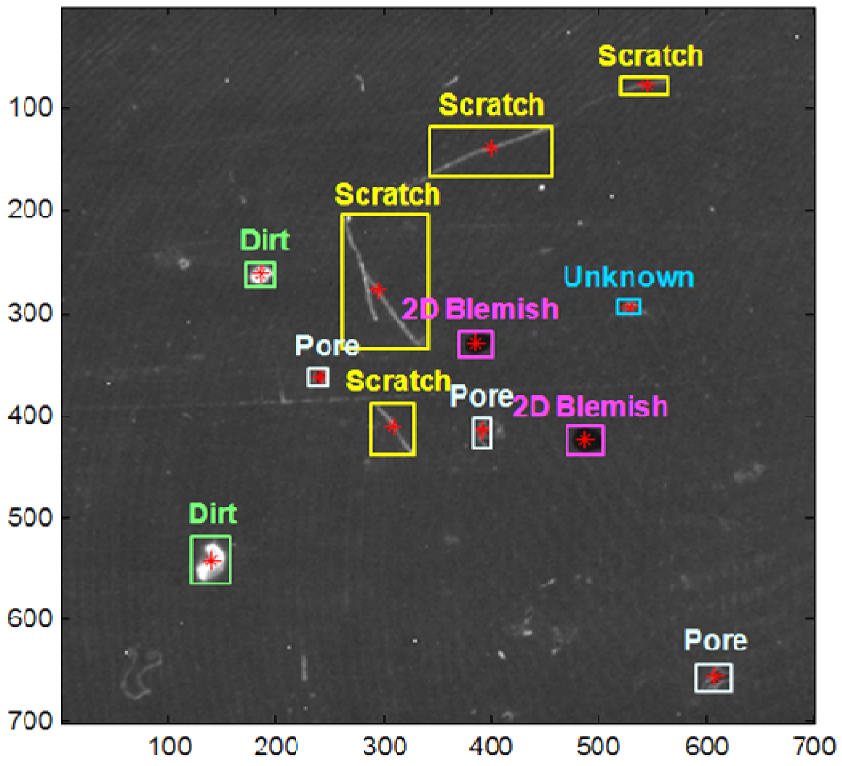

Figure 4.19 Result display of the defects inspected on the artificially machined part.

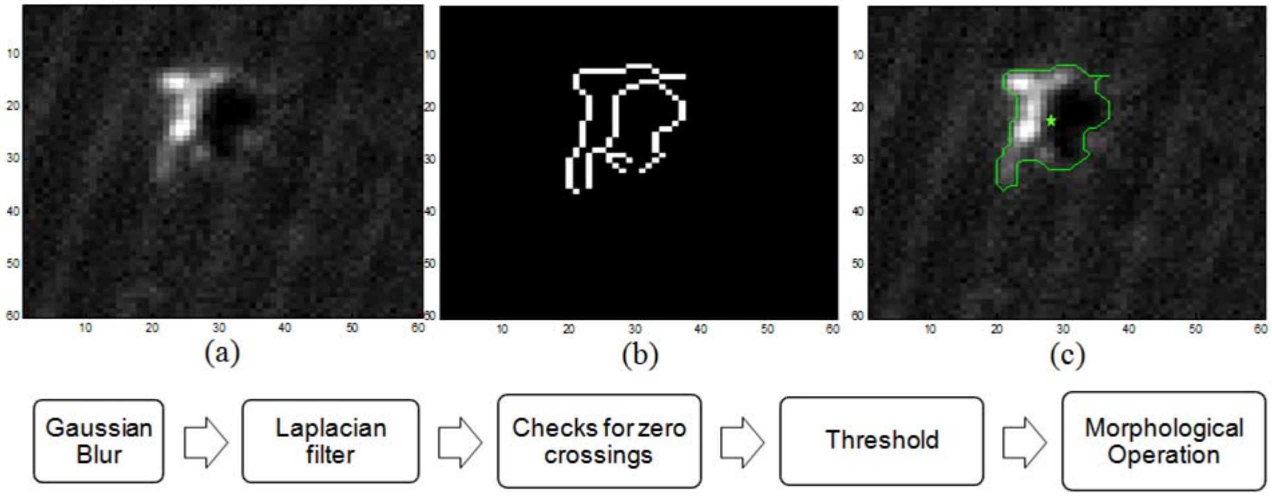

(a) (b) (c)

(d)

Figure 4.20 (a) An image of a pore on the artificially machined surface (anomaly #2), (b) binary image where the white pixels show the edge points of the pore detected by the Laplacian of Gaussian edge filter, (c) the boundary and the centroid point of the pore, (d) the flow chart of the algorithms of Laplacian of Gaussian edge filter.

4.3 Case Studies of Automotive Parts

4.3.1 Case Study 1: Transmission Pump Surface

To test the performance of the surface defect detection and classification system on an actual powertrain machined part surface, all the image processing steps are the same as those used for inspecting the artificially machined surface. However an actual part contains intentional surface features (larger than the defect dimensions) which are unnecessary information for machined surface defect detection and will confuse the defect segmentation results thus should be removed before the detecting process.

We developed an algorithm to automatically extract the feature-free surface using morphological operations based on the gray image of the target surface. By doing this, we don't need any prior knowledge about the intentional features that may be offered by a template. The gray image of the target surface is captured based on the on-axis diffuse illumination. The assumption for the algorithm is that the contrast between the gray level of the machined surface and the un-machined surface is large, which is reasonable. The morphological operations are: (a) threshold the image, (b) label the connected groups on the binary image, (c) select the largest group, (d) fill in the holes which are smaller than the smallest intentional feature size inside the selected group. By doing this, the pixels not of interest will be removed.

Figure 4.21 (a) shows the gray image of a selected part of a transmission pump surface illuminated by the on-axis diffuse light source and Figure 4.21 (b) is a binarized image showing the feature-free surface exacted by the morphological operations. Figure 4.22 (a) shows an image illuminated by the directional LED light source, and Figure 4.22 (b) shows the feature-free surface based on the binary mask shown in Figure 4.21 (b),

Figure 4.22 (c) shows that a defect (a pore) was detected on the transmission pump surface.

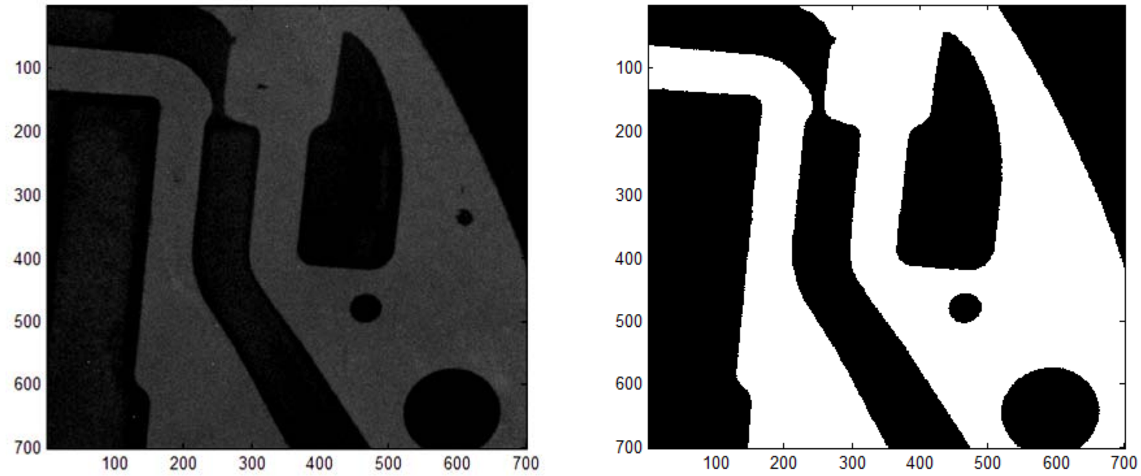

(a) (b)

Figure 4.21 (a) Gray image (illuminated by the on-axis diffuse light source) of a selected part of a transmission pump, (b) binary image of the feature-free surface.

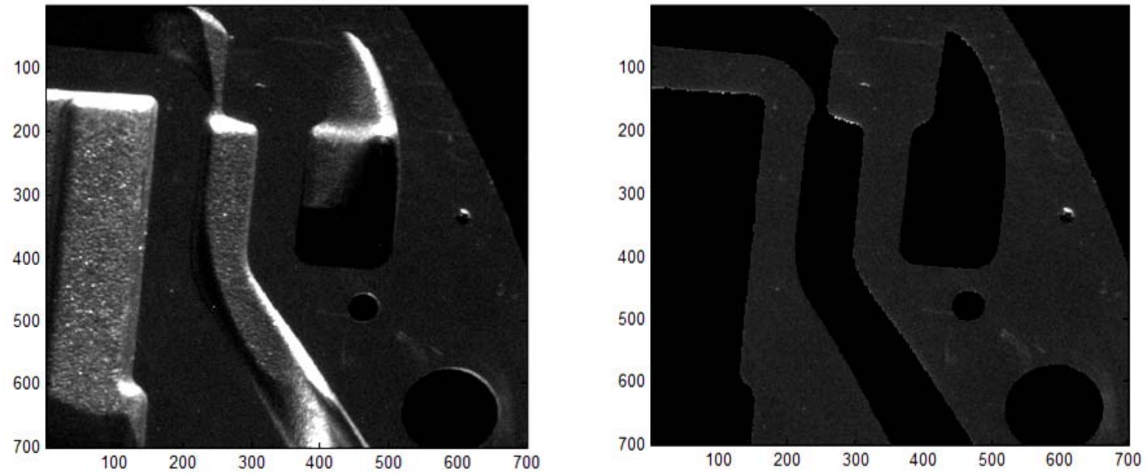

(a) (b)

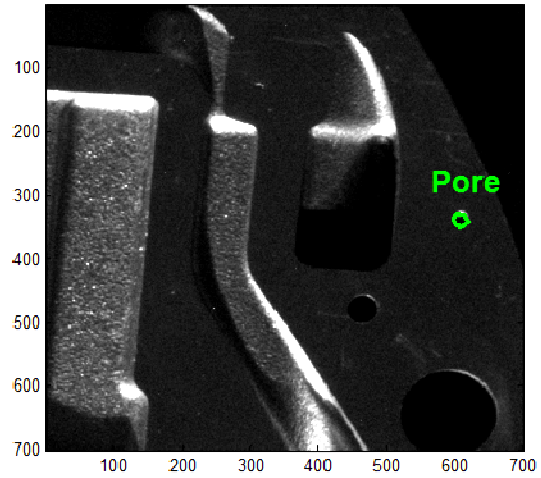

(c)

Figure 4.22 (a) Gray image illuminated by the directional LED light source, (b) feature-free surface of the image in (a), (c) defect detected (a pore) on the transmission pump surface.

4.3.2 Case Study 2: Cylinder Head Surface

Normally in the inspection process, a user-defined region will be selected to perform the inspection, and these regions will be selected near to the edges of the surface that may cause serious leaking problem. We can also inspect the whole surface. In case study 2, a cylinder head surface is inspected using the full field of view of the system. Figure 4.23 shows the inspection result. In order to display the defect clearly, we enlarged the region near the defect shown in Figure 4.23 (c).

In this case study, the defect type is a gouge. In Table 4.5, we defined the feature vector, where Z(6) is the number of data points satisfy "dark to bright angle changing ratio<0.1”, and a threshold Th(6)=5 is selected based on our experiences. Here the dark to bright angle changing ratio is calculated by the difference between two consecutive dark to bright angles divided by the mean value of these two angles. Figure 4.24 (b) shows the dark to bright angle changing ratio of this defect (a gouge) on the cylinder head, and we can see that 7 out of 11 data points are under 0.1. Compared to the defect type of a pore, as shown in Figure 4.24 (d), the only difference between the pore and gouge is that the pore only has 2 out of 10 data points satisfy "dark to bright angle changing ratio <0.1". The reason for this difference is that, the edge of a gouge is less irregular compared to a pore (close to a rectangle shape), therefore, when the LED illumination angle changes within some range, the shining edge of a gouge may not change. But for a pore, the edges are close to a circular shape, the shining edge will rotate with the changing LED illumination angle.

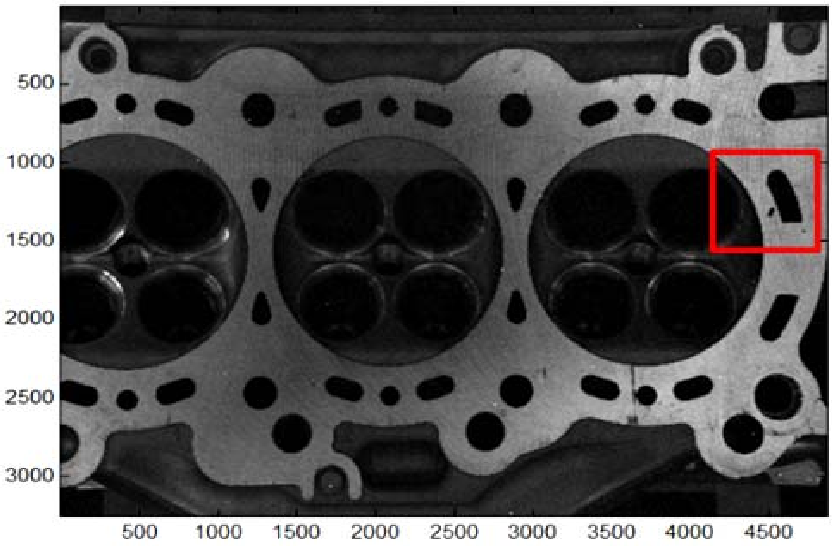

(a)

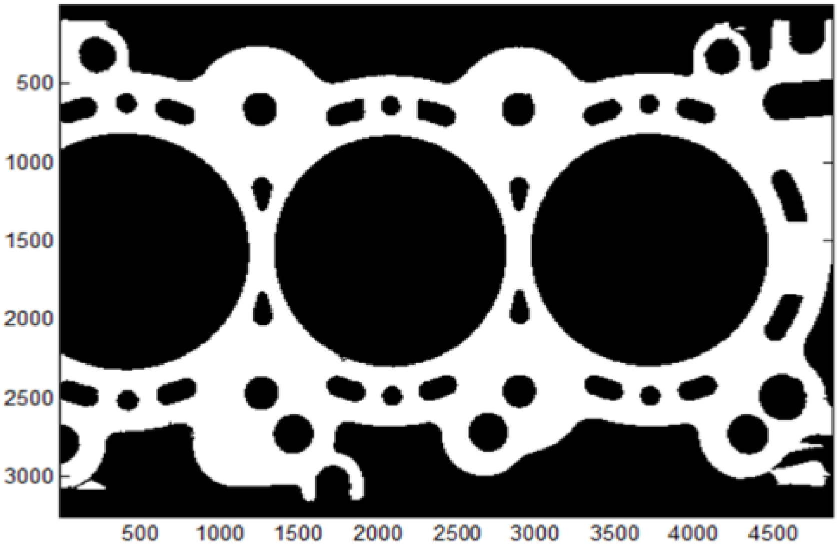

(b)

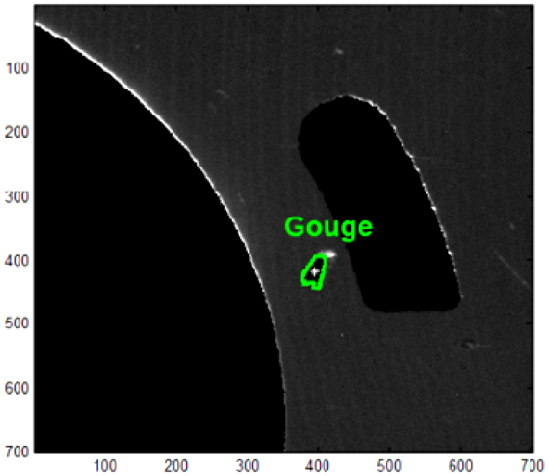

(c)

Figure 4.23 (a) Gray image (illuminated by the on-axis diffuse light source) of a cylinder head surface, (b) feature-free surface of the cylinder head, (c) defect detected (a gouge) on the cylinder head surface.

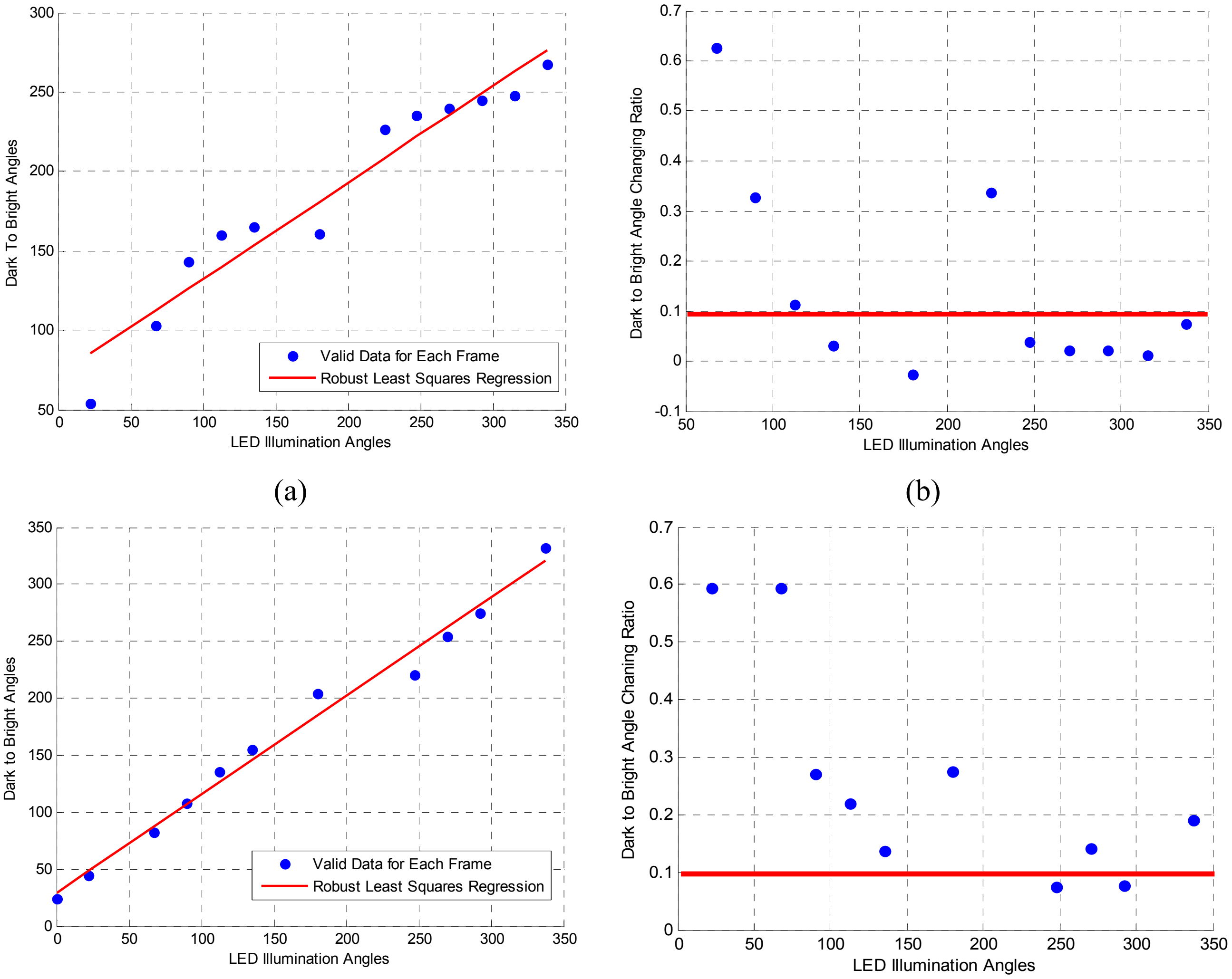

(a) (b)

(c) (d)

Figure 4.24 (a) LED illumination angles versus the dark to bright angles of a gouge on the cylinder head, (b) the scatter plot of the dark to bright angle changing ratio of (a), (c) LED illumination angles versus the dark to bright angles of a pore on the artificially machined part, (d) the scatter plot of the dark to bright angle changing ratio of (c).

4.4 Conclusions

In this chapter, a novel automated defect detection and classification system has been designed and constructed to extract surface abnormal features and classify them into different defect types. This system is a machine vision system using multiple directional illuminations to produce image series providing robust three-dimensional defect information. The image processing algorithms were developed to realize 5 types of surface defect (pore, 2D blemish, residue dirt, scratch, and gouge) detection and classification. In the previous sections, the steps of image processing: (1) image acquisition and contrast enhancement (2) defect segmentation and feature extraction (3) defect classification, were introduced in detail. We tested this system on an artificially machined surface and two actual automotive machined part surfaces: a transmission pump surface and a cylinder head surface. The experimental results showed that the microscopic surface defects which have the minimum dimension larger than 300 micron can be accurately detected and assigned to a certain surface defect class.

CHAPTER 5

CONCLUSIONS AND FUTURE WORK

5.1 Conclusions

This doctoral research is focused on developing image processing method to reliably extract multiple-scale 3D surface texture features from a large field of view 3D surface height map measured by an optical holographic interferometer. And these features were then applied to characterize 3D surface functional performances and detect errors in the machining process. We also designed and constructed an automated machine vision system to extract the abnormal surface features and classify these anomalies into certain defect types that are problematic to the manufacturing process.

First, we developed an improved Gaussian filter to accurately extract 3D surface waviness and applied the waviness feature of machined workpiece to assess severe tool wear. Compared to the standard Gaussian filter, the improved Gaussian filter was specially designed to improve the filter performance when applying on an engineering surface height map which has lots of sharp noises and large distortion shape. In this work, in addition to 3D surface waviness feature, other two 3D surface texture parameters of machined workpiece (image intensity histogram distribution and 3D peak-to-valley height) were also studied and applied to assess tool wear. Experimental results on aluminum and compacted graphite iron workpieces showed that these 3D surface texture parameters can all be used to detect the onset of severe tool wear.

Second, a method of using 2D wavelet to decompose a large field of view 3D engineering surface into multiple-scale frequency bands was developed. Compared to the work in the first part, the wavelet based method can decompose a surface into finer frequency bands. In this work, we developed a two-channel filter bank diagram for multiple-scale 3D surface decomposition. The two-channel filter bank diagram enables the separate filtering of successive profile in the row direction, followed by the same operation in the column direction, thus greatly simplifies the implementation and brings computational efficiency. A three-dimensional cylinder head surface height map measured using the holographic interferometer was used for the demonstration. During the decomposition process for an engineering surface, two important issues: the elimination of the border distortion and the transformation between the scale of the wavelet at each decomposition level and its physical dimension were also studied. Following this, four automotive case studies were used to demonstrate the application of using multi-scale 3D surface features to predict surface functional performances and detect issues in the machining process. These case studies included abrupt broken tool detection, chatter detection, mating/sealing surface leak paths identification, and surface non-clean up region detection. These case studies showed that the wavelet transform decomposition method is a very good tool to rapidly assess surface functions and detect machining faults based on the comprehensive surface information.

Finally, a novel automated surface defect detection and classification system has been designed and constructed. This system is based on multiple directional illuminations to produce information set providing robust 3D surface defect feature information. Related image processing algorithms were developed to detect and classify 5 types of surface defect (pore, 2D blemish, residue dirt, scratch, and gouge) which are commonly found on the automotive powertrain mating/sealing surfaces. The steps of image processing: (1) image acquisition and contrast enhancement (2) defect segmentation and feature extraction (3) defect classification, were clearly presented. We demonstrated our technique on an artificially machined surface and two actual automotive machined part surfaces: a transmission pump surface and a cylinder head surface. The experimental results showed that the microscopic surface defects which have the minimum dimension larger than 300 micron can be accurately detected and assigned to a surface defect class. The breadboard system is a successful step toward the implementation of a product to implement 100% inline inspection of surface defects in a production machining line.

5.2 Future Work

A number of future research topics are recommended following the studies in this dissertation:

(1) A specially designed wavelet, e.g., a wavelet formed by the lifting algorithm, can be developed to better decompose a 3D engineering surface into multiple-scale subsurfaces. Different frequency components of the surface can be separated, extracted and then reconstructed according to the intended requirements of the surface functional analysis. As introduced in [19][91], the lifting wavelet representation is to initially decompose an original surface into a sequence of subsets, without an assessment of the frequency content of the original signal. Next, different frequency components can be interrogated via a flexible transmission bank according to the intended functional inferences which need to be drawn from it. Finally, the required surfaces can be

reconstructed in the spatial domain. This future work requires a solid mathematical background and familiarity to the manufacturing process.

(2) In the future work, people can think about how to better predict a product's functionality with the dimensional and surface characteristics information. A better measurement scheme which allow the engineers to measure less characteristics on one part while taking more product samples from the production line can be studied. How to represent the complex surface data in a consistent way with other quality features while not loosing much information poses a big challenge, especially when all the quality characteristics are needed as the inputs in the prediction model. Moreover, other non-dimensional, non-surface quality characteristics, e.g. material properties, defects and residual stresses, can also be integrated into the surface functionality characterization.

(3) Inspirited by paper [104], the surface defect detection algorithm can be improved by combining the wavelet technique. A multiresolution approach can be used for the inspection of local defects embedded in the surface with strong tooling marks. By properly selecting the smooth subimage or the combination of detail subimages at different resolution levels for image reconstruction, the surface background containing tooling marks can be effectively removed and only the local anomalies are preserved in the restored image. Therefore, the surface defects extraction algorithm can be simpler, faster and more robust.

(4) The applications of the machine vision inspection system can be extended to detect and classify defects on many types of surfaces, such as fabric, wood, sand paper, and so on.

5.3 Contributions

The main contributions of this dissertation are summarized as follows:

I. Scientific Contributions:

(1) Developed an improved Gaussian filter technique to accurately extract 3D surface waviness from large field of view 3D engineering surface height map which has large form distortion and contains lots of sharp peaks/valleys/noise.

(2) Developed a two-channel filter bank algorithm diagram for applying 2D wavelet on multiple-scale 3D surface decomposition. Exploited a simple but effective border distortion elimination method when applying 2D wavelet to decompose a 3D engineering surface. Quantified the transformation between the wavelet scale and its physical dimension.

(3) Designed and constructed a novel, automated and fast machine vision system to detect and classify 5 types of microscopic surface defects commonly found on the mating/sealing surface. This system is a single camera system with 16 LED blocks illuminating the target surface from multiple directions sequentially.

(4) Improved the image histogram equalization algorithm by choosing a reference image and enhancing the contrast of other images by transforming the intensity values of the input image so that the histogram of the output image approximately matches the distribution of the reference image.

(5) Enhanced the global thresholding image segmentation algorithm by adding an edge filter and considering only the pixels near the edges between the objects

and background. This method makes the intensity distribution of the image less dependent on the relative sizes of the objects and the image background.

II. Engineering Contributions:

(1) Presented a new way to detect severe tool wear based on the 3D surface waviness feature of the workpiece; the experimental results of different cutter types, workpiece materials and cutting conditions showed that the 3D surface waviness feature is a good indicator for detecting severe tool wear.

(2) Defined some surface height and energy features from multiple-scale subsurfaces and applied them to several automotive case studies. These case studies demonstrated that the different-scale surface features can be used to predict various surface functional performances and detect machining faults.

(3) Tested the “breadboard” surface defect detection and classification system on an artificially machined surface and two actual automotive parts. The experimental results showed that this system has the ability to detect and distinguish 2D or 3D microscopic surface defects which are problematic to the powertrain manufacturing.

BIBLIOGRAPHY

[1] Whitehouse, D. J., 1994, "*Handbook of Surface Metrology*," Bristol, UK: Institute of Physics Publishing.

[2] ASME B46.1, 1995, "Surface texture — Surface Roughness, Waviness, and Lay".

[3] Raja, J., Muralikrishnan, B., and Fu, S., 2002, ''Recent Advances in Separation of Roughness, Waviness and Form,'' Precis. Eng., **26** (2).

[4] Whitehouse, D.J., 1967-1968, "Improved type of wavefilter for use in surface-finish measurement," Proc. Inst. Mech. Eng. **182**, 306-318.

[5] Raja, J., Radhakrishnan, V., 1979, "Digital filtering of surface profiles," Wear, **57**, 147-155.

[6] ISO 11562, 1996, "Geometrical product specification (GPS) - surface texture: profile method—metrological characteristics of phase correct filters," Geneva: International Organization for Standardization.

[7] Raja, J., Radhakrishnan, V., 1979, "Filtering of surface profiles using fast Fourier transform," Int. J. Mach. Tool. Des. Res., **19**, 133-141.

[8] Krystek, M., 1996, "A fast Gauss filtering algorithm for roughness measurements," Prec. Eng., **19**, 198-200.

[9] Yuan, Y.B., Qiang, X.F., Song, J.F., Vorburger, T.V., 2000, "A fast algorithm for determining the Gaussian filtered mean line in surface metrology," Prec. Eng., **24**, 62-69.

[10] Krystek, M., 2000, "Discrete linear profile filters," Proceedings of the Xth International Colloquium on Surfaces. Chemnitz University of Technology, Chemnitz, 145-152.

[11] Krystek, M., 1996, "Form filtering by splines," Measurement, **18**, 9-15.

[12] Srinivasan, V., "Discrete morphological filters for metrology, 1988, " Proceedings of the 6th IMEKO ISMQC Symposium on Metrology for Quality Control in Production. TU Wien, Austria.

[13] Scott, P.J., 2000, "Scale-space techniques," Proceedings of the Xth International Colloquium on Surfaces. Chemintz University of Technology, Chemnitz, p153-161.

[14] Chen, X., Raja, J., 1995, "Simanapalli S. Multi-scale analysis of engineering surface," Int. J. Mach. Tools Manufact., **35(2),** 231-238.

[15] Liu, X., Raja, J., 1996, "Analyzing engineering surface using wavelet filter," Proceedings of the SPIE, Vol. **2825**.

[16] Mallat, S., 1989, "A theory for multi-resolution signal decomposition: the wavelet representation," IEEE Trans. Pattern Anal. Mach. Intell., **11(7)**, 674-693.

[17] Vetterli, M., Herley, C., 1992, "Wavelets and filter banks: theory and design," IEEE Trans. Signal Proc., **40(9)**, 2207-2232.

[18] Sweldens, W., 1996, "The lifting scheme: a custom-design construction of biorthogonal wavelets," Appl. Comput. Harmon. Anal., **3(2)**, 186-200.

[19] Jiang, X.Q., Blunt, L., Stout, K.J., 2000, "Development of a lifting wavelet representation for surface characterization," Proc. R. Soc. Lond. A., **456**, 2283-2313.

[20] Whitehouse, D.J., 1982 "The Parameter Rash – is there a cure," Wear, Vol. **83**, 75-78.

[21] Griffiths B., 2001, *"Manufacturing surface technology: surface integrity and functional performance*," Taylor and Frances.

[22] Wyatt, J. E., Smith, G. T., Berry, J. T., 2006, "Surface characterization and the functionality of mating parts," ASME International Manufacturing Science and Engineering Conference (MSEC), pp 867-875.

[23] Blunt, L., Stout K,J., 2000, *Three-dimensional Surface Topography*, Penton Press, London.

[24] Stout, K.J., 2000, *Development of methods for characterisation of roughness in three dimensions*, Butterworth Heinemann.

[25] Bengtsson, A., Ronnberg, A., 1984, "Wide range three-dimensional roughness measuring system," Prec. Eng., **6(3)**, 141-147.

[26] Teague, E. C., Scire, F. E., Baker, S. M., Jensen, S. W., 1982, "Three-dimensional stylus protilometry," Wear, **83**, 1-12.

[27] Lewis, J. R. T., Sopwith, T., 1986, "Three-dimensional surface measurement by microcomputer," Image mien. Complcl., **4(3)**, 159-166.

[28] Lange, S. R., Bhushan, B., 1988, "Use of two- and three-dimensional non-contact surface profile for tribology applications," Surf. Topogr., **I(3)**, 277-289.

[29] Ldrus, N., 1981, "An integrated digital system for three-dimensional surface scanning," Prec. Eng., **3(3)**, 37-43.

[30] Contet, P., Ville, J. F., 1995, "Surfascan 3D — An industrial 3D surface texture characterisation instrument," Int. J. Mach. Tools Manufact., **35**, 151-156.

[31] Lu, S., Gao,Y., Xie, T., Xie, F., Jiang, X. Q., Li, Z., Wang, F., 2001, "A novel contact/non-contact hybrid measurement system for surface topography characterization," Int. J. Mach. Tools Manufact., **41**, 2001-2009.

[32] Thierry, Z., Heinz, H., 2004, "Applied multifocus 3D microscopy," Two- and Three-Dimensional Vision Systems for Inspection, Control, and Metrology, Proceedings of SPIE, Bellingham, WA, Vol. **5265**, 134-144.

[33] Xie, F., Xiao, S., Blunt, L., Zeng, W., Jiang, X., 2009, "Automated bullet-identification system based on surface topography techniques," Wear, **266**, 518-522.

[34] Dong, W.P., Sullivan, P.J., and Stout, K.J., 1992, “Comprehensive Study of Parameters for Characterizing 3D Surface Topography I: Some Inherent Properties of Parameter Variation,” Wear, **159**, 161-171.

[35] Dong,W.P., Sullivan, P.J., and Stout, K.J., 1993, “Comprehensive Study of Parameters for Characterizing 3D Surface Topography II: Statistical Properties of Parameter Variation,” Wear, **167**, 9-21.

[36] Dong,W.P., Sullivan, P.J., and Stout, K.J., 1994, “Comprehensive Study of Parameters for Characterizing 3D Surface Topography III: Parameters for Characterizing Amplitude and Some Functional Properties,” Wear, **178**, 29-43.

[37] Dong,W.P., Sullivan, P.J., and Stout, K.J., 1994, “Comprehensive Study of Parameters for Characterizing 3D Surface Topography IV: Parameters for Characterizing Spatial and Hybrid Properties,” Wear, **178**, 45-60.

[38] Lonardo, P. M., Trumpold, H., De Chiffre, L., 1996, "Progress in 3D Surface Microtopography Characterization," CIRP Annals Manufact. Tech., **45**, 589-598.

[39] Jiang, X. Q., Blunt, L., Stout, K. J., 1999, "Three-dimensional surface characterization for orthopaedic joint prostheses," Proceedings of the Institution of Mechanical Engineers, Part H: Journal of Engineering in Medicine, **213**, 49-68.

[40] Josso, B., Burton, D. R., Lalor, M. J., 2002, "Frequency normalised wavelet transform for surface roughness analysis and characterisation," Wear, **252**, 491-500.

[41] Myshkin, N. K., Grigoriev, A.Ya., Chizhik, S.A., Choi, K.Y., Petrokovets, M.I., 2003, "Surface roughness and texture analysis in microscale," Wear, **254**, 1001-1009.

[42] Yuan, C., Peng, Z., Yan, X., 2005, "Surface Characterization Using Wavelet Theory and Confocal Laser Scanning Microscopy," J. Tribology, **127**, 394-404.

[43] http://coherix.com/automotive.

[44] Kurada,S., and Bradley,C., 1997, “A Machine Vision System for Tool Wear Assessment,” Tribology International, **30**(4), pp. 295–304.

[45] Lanzetta,M., 2001, “A New Flexible High-Resolution Vision Sensor for Tool Condition Monitoring,” J. Materials Processing Technology, **119**, 72-82.

[46] Jurkovic,J., Korosec,M., Kopac,J., 2005, “New Approach in Tool Wear Measuring Technique using CCD Vision System,” International Journal of Machine Tools & Manufacture, **45**, 1023–1030.

[47] Choi, Y., and Chung, S., 2006, “Monitoring of Micro-Drill Wear by Using the Machine Vision System,” Trans. NAMRI/SME, **34**, pp. 143–150.

[48] Dimla Snr, D.E., 2000, “Sensor Signals for Tool-Wear Monitoring in Metal Cutting Operations: A Review of Methods,” International Journal of Machine Tools and Manufacture, **40**, 1073–1098.

[49] Sarhan, A., Sayed, R., Nassr, A.A., and El-Zahry, R.M., 2001, “Interrelationship between Cutting Force Variation and Tool Wear in End-milling,” J. Materials

Processing Technology, **109**, 229–235.

[50] Risbood, K.A., Dixit, U.S., Sahasrabudhe, A.D., 2003, "Prediction of Surface Roughness and Dimensional Deviation by Measuring Cutting Forces and Vibrations in Turning Process," J. Materials Processing Technology, **132**, 203–214.

[51] Qin,N., Pei,Z.J., Treadwell,C., Guo,D.M., 2009, "Physics-Based Predictive Cutting Force Model in Ultrasonic- Vibration-Assisted Grinding for Titanium Drilling," ASME, J. Manufacturing Science and Engineering, **131**, 041011-1-9.

[52] Toh, C.K., 2004, "Vibration Analysis in High Speed Rough and Finish Milling Hardened Steel," J. Sound & Vibration, **278**, 101–115.

[53] Suprock, C., and Roth, J. T., 2006, "Directionally Independent Failure Prediction of End Mill Cutting Tools: An Investigation of Noise Reduction Using Higher Dimensional Real Fourier Analysis," ASME Paper No. IMECE2006-14968.

[54] Li, X.L., 2002, "A Brief Review: Acoustic Emission Method for Tool Wear Monitoring During Turning," International Journal of Machine Tools & Manufacture, **42**, 157–165.

[55] Chiou, R.Y., and Liang, S.Y., 2000, "Analysis of Acoustic Emission in Chatter Vibration with Tool Wear Effect in Turning," International Journal of Machine Tools & Manufacture, **40**, 927–941.

[56] Gong,W., Li,W., Shirakashi,T., and Obikawa,T., 2004, "An Active Method of Monitoring Tool Wear Stages by Impact Diagnostic Excitation," International Journal of Machine Tools & Manufacture, **44**, 847–854.

[57] Suprock,C.A., Roth,J.T., 2008, "Directionally Independent Failure Prediction of End-Milling Tools by Tracking Increasing Chaotic Noise at the Machining Frequencies Due to Wear," ASME, J. Manufacturing Science and Engineering, **130**, 031006-1-9.

[58] Damodaraswamy,S., and Raman,S., 1991, "Texture Analysis using Computer Vision", Computers in Industry, **16**, pp. 25–34.

[59] Bradley,C., and Wong,Y.S., 2001, "Surface Texture Indicators of Tool Wear - A Machine Vision Approach," International Journal of Advanced Manufacturing Technology, **17**, 435–443.

[60] Dianne, P., 1990, "Robust Regression Computation Using Iteratively Reweighted Least-Squares," Society for Industrial and Applied Mathematics, Vol. **11**, No. **3**, pp. 466-480.

[61] Lancaster, P., Salkauskas, K., 1986, *Curve and surface fitting*, Academic Press.

[62] Sullivan, P.J., Evans, C., 1992, "Improving the robustness of curve fitting in figure and finish metrology," Optical Fabrication and Testing Workshop.

[63] Draper, N.R., Smith, H., 1998, *Applied Regression Analysis*, Wiley Interscience.

[64] Tukey, J.W., 1974, "Nonlinear (nonsuperposable) methods for smoothing data," in Conf. Rec., EASCON, pp.673.

[65] Pratt, W. K., 1978, *Digital Image Processing*. New York: Wiley.

[66] Hwang, H., Haddad, R. A., 1995, "Adaptive Median Filters: New Algorithms and Results," IEEE Trans. on Image Processing, vol.**4**, no.**4**, pp.499-502.

[67] Kong, H., Guan, L., 1998, "A noise exclusive adaptive filtering framework for removing impulse noise in digital images," IEEE Trans. Circuits Syst. II., vol.**453**, pp. 422–428.

[68] Xu, X., Miller, E. L., "Dongbin Chen and Mansoor Sarhadi, 2004, "Adaptive Two-Pass Rank Order Filter to Remove Impulse Noise in Highly Corrupted Images", IEEE Transactions on Image Processing, Vol.**13**, No. **2**, pp.238 – 247.

[69] Nallaperumal, K., Varghese, J., 2006, "Adaptive threshold based switching median filter for highly corrupted images", in proc. of CSIIEEE First Intnl. Conf. EAIT 2006, Calcutta, India, Elsevier, pp. 103-106.

[70] Nallaperumal, K., Varghese, J., 2006, "Selective Switching Median Filter for the Removal of Salt & Pepper Impulse Noise", in proc. of IEEE WOCN 2006, Bangalore, India, pp. 11-13.

[71] Zhou, Y., Tang, Q., Jin, W. 2008, "A fast adaptive switching median filter based on measure-integral," Proceedings of the 7th world congress on intelligent control and automation, June 25-27, Chongqing, China, pp.6760-6763.

[72] Liu, Y., Liu, C., Wang, D., 2009, "A 1D time-varying median filter for seismic random, spike-like noise elimination," Geophysics, **74**, v17-v24.

[73] Huynh-Thu, Q., Ghanbari, M., 2008, "Scope of validity of PSNR in image/video quality assessment," Electronics Letters 44: 800–801.

[74] Mehta, N.K., Pandey, P.C., 1983, "An Investigation of Tool Wear and the Vibration Spectrum in Milling," Wear, **91**, 219-234.

[75] Bracewell, R. N., 2000, *The Fourier Transform and Its Applications*, Boston: McGraw-Hill.

[76] Boashash, B., 2003, *Time-Frequency Signal Analysis and Processing: A Comprehensive Reference*, Oxford: Elsevier Science.

[77] Portnoff, M. R., 1980, "Time-frequency representation of digital signals and systems based on short-time Fourier analysis," IEEE Trans. on acoustics, speech and signal processing, **28**, 55-69.

[78] Nawab, S. H., Quatieri, T. F., 1987, "Short-time Fourier transform," Prentice-Hall Signal Processing Series archive Advanced topics in signal processing book contents, 289-337.

[79] Haar, A., 1910, "The theory of orthogonal function systems", Mathematical annals, **69**, pp 331-371.

[80] Mallat, S., 1999, "*A Wavelet Tour of Signal Processing*", Second edition, Academic Press.

[81] Daubechies, I., 1988, “Orthonormal Bases of Compactly Supported Wavelets”, Commun. Pure Appl. Math., **41**, pp. 909-996.

[82] Daubechies, I., 1992, “*Ten lectures on wavelets*,” Philadelphia.

[83] Strang, G., and Nguyen, T. Q., 1996, “*Wavelets and Filter Banks*,” Cambridge Press, Wellesley.

[84] Liu, X., Raja, J., Sannareddy, H., 1995, “Assessment of plateau honed surface texture using wavelet transform,” Proc. ASPE, **14**, 672-675.

[85] Fu,S., Muralikrishnan, B., Raja.J., 2003, “Engineering Surface Analysis with Different Wavelet Bases,” ASME, J. Manufacturing Science and Engineering, **125**, 844-852.

[86] Josso, B., Burton, D.R., Lalor, M. J., 2002, “Frequency normalized wavelet transform for surface roughness analysis and characterization,” Wear, **252**, 491-500.

[87] Lin, J., and Zuo, M. J., 2006, “Wavelet filter-based weak signature detection method and its application on rolling element bearing prognostics,” Journal of Sound and Vibration, **289**(4-5), pp. 1066-1090.

[88] Olortegui-Yume,J.A., Yoon,M.C., Kwon,P.Y., 2008, “Crater wear patterns and evolution on multi-layer coated carbides using the wavelet transform,” ASME International Manufacturing Science and Engineering Conference (MSEC), pp 437-445.

[89] Li,J., Shi, J.J., Chang, T.S., 2007, “On-line seam detection in rolling processes using snake projection and discrete wavelet transform,” J. Manuf. Sci. Eng., Vol. **129**, 926-933.

[90] Bruzzone, A.A.G., Montanaro, J.S. , Ferrando, A., Lonardo, P.M., 2004, “Wavelet analysis for surface characterization: An Experimental Assessment,” CIRP Annals , **53**, 479-482.

[91] Jiang, X. Q., Blunt, L., Stout, K. J., 2001, “Lifting wavelet for three-dimensional surface analysis,” Int. J. of Machine Tools & Manufacture, **41**, 2163-2169.

[92] Zeng, W., Jiang, X., Scott,P., 2005, “Metrological characteristics of dual-tree complex wavelet transform for surface analysis,” Measurement Science and Technology, **16** , 1410-1417.

[93] ISO catalog, ISO 10126-1:1991.

[94] Bickford, J. H., 1995, *An Introduction to the Design and Behavior of Bolted Joints*, 3rd ed., Marcel Dekker.

[95] Latte, D. J., Rossi, C., 1995, "High Temperature Behavior of Compressed Fiber Gasket Materials, and an Alternative Approach to the Prediction of Gasket Life," FSA presented Paper, p16.

[96] Malburg, M. C., 2003, "Suface profile analysisi for conformable interfaces," ASME J. Manufacturing science and engineering, **125**, 624-627.

[97] Anderson, R. C., 1983, “Inspection of metals, Volume I: Visual inspection,” American Society of Metals International, Metals Park, Ohio, 68-69.

[98] Kumar, A., 2008, “Computer-vision-based fabric defect detection: a survey,” IEEE Trans. Ind. Elec. **55**, 348-363.

[99] Mahalanobis, A., Singh, H., 1994, “Application of correlation filters for texture recognition,” Appl. Opt., Vol. **33**, No. **11**, 2173-2179.

[100] Liu, Z. Q., Madiraju, V. R., 1996, “Covariance-based approach to texture processing,” Appl. Opt., Vol. **35**, No.**5**, 848-853.

[101] Kumar, A., Pang, G. K. H., 2002, “Defect detection in textured materials using Gabor filters,” IEEE Trans. Ind. Appl. **38**, 425-440.

[102] Escofet, J., Navarro, R. B., Millan, M. S., Pladellorens, J. M., 1998, “Detection of local defects in textile webs using Gabor filters,” Opt. Eng. **37**(8), 2297-2307.

[103] Rallo, M., Millan, M. S., Escofet, J., 2007, “Referenceless segmentation of flaws in woven fabrics,” Appl. Opt., Vol. **46**, No. **27**, 6688-6699.

[104] Tsai, D. M., Chiang, C. H., 2003, “Automatic band selection for wavelet reconstruction in the application of defect detection,” Image and Vision Computing, **21**, 413-431.

[105] Hu, C. H., Liang, H. P., 2008, “Wood surface texture inspection using automatic selection band for wavelet reconstruction,” Proc. of SPIE Vol.**7130**, 713038.

[106] Beyerer, J., 1995, “Model based analysis of grooved textures with application to automated inspection of machined surfaces,” Measurement, **15**, 189-199.

[107] Mahon, J., Harris, N., Vernon, D., 1989, “Automated visual inspection of solder past deposition on surface mount technology PCBs,” Comput Ind., **12**, 3-142.

[108] Nayar, S. K., Sanderson, A. C., Weiss, L. E., Simon, D. A., 1990, “Specular surface inspection using structured highlight and Gaussian images,” IEEE Trans. Rob. Autom., **6**(2), 208-218.

[109] Ramana, K. V., Ramamoorthy, B., 1996, “Statistical methods to compare the texture features of machined surfaces,” Pattern Recogn. **29**, 1447–1459.

[110] Steiner, D., Katz, R., 2007, “Measurement techniques for the inspection of porosity flaws on the machined surfaces,” J. Comput. Inf. Sci. Eng. **7**, 85-94.

[111] Chantler, M. J., 1995, “Why illuminant direction is fundamental to texture analysis,” IEEE Proc. Vision, Image and Signal Processing, Vol. **142**, 199-206.

[112] Racky, J., Pandit, M., 1999, “Active illumination for the segmentation of surface deformations,” in ICIP (1), IEEE, 41-45.

[113] Lindner, C., Arigita, J., Leon, F. P., 2005, “Illumination-based segmentation of structured surfaces in automated visual inspection,” Proc. of SPIE, Vol. **5856**, 99-108.

[114] Lindner, C., Leon, F. P., 2006, “Reflection-based surface segmentation using active illumination,” in Proc. IEEE Instrum. Meas. Technol. Conf., 157-162.

[115] Leung, T., Malik, J., 2001, “Representing and recognizing the visual appearance of materials using three-dimensional textons,” J. Computer Vision, **43**, 29-44.

[116] Gonzalez, R. C., Woods, R. E., 2002, *Digital Image Processing, Second Edition*, by Prentice Hall.

[117] Gonzalez, R. C., Woods, R. E., Eddins, S. L., 2009, *Digital Image Processing using Matlab, Second Edition*, by Gatesmark Publishing.

[118] Canny, J., 1986, “A computational approach to edge detection,” IEEE Trans. Patt. Ana. Mach. Intel, Vol. PAMI-8, **6**, 679-698.

[119] Har-Peled, S., Roth, D., Zimak, D., 2003, "Constraint Classification for Multiclass Classification and Ranking." Becker, B., Thrun, S., Obermayer, K. (Eds) Advances in Neural Information Processing Systems 15: Proceedings of the 2002 Conference, MIT Press.

[120] Van der Walt, C.M., Barnard, E., 2007, "Data characteristics that determine classifier performance," SAIEE Africa Research Journal, **98** (3), 87-93.

[121] Yuan, Y., Shaw, M. J., 1995, "Induction of fuzzy decision trees," Fuzzy Sets and Systems, **69**, 125–139.

[122] Yang, T., 2006, "Computational Verb Decision Trees". International Journal of Computational Cognition, **4** (4): 34-46.